6-25-2015

C-MEMS Based Micro Enzymatic Biofuel Cells

Yin Song
Florida International University, ysong003@fiu.edu

FLORIDA INTERNATIONAL UNIVERSITY

Miami, Florida

C-MEMS BASED MICRO ENZYMATIC BIOFUEL CELLS

A dissertation submitted in partial fulfillment of the

requirements for the degree of

DOCTOR OF PHILOSOPHY

in

MATERIALS SCIENCE AND ENGINEERING

by

Yin Song

2015

To: Dean Amir Mirmiran
College of Engineering and Computing

This dissertation, written by Yin Song, and entitled C-MEMS Based Micro Enzymatic Biofuel Cells, having been approved in respect to style and intellectual content, is referred to you for judgment.

We have read this dissertation and recommend that it be approved.

_____
Jiuhua Chen

_____
Norman Munroe

_____
Chenzhong Li

_____
Xiangyang Zhou

_____
Chunlei Wang, Major Professor

Date of Defense: June 25, 2015

The Dissertation of Yin Song is approved.

_____
Dean Amir Mirmiran
College of Engineering and Computing

_____
Dean Lakshmi N. Reddi
University Graduate School

Florida International University, 2015

DEDICATION

I dedicate this dissertation to my loving parents, Xichang Song and Peiyu Tan for their unconditional support and love. This dissertation is also dedicated to my husband, Anthony Hiller.

ACKNOWLEDGMENTS

The completion of my dissertation and subsequent Ph.D has been a long journey. I am deeply grateful to my advisor, Dr. Chunlei Wang for her guidance, vision and support throughout the course of my PhD research. I express my special thanks to her for supervising and reviewing my research works and providing constructive comments to improve the quality of my research. I also appreciate her delicated attitude and high standard in supervising, which will be benifical for my whole life.

My gratitude is also extended to my dissertation committee members, Dr. Jiuhua Chen, Dr. Norman Munroe, Dr. Chenzhong Li and Dr. Xiangyang Zhou for their academic advice and continous support. I owe many thanks for their valuable suggestions and research discussions and support whenever I needed. I would like to thank Dr. Cesar Levy, who has provided tremendous help to me, especially when I had family emergency. I wish to thank Dr. Giri Narasimhan for his dedication to quality of gradute education.

Over six years I spent in Dr. Wang's group, I had the opportunity to work with so many amazing individuals. Here I have a lot of colleagues and friends to thank. I wish to acknowledge all my past and present lab mates, Dr. Jung-hoon Yang, Dr. Wei Chen, Dr. Xifei Li, Taekwon Kim, Yamini Parikh, Gregg Burrow, Sheidyn Ng, Kevin Bechtold, Varun Penmatsa, Majid Beidaghi, Abirami Dhanabalan, Chunhui Chen, Richa Agarwal andYong Hao, for help in my research and personal life.

I would like to acknowledge the excellent facilities provided at AMERI and support from past director Dr. Kinzy Jones and current director Dr. Arvind Agarwal at FIU. I highly appreciate Mr. Neal Ricks's knowledge and patience when training me with different equipments.

I acknowledge the University Graduate School at FIU for supporting me through Dissertation Evidence Acquisition (DEA) and Dissertation Year Fellowship (DYF) awards and Tech Fee. I also would like to appreciate all the collaborators: Dr. Sylvia Daunert, Dr. Sapna Deo, Dr. Leonidas Bachas from University of Miami, Dr. Marc Madou from University of University of Califoria-Irvine, Dr. Hiroshi Kawarada from Weseda University, Japan. I also appreciate NSF (CMMI, IRES, NERC) fundings to support my phD program.

Last, to my mom and dad, uncles, aunts, cousins for always being there for me, I couldn't thank you all more. Finally, I would like to thank my dear hunsband, who always believes in me and reminds me how lucky I am to have all the opportunities and to appreciate whatever I have in life.

ABSTRACT OF THE DISSERTATION

C-MEMS BASED MICRO ENZYMATIC BIOFUEL CELLS

by

Yin Song

Florida International University, 2015

Miami, Florida

Professor Chunlei Wang, Major Professor

Miniaturized, self-sufficient bioelectronics powered by unconventional micropower may lead to a new generation of implantable, wireless, minimally invasive medical devices, such as pacemakers, defibrillators, drug-delivering pumps, sensor transmitters, and neurostimulators. Studies have shown that micro-enzymatic biofuel cells (EBFCs) are among the most intuitive candidates for in vivo micropower.

In the fisrt part of this thesis, the prototype design of an EBFC chip, having 3D intedigitated microelectrode arrays was proposed to obtain an optimum design of 3D microelectrode arrays for carbon microelectromechanical systems (C-MEMS) based EBFCs. A detailed modeling solving partial differential equations (PDEs) by finite element techniques has been developed on the effect of 1) dimensions of microelectrodes, 2) spatial arrangement of 3D microelectrode arrays, 3) geometry of microelectrode on the EBFC performance based on COMSOL Multiphysics.

In the second part of this thesis, in order to investigate the performance of an EBFC, behavior of an EBFC chip performance inside an artery has been studied. COMSOL Multiphysics software has also been applied to analyze mass transport for different

orientations of an EBFC chip inside a blood artery. Two orientations: horizontal position (HP) and vertical position (VP) have been analyzed.

The third part of this thesis has been focused on experimental work towards high performance EBFC. This work has integrated graphene/enzyme onto three-dimensional (3D) micropillar arrays in order to obtain efficient enzyme immobilization, enhanced enzyme loading and facilitate direct electron transfer. The developed 3D graphene/enzyme network based EBFC generated a maximum power density of 136.3 μWcm^{-2} at 0.59 V, which is almost 7 times of the maximum power density of the bare 3D carbon micropillar arrays based EBFC.

To further improve the EBFC performance, reduced graphene oxide (rGO)/carbon nanotubes (CNTs) has been integrated onto 3D mciropillar arrays to further increase EBFC performance in the fourth part of this thesisThe developed rGO/CNTs based EBFC generated twice the maximum power density of rGO based EBFC. Through a comparison of experimental and theoretical results, the cell performance efficiency is noted to be 67%.

TABLE OF CONTENTS

CHAPTER PAGE

LIST OF TABLES

TABLE PAGE

LIST OF FIGURES

FIGURE PAGE

Figure 6.4 FTIR spectra of (a) graphene encrusted 3D micropillar arrays, (b) graphene/laccase encrusted 3D micropillar arrays, (c) graphene/GOx encrusted 3D micropillar arrays 87

CHAPTER 1

INTRODUCTION

1.1 Overview

The concept of biofuel cells has been known for one century since the first half-cell using E.coli was demonstrated by Potter at University of Durham in 1910 [1]. Further development of half-cell by Cohen from University of Cambridge led to one of the major types of biofuel cells, i.e., microbial fuel cells in 1931 [2]. Since the first enzymatic biofuel cell (EBFC) was reported by Yahiro in 1964 [3], noticeable developments have been made in terms of the power density, cell lifetime, operational stability for biofuel cells [4-6]. More recently, implantable medical devices such as pacemaker, defibrillator, insulin pumps, sensor-transmitter systems for animals and plants, nano-robots for drug delivery and health monitoring systems gain increasing attention which led to an upsurge in research and development in EBFCs as one of the potential alternatives to replace current batteries in implantable medical devices. In principle, EBFCs using biocatalysts can derive energy from physiological ambient resources abundantly available inside the human body [7]. The advantages of EBFCs include their biocompatibility, simple operation at physiological conditions, higher selectivity for particular substrates, higher volumetric catalytic activity and less resistive losses [8]. Before EBFC become competitive in practical applications, two critical issues: short lifetime and poor power density, both of which are related to enzyme stability, electron transfer efficiency, enzyme loading, etc. have to be addressed. 3-D electrode structures with high effective surface area per footprint can significantly improve EBFC power density by increase the enzyme loading. Besides, surface functionalization would enhance the enzyme stability

by forming the stable covalent bonding. Moreover, integration of nanostructures into microelectrode arrays could significantly improve the C-MEMS based EBFCs.

1.2 Research objectives

The ultimate goal of this research is to develop on-chip enzymatic biofuel cells with 3-D microelectrodes, which have high power density and improved lifetime. To achieve this goal, simulation and experimental work have been both conducted. On the one hand, the simulation will be conducted to 1) optimize the cell performance by obtaining the design rule of the 3-D microelectrode arrays; 2) examine the EBFC performance in the blood artery. On the other hand, the main objectives of the experimental work are to 1) increase the effective electrode surface area; 2) functionalize the electrode surface for stable immobilization of enzyme; 3) improve the electron transfer efficiency between substrate and electrode surface; 4) eventually develop the high performance C-MEMS based EBFCs.

The research problem has three main aspects:

1. How to properly build a computational modeling for 3-D EBFCs and predicate the device performance?

First, the steady state condition to mimick 3-D EBFCs in the lab environment has been investigated. Mass transport, conductivity and reaction kinetics and output power have been considered for optimum 3-D microelectrode designs for the EBFCs. Next, the simulation was targeted towards EBFC chip with 3-D microelectrode arrays inside a blood artery based on transient state condition. The performance of an EBFC chip placing in different orientations in the blood flow and novel design has been also investigated.

2. How to increase the surface area of electrodes?

One of the major challenges in developing EBFCs is to increase the power density, which is usually measured by power generation per surface area of electrode. However, for an EBFC to successfully power an implantable medical device, significant reduction in size must be achieved while at the same time maintaining relatively high current and power density. Normally, reducing size of EBFCs directly results in smaller amount of active electrode materials, which may significantly diminish the total energy and power output. In this regard, in order to improve the power density of miniaturized EBFCs, micro/nano-electrode architectures, which offer increased surface area, superior physiochemical properties and enhanced electrode reactions, should be investigated. Here the C-MEMS fabraication has been applied to develop 3-D micropillar arrays as platform for EBFCs development.

3. How to effectively immobilize enzyme on the C-MEMS electrodes surface?

The critical issue is short lifetime before EBFCs can be used in practical application. Enzyme stability upon immobilization on the electrode surface mainly decides EBFC lifetime. In this research, appropriate chemical immobilization method with stable covalent bonding between enzyme and electrode surface has been investigated. Furthermore, nanomaterials have been also integrated to immobilize enzymes onto the 3-D micropillars.

1.3 Scope of the dissertation

The dissertation work has included four research topics to meet its goal by pursuing the above objectives (Fig 1.1):

1. Optimization of 3-D microelectrode arrays configuration in the steady state model.

In an attempt to optimize the design rule of 3-D microelectrode arrays configuration, simulation using COMSOL multiphysics is conducted on the effect of dimensions and

spatial arrangement of 3-D microelectrode arrays on the EBFC performance by incorporating the mass transport and enzymatic kinetics in steady state model. In addition, four different electrode geometries are simulated to evaluate the distribution of current density on the electrodes.

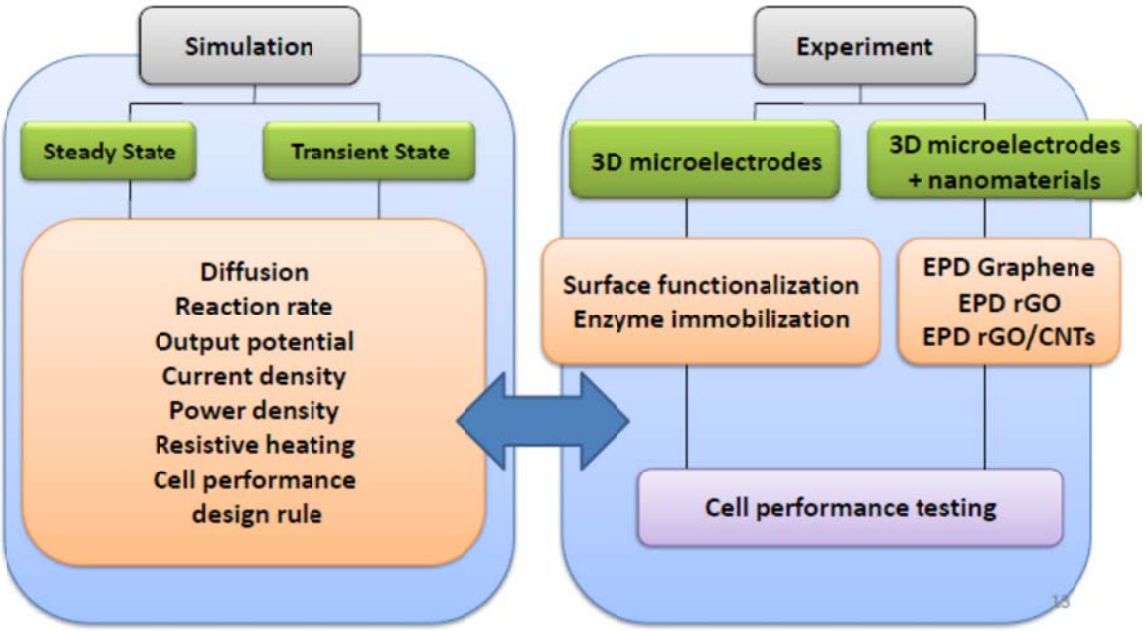

Figure 1.1. Organization of the dissertation.

2. Evaluation of EBFC with 3-D microelectrode arrays in blood artery in the transient state model.

Based on the result from optimized design rule of 3-D microelectrode arrays, performance of 3-D EBFC is simulated in the transient state mimicking in the blood artery, in terms of output potential and electric field of electrodes. Current and power density is also determined for 3-D EBFC in the blood artery in different chip orientations and designs.

3. C-MEMS based miniaturized EBFC with 3-D microelectrode arrays.

3-D microelectrode arrays will be fabricated by C-MEMS. Glucose oxidase and laccase will be immobilized on the anode and cathode, respectively. The immobilization method

is based on diazonium salts to form a covalent binding bwteen electrodes and enzymes. Performance of 3-D microelectrode arrays based EBFC is evaluated.

4. EBFC with 3-D graphene integrated microelectrode arrays.

In order to improve cell performance based on 3-D design, carbon nanomaterials such as graphene, rGO, CNTs are integrated in C-MEMS microelectrode arrays. Glucose oxidase and laccase will be immobilized on the anode and cathode, respectively. EBFC performance with different nanomaterials modified 3-D EBFCs are evaluated and the results are to be compared with 3-D design without nanomaterials.

1.4 References

1. M.C. Potter, Proceedings of the Royal Society B, 84 (1910), pp. 260.

2. B. J. Cohen, Bacteriol. 21 (1931), pp. 18.

3. A.T. Yahiro, S.M. Lee, D.O. Kimble, Biochim. Biophys. Acta. 88 (1964), pp. 375-383.

4. J. Bockris, S. Srinivasan, Fuel cells: their electrochemistry. NewYork. McGraw-Hill. (1969).

5. G. Govil, A. Saran, Biochemical fuel cells. J Indian Chem. Soc. 59 (1982), pp. 1226-1228.

6. G. Palmore, G.M. Whitesides, American Chemical Society. 566 (1994), pp. 271-290.

7. L. Halamkova, J. Halamek, V. Bocharova, A. Szczupak, L. Alfonta, E. Katz, J. Am. Chem. Soc. 134 (2012), pp. 5040-5043.

8. E. Katz, A.N. Shipway, I. Willner, Biochemical fuel cells. In: Handbook of Fuel Cells—Fundamentals, Technology and Applications, W. Vielstich, H.A. Gasteiger and A. Lamm, Fundamentals and Survey of Systems vol. 1, John Wiley & Sons, Ltd., Hoboken, NJ, (2003), pp. 355-381.

CHAPTER 2

BACKGROUND AND LITERATURE REVIEW

2.1. Introduction

The global energy demands increases significantly every year and current reliance on fossil fuels is unsustainable due to finite supplies from environment. In addition, the products from using fossil fuels cause critical pollution, which forms global warming. Fuel cells offer an alternative solution to this issue. A fuel cell is an electrochemical cell that converts chemical energy from a fuel to electrical energy. In a fuel cell, an oxidation reaction occurs at the anode and a reduction reaction occurs at the cathode. The oxidation from anode generates electrons, which transfer to the cathode through the external circuit. Conventional fuel cells, for example, can be operated by using hydrogen or methanol (MeOH) as fuels, to produce energy, along with water and carbon dioxide as by-products. However, hydrogen is gaseous which gives rise to storage and transport issues. In addition, many of the alternative fuels that can be used for fuel cells still rely on petroleum products. Therefore, it is well recognized that alternative sources of renewable energy are urgently required. Numerous efforts have been made to develop these power sources alternatives that are capable of performing in physiological conditions for prolonged lifetime without recharging. More recently, the US implantable medical devices market increases at an average rate of 8% every year and is expected to reach $73.9 billion by 2017 (Fig. 2.1). The development of miniaturized medical implants such as pacemaker, defibrillator, insulin pumps, sensor-transmitter systems for animals and plants, nano-robots for drug delivery and health monitoring systems gain increasing attention which led to an upsurge in research and development in micropower source, especially, biofuel cells (Fig. 2.2) [1-10]. Biofuel cell is a particular kind of fuel cell, which converts biochemical energy to electrical energy by using biocatalysts [12-14]. In the

following section, brief review on recent progress in biofuel cells, which offer possibilities for implantable devices within the human body, is presented.

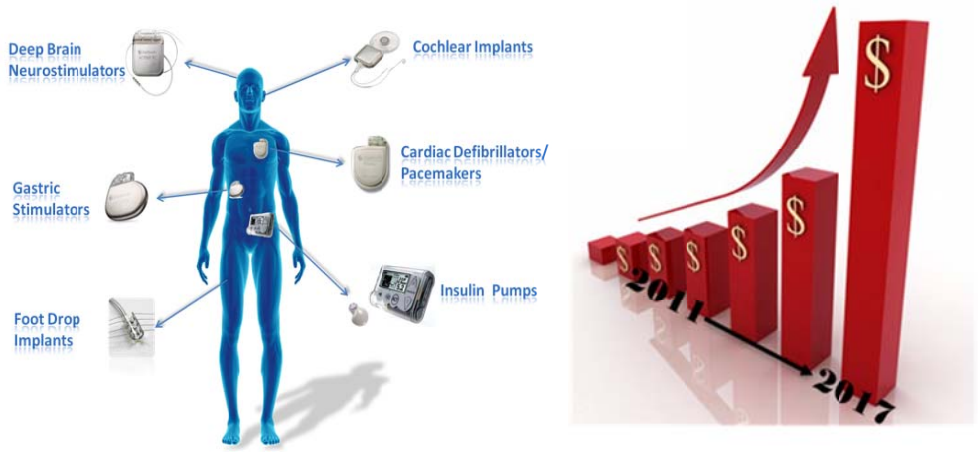

Figure 2.1. Various types of implantable medical device [14].

2.2 Background

Fig. 2.2 illustrates the evolution of biological energy. The earliest discovery between biology and electrical energy was demonstrated by Galvani in 1791 showing the frog leg twitching from an electric current. The first fuel cell, which involved electrolysis of water, was discovered by Grove in 1839. Since an electrical action can induce a biological reaction, the converse that biological processes can generate electricity can also be true. This led the first half-cell using microorganism (E.coli) demonstrated by Potter at University of Durham. Further development of half-cell by Cohen from University of Cambridge led to one of the major types of biofuel cells, i.e., microbial fuel cells. Cohen applied a number of microbial half-cells connected in series, which generated over 35 volts [15]. The interest in development of biofuel cells expanded by the USA space program, in the late 1950s and early 1960s, which led to the possibility of microbial fuel cells as an advanced technology for waste disposal treatment in space flights. Also, in the late 1960s, the first enzymatic biofuel cell using cell-free enzyme systems was discovered aiming to permanently power medical implants by utilizing specific body fluids as fuel [16]. However, the output potential

generated from enzymatic biofuel cells was far beyond the demand of commercialized application and the research reached the bottleneck ever since. Until early 2000s, it was found out that power output could be greatly improved by using electron mediators, which acted as electron shuttle between electrode and enzyme [17]. Shewanella putrefaciens, Geobacteraceae sulferreducens, Geobacter metallireducens and Rhodoferax ferrireducens are all bioelectrochemically active and can transfer electrons directly through the membrane [18]. A breakthrough was also made when chemical covalent binding based enzyme immobilization has been proved to increase the cell performance, in the terms of the power density, cell lifetime, and operational stability [19]. In the past ten years, cell performances on EBFCs have been improved significantly and the detailed development in will be discussed the following sessions.

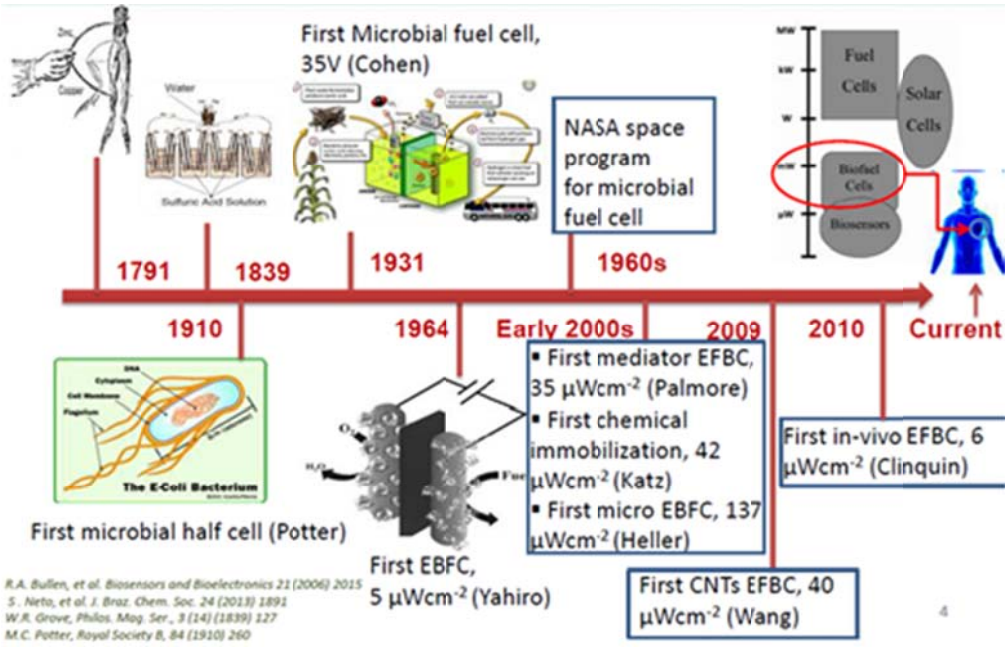

Figure 2.2. Evolution of biological energy.

2.3 Enzymatic biofuel cells

Enzymatic biofuel cells (EBFCs) utilize redox enzymes such as glucose oxidase (GOx), laccase as the catalysts that can facilitate the electron generation between substrates and

electrode surface, hence generating the output potential. There are two types of electron transfer mechanisms, which are direct electron transfer (DET) and mediator electron transfer (MET). In DET based EBFCs, the substrate is enzymatically oxidized at the anode, producing protons and electrons, which directly transfer from enzyme moleculars to anode surface. At the cathode, the oxygen reacts with electrons and protons, generating water. However, DET between an enzyme and electrode has only been reported with several enzymes such as cytochrome c, laccase, hydrogenase, and several peroxidases [20-25]. Some enzymes have nonconductive protein shell in which holds active site of enzyme so that the electron transfer is inefficient as well as output potential. To overcome this barrier, MET was used to enhance the transportation of electrons. The selection and mechanism of MET in EBFCs are quite similar to those of MFCs that discussed before. Similarly, there are still some challenges in using MET in EBFCs, which are poor diffusion of mediators and non-continuous supply. Therefore, modification of bioelectrodes to realize DET based EBFCs attracted most attention in current researches. In EBFCs system, power density and lifetime are two most important factors, which determine the cell performance in the application of EBFCs. Significant improvements have been made during the last decade to overcome those problems [26-29]. Noticeably, these advancements have been mostly achieved by modification of electrode with better performance, improving enzyme immobilization methods as well as optimizing the cell configuration.

The performance of electrodes for EBFCs depends on these factors: electron transfer kinetics, mass transport, stability, and reproducibility. Therefore, the electrode is mostly made of gold foil and rod, platinum foil and rod, or carbon paper, rod, paste, metalized carbon, glassy carbon and carbon fiber [30-34]. Instead of those conventional materials, biocompatible conducting polymers are widely used because they can facilitate electron transfer and immobilize the enzymes at the same time which is widely applied in enzyme

immobilization method [35-38]. In order to maximize the cell performance, mesoporous materials have been applied in many studies because of their high surface areas thus high power density could be achieved [39-42]. Moreover, many attempts using nanostructures such as nanoparticles, nanofibers, and nanocomposites as electrodes materials have also been made to fabricate electrodes for EBFCs. The large surface area by using these nanostructures leads to high enzyme loading beyond immobilization, hence improving the power density of enzymatic biofuel cells.

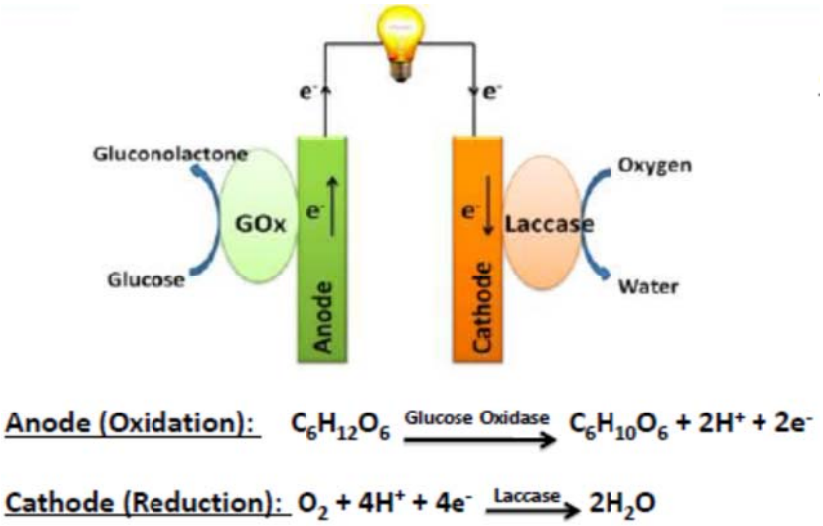

Figure 2.3 Mechanism of EBFCs.

Recently, one of the most significant advances in EBFCs those electrodes modification by employing nanomaterials [43-45]. Several research activities have addressed the generation of application of single wall carbon nanotube hybrid system [43-45]. The oriented assembly of short single wall carbon nanotubes (SWNT) normal to electrode surfaces was accomplished by the covalent attachment of the CNT to the electrode surface. It was reported that surface assembled GOx is in good electric contact with electrode due to the application of SWNT, which acted as conductive nanoneedles that electrically wire the enzyme active site to the transducer surface. Other studies have been reported to improve electrochemical and electrocatalytic behavior of SWNT, as well as fast electron transfer kinetics on SWNT

and MWNT. Improved enzyme activity was observed in comparison to similar enzyme-containing composites without using SWNTs. It was discussed that the application of SWNTs, which possesses a high specific surface area, may effectively adsorb enzyme molecules and retains the enzyme within the polymer matrix, whereas other forms of enzyme-composites may suffer from enzyme loss when they were placed in contact with aqueous solutions. The stable and active enzyme system on conductive CNTs will make a great impact in the field of biofuel cells. Furthermore, graphene and its derivtives also have potential in developing high performance EBFCs. Therefore it is necessary to further study this area in order to realize high performance EBFCs in the dynamic energy market.

In addition, the immobilization of the enzymes on the electrode surface is considered as another one of the critical factors that affect cell performance. The immobilization of enzyme can be achieved physically or chemically. There are two major types of physical methods. The first one is to absorb the enzymes onto conductive particles such as carbon black or graphite powder. Hydrogenase and laccase have been immobilized by using this method on carbon black particles to construct composite electrodes and EBFCs had been continuously worked for 30 days. Another physical immobilization method is polymeric matrices entrappment, which usually stabilize the enzymes better than surface adsorption [46-48]. Soukharev utilized redox polymers to fabricate enzymatic biofuel cells system. The electrodes were built by casting the enzyme-polymer mixed solution onto 7-μm diameter, 2 cm length carbon fibers. It showed that the glucose–oxygen biofuel cell was capable of generating a power density up to 0.35 mW/cm^2 at 0.88 V. Compared with the physical immobilizaition, which is unstable during the operation, the chemical immobilization methods with the efficient covalent bonding of enzymes and mediators are more reliable. Katz et al. reported a biofuel cells using co-immobilized enzyme-cofactor-mediator composites on metal electrodes to functionalize the electrode surface with a monolayer then

integrate with enzymes via bioaffinity. Another example is that a redox monolayer was covalently grafted with pyrroloquinoline quinone (PQQ) to Au-electrode. Then GOx-FAD electrode was assembled with PQQ as mediators. Other widely materials used to functionalize electrode surface have also been reported, such as nitrospiropyran, rotaxane, C-60, and Au nanoparticles.

Fuel	Enzyme	Electrode	Electron transfer	Power density ($\mu W\ cm^{-2}$)	Ref.
Glucose/ O_2	GOx/laccase	Carbon fiber electrodes	MET	64	Chen et al. (2001)
Glucose/ O_2	GOx/BOx	Carbon fiber electrodes	MET	432	Mano et al. (2002)
Glucose/ O_2	GDH/BOx	Glassy carbon disc electrodes	MET	58	Tsujimura et al. (2002)
Glucose/ O_2	GOx/COx	Gold electrodes coated with Cu	MET	4.3	Katz & Willner (2003)
Glucose/ O_2	GOx/BOx	Carbon fiber electrodes	MET	50	Kim et al. (2003)
Glucose/ O_2	GOx/BOx	Carbon fiber electrodes	MET	440	Mano et al. (2003)
Glucose/ O_2	GOx/BOx	Carbon fiber electrodes	MET	244	Mano & Heller (2003)
Glucose/ O_2	GOx/laccase	Carbon fiber electrodes	MET	350	Heller (2004)
EtOH to CH_3CHO to CH_3COOH	ADH, ADH +AldDH, dehydrognase + FDH	Carbon coated with poly(methylene)	MET	1160	Akers et al. (2005)

Glucose/ O_2	PLL-VK_3 / PDMS	Pt	MET	130	Togo et al. (2007)
Ethanol/H_2O_2	QH-ADH/AOx	Pt	DET	30	Ramanavicius et al. (2008)
Glucose/ O_2	GDH/PDMS	Pt	DET	11000	Sakai et al. (2009)
Glucose/ O_2	GOx/laccase	Silicon/ SWNTs	DET	30	Wang et al. (2009)
Glucose/ O_2	GOx/laccase	Au/SWNTs	DET	960	Lee et al. (2010)
Glucose/ O_2	GDH/BOD	Au/MWNTs	DET	200	Tanne et al. (2010)
Glucose/O_2	GDH/NB	Glass carbon/ SWNTs	DET	100	Saleh et al. (2011)
Glucose/O_2	GOx/BOD	CRGO/Au	MET	24.3	Liu et al. (2010)
Glucose/O_2	GOx/laccase	GCE/graphene	DET	58	Zhang et al. (2010)
Glucose/O_2	GOx/laccase	CRGO/Au	MET	78.3	Liu et al. (2011)
Glucose/O_2	GOx/laccase	GCE/ERGO-MWCNTs	MET	46	Devadas et al. (2012)

Table 2.1 The performance of EBFCs

Rapid development on EBFCs has been achieved in the past decade with the arised demands for reliable power supplies for implantable medical device. The table 1 has shown the performance of the EBFCs. However, there are still challenges for further development of long term stability of the enzymatic bioelectrodes and efficient electron transfer between

enzymes and electrode surfaces. Recent efforts have been given to protein engineering, reliable immobilization method and novel cell configuration.

2.4 Miniature biofuel cells

Miniature power systems are widely applied in devices that require miniature electrical power sources especially in implantable medical device. The prospects of medical implants can be realized only if the implantable device could be extremely small. This can be achieved by miniaturization of different functional components such as electrodes, power supply, and signal processing units. Efforts have been made in miniature biofuel cells in the past ten years. Development of miniature biofuel cells offers great opportunities for long-term power sources of implantable device where frequent switching of battery is not practical. The ability of biocatalyst in converting indigenous fuels into electrical energy makes miniature biofuel cells applicable because biocatalysts can replenish to enable long-term and self-sustained power system as long as there is enough supply of fuels. Common procedures for fabricating microfluidic systems are photolithography, etching, polymer molding, and metal deposition and these have been widely applied in fabricating miniature biofuel cells. For example, Siu and Chiao applied photolithography and polymer molding to fabricate polydimethylsiloxane (PDMS) electrodes. It was also used by Hou et al. to fabricate gold electrode arrays for the microbe screening. Besides polymer molding, etching can also be used to transfer micro-patterns onto device-building substrate. Chiao applied wet etching to construct silicon-based chambers containing serpentine channels. Additionally, C-MEMS microfabrication technique for 3D microstrustures, involving the pyrolysis of patterned photoresist has been developed which can be used as microelectrodes for miniature biofuel cells [49-50]. Besides, photoresist with micro-pattern was used to define the chambers as well. With current microfabrication processes, the miniature biofuel cells offer unique advantages such as large surface area-to-volume ratio, short electrode distance, fast response time and low Reynolds number. Here we

will introduce principles, design strategies and experimental demonstrations of representative miniature biofuel cells, along with the discussion of the key challenges and opportunities for realizing the practical potential of miniaturized biofuel cells for medical implants.

The first micro-size enzymatic biofuel cells reported in 2001. A glucose/oxygen biofuel cell, consisting of two 7-μm diameter, 2-cm long, 0.44 mm^2, electrocatalyst-coated carbon fibers and operating at ambient temperature in a pH 5 aqueous solution was described. The areas of the anode and the cathode of the cell were about 60 times smaller than those of the smallest reported fuel cell and 180 times smaller than those of the smallest area biofuel cell. The power density of the cell is 64 $\mu W/cm^2$ at 23 °C and 137 $\mu W/cm^2$ at 37 °C, and its power output is 280 nW at 23 °C and 600 nW at 37 °C. The results revealed that the miniature enzymatic biofuel cells could generate sufficient power for slower and least power-consuming CMOS circuit. Later, a miniature enzymatic biofuel cell with the same micro size carbon fiber operating in a physiological buffer was reported. In a week operation the cell generates 0.9 J of electrical energy while passing 1.7 C charge. Based on this result, Mano developed a miniature compartment-less glucose-O_2 biofuel cell operating in a living plant. Implantation of the fibers in the grape leads to an operating biofuel cell producing 2.4 μW at 0.52 V, which is adequate for operation of low-voltage CMOS/SIMOX integrated circuits. The performance of the miniature enzymatic biofuel cell was upgraded to 0.78V operating at 37C in ph 5 buffer later on. In 2004, a miniature single-compartment glucose−O_2 biofuel cell made with the novel cathode operated optimally at 0.88 V, the highest operating voltage for a compartmentless miniature fuel cell. The enzyme was formed by "wiring" laccase to carbon through an electron conducting redox hydrogel, its redox functions tethered through long and flexible spacers to its cross-linked and hydrated polymer, which led to the apparently increased electron diffusion coefficient. The latest report on miniature glucose/O_2 biofuel cells demonstrated a new kind of carbon fiber microelectrodes modified with single-wall

carbon nanotubes (CNTs). The power density of this assembled miniature compartment-less glucose/O_2 BFC reaches 58l Wcm^{-2} at 0.40 V. When the cell operated continuously with an external loading of 1 M resistance, it lost 25% of its initial power in the first 24 h and the power output dropped by 50% after a 48 h continuous work. Although from the practical application point of view, the performance and the stability of the current emzymatic biofuel cells remain to be improved, the miniature feature and the compartment-less property as well as the tissue-implantable biocapability of enzymatic biofuel cell essentially enable the future studies on in vivo evaluation of the cell performance and stability in real implantable systems.

Additionally, based on C-MEMS fabrication technologies, our research focuses on the 3D microelectrodes for miniature enzymatic biofuel cells. First, we apply finite element approach to simulate this miniature EBFCs to attain the design rule such as electrode aspect ratio, configuration as well as orientation of the chip. According to the simulation, a prototype EBFC consisting of glucose oxidase immobilized anode and a laccase immobilized cathode using C-MEMS based interdigited electrode arrays was built.

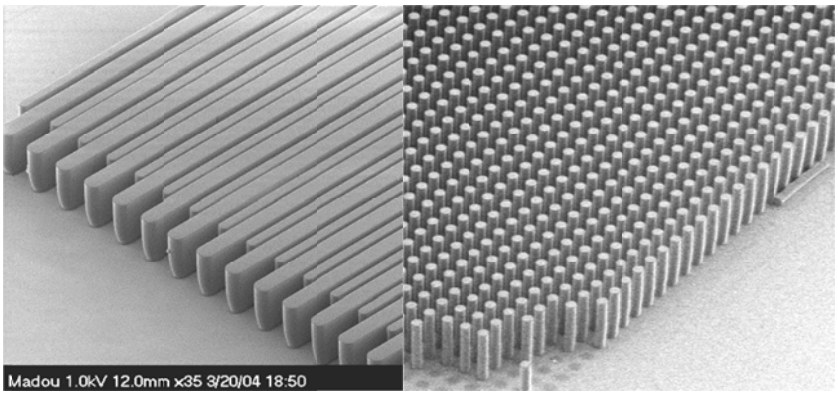

Figure 2.4 C-MEMS microstructure [50-52].

2.5 C-MEMS 3-D architecture electrodes

The surface area of biofuel cells determines its amperage, meaning that cell power is directly proportional to the electrode surface area. A conventional 2D power system is

typically a parallel arrangement of a planar cathode and an anode separated by a solid or liquid electroyte. In order to maximize power density, three-dimensional bioelectrocatalytic electrodes should include multidimensional and multidirectional pore structures. Multidimensionality provides small pores to support enzyme stabilization and high loading densities. More recently, The revolutionary carbon-microelectromechanical (C-MEMS) fabrication technologies have offered a wide range of opportunities to engineers and researchers to reproducibly fabricate complex carbon-based EBFCs, having 3D highly dense micro-scaled electrodes arrays with low cost and on chip switchable designs. Electrodes based on 3D microstructures offer higher surface area and significant advantages in comparison to thin-film devices for powering MEMS and miniaturized electronic devices. C-MEMS, describes a manufacturing technique in which carbon microstructures are fabricated by baking UV sensitive polymers at high temperatures in an inert environment. It has been demonstrated that 3D high-aspect-ratio carbon structures can be made from carbonizing (pyrolysis) patterned NANOTM SU-8 negative photoresist layers. Both positive photoresists (AZ4620, AZ1518) and negative photoresist (SU-8) can be converted by carbon by pyrolysis depending on the application.

Although the 3D structures have significant advantages, such as an increase in the surface area and power density for same foot print area, compared to 2D planar electrodes or thin films, there are yet certain important issues, which need to be solved in order to use these structures effectively. Anandan and Godino have studied the mass transport phenomenon in micro and nano-electrodes by finite element analysis approach. They suggest that in order to accommodate the specific analyte species in terms of reaction kinetics and mass transport, it is necessary to optimize the geometry of nanopillars (their diameter, spacing and height), to reap the true benefit of using micro-nanostructured electrodes for enhancing the performance of biosensors. They reveal that the glucose immediately react with the top portions of the

nanopillars due to higher reaction rate of enzymes and hence the bottom portion of the pillars lack the glucose, which may not be favorable to improve the performance of EBFC. Jeffrey suggests that in contrast to the 2-D electrodes, in which uniform current density is naturally obtained over the surface of the cathodes and anodes, the current density in the 3-D microelectrode array suffer from a non-uniform primary current distribution. These non-uniform currents result in utilization of the electrode materials, and are thus associated with lower cell efficiencies, reduced electrodes stability due to non-uniform stresses, and non-uniform heat dissipation. Therefore, it is essential to select the geometries of electrodes, which homogenize the current density distribution around microelectrodes surfaces.

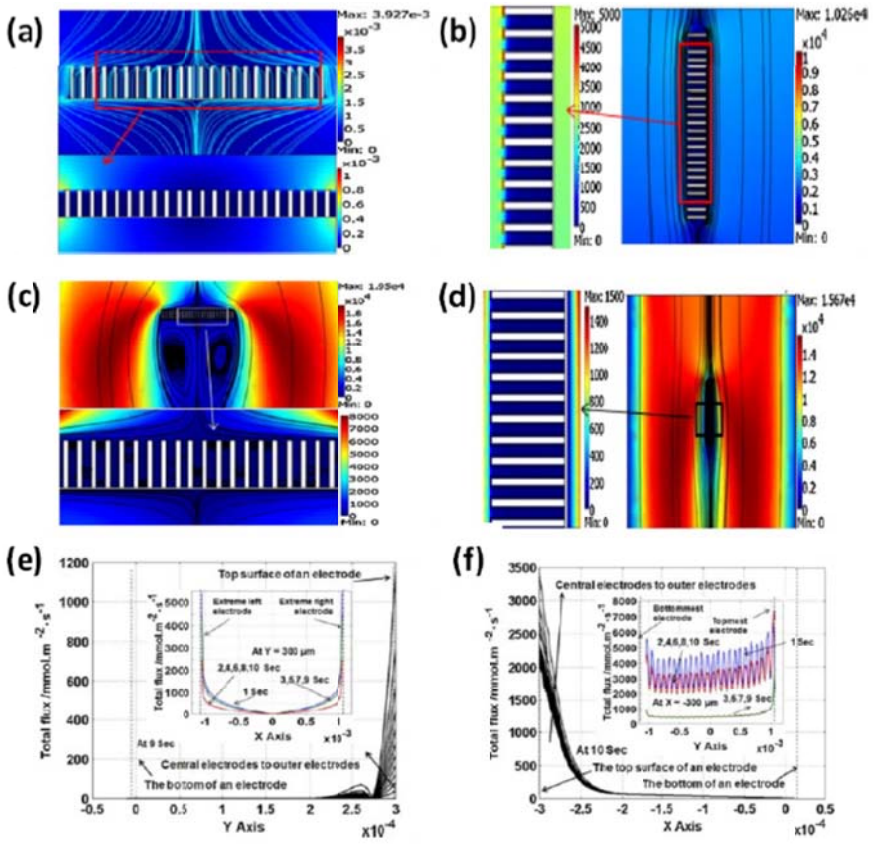

Figure 2.5 Surface plot with streamlines for diffusive flux of glucose around microelectrodes for (a) HP and (b) VP. Surface plot withstreamlines for convective flux of glucose around microelectrodes for (a) HP and (b) VP. Total fluxes in between micro-electrodes for (a) HP and (b) VP. Insets provide the total flux on top of all electrodes [26].

2.6 Finite element analysis simulation

Modeling could play a vital role in optimizing the design of increasingly sophisticated devices, taking into account various factors regarding mass transport, electron transfer, and reaction kinetics. Until now, majority of the EBFCs research have been focused on in vitro experiments by mimicking physiological conditions. However, additional complications may arise when an EBFC chip is placed inside a blood artery, such as implantation process, the stability of chip inside an artery and the clotting of the blood, etc. Ideally, the EBFC chip should be placed in a manner that it would not obstruct the blood flow and it should not result in substantial pressure drop inside an artery. In order to investigate the stability of an EBFC, we have mimicked the behavior of an EBFC chip performance inside an artery [26]. We applied COMSOL 3.5 Multiphysics software to analyze mass transport for different orientations of an EBFC chip inside a blood artery. During the initial stage, we have analyzed two orientations: horizontal position (HP) and vertical position (VP). The stability of the chip in these positions, diffusion and convectional fluxes around microelectrodes has been finely investigated in Fig 2.5. From the comparison between HP and VP in the blood artery, we can conclude that the chip can be more stable in the VP as there is no external drag force due to turbulences surrounded the chip. The diffusion in between microelectrodes is negligible in HP and it is better in VP of a chip. In HP, the flux distribution is very different for each electrode from center to edge. The diffusive flux and convective flux are higher for microelectrodes located on the circumference of the horizontally positioned chip. At the central electrodes, these fluxes are negligible. In VP, these fluxes are uniform for all electrodes although negligible in between electrodes. In VP, there will not be limitation of increasing the foot print area. In HP, an increase in foot print area will allow thicker boundary layers to be formed, which can obstruct the blood flow. Based on the results, we have proposed a novel chip design with holes in between all electrodes on the substrate, which can

drastically improve the diffusion in between microelectrodes. From the comparison between a prototype design without holes and a proposed design with holes, it is concluded that the diffusive flux and convective flux have been significantly improved in a chip with holes. The uniformity of these fluxes has also been improved with all microelectrodes receiving similar diffusive and convective flux. The overall flux has been drastically improved in the HP with holes compared to a chip without holes in both horizontal and vertical position.

In this thesis, establishing rigorously validated models in conjunction with experimental studies to develop advanced microbiofuel cells with optimized 3D C-MEMS-based EBFCs has been targeted. A modeling study based on coupling mass transport, enzyme kinetics, and electron transfer with a COMSOL multiphysics module, has been investigated.

2.7 References

1. F. D. Réaumur, L'art de convertir le fer forgé en acier, et l'art d'adoucir le fer fondu, ou de faire des ouvrages de fer fondu aussi finis que le fer forge, 1722(English translation from 1956), Paris, Chicago.

2. G. Federico, The cementation of Iron and Steel, 1914, McGraw-Hill Book Company, ISBN: 9781149305690.

3. A. Lavoisier, Traite elementaire de chimie.,1789 (English translation in 1790).

4. P. Shevlin. Formation of atomic carbon in the decomposition of 5-tetrazolyldiazonium chloride. 1972, Journal of the American Chemical Society, 94, 1379–1380.

5. M. J. S. Dewar, D. J. Nelson, P. B. Shevlin, and K. A. Biesiada. Experimental and theoretical investigation of the mechanism of deoxygenation of carbonyl compounds by atomic carbon. 1981, Journal of the American Chemical Society, 103,2802–2807.

6. T.W. Ebbesen, ed. Carbon nanotubes—preparation and properties. 1997, Boca Raton, Florida: CRC Press. ISBN: 0849396026.

7. H. W. Kroto, J. R. Heath, S. C. O'Brien, R. F. Curl, and R. E. Smalley. C60: Buckminsterfullerene. 1985, Nature, 162–163.

8. C. Frondel, U. B. Martin. Lonsdaleite, a hexagonal polymorph of diamond. 1967, Nature, 587–589.

9. R. J. Lagow, J. J. Kampa, H-C Wei, S. L. Battle, J. W. Genge, D. A. Laude, C. J. Harper, R. Bau, R. C. Stevens, J. F. Haw, and E. Munson. Synthesis of linear acetylenic carbon: The sp carbon allotrope. 1995, Science, 362–367.

10. A. V. Rode, E. Gamalay, A. G. Christy, J. Fitz Gerald, S. T. Hyde, R. G. Elliman, B. Luther-Davies, A. I. Veinger, J. Androulakis, and J. Giapintzakis. Unconventional magnetism in all-carbon nanofoam.2004, Physical Review B, 70(5):0544071–0544079.

11. J. Robertson. Hard amorphous (diamond-like) carbons. 1991, Progress in Solid State Chemistry, 21,199–333.

12. D. B. Ratner, Pyrolytic carbon. 2004, In Biomaterials science: an introduction to materials in medicine. Academic Press., ISBN:0125824637.

13. A. K. Geim, K. S. Novoselov, The rise of graphene, 2007, Nature Materials, 6, 183–191.

14. http://en.wikipedia.org/wiki/File:Eight_Allotropes_of_Carbon.png.

15. N. L. Pocard, D. C. Alsmeyer, R. L. McCreery, T. X. Neenan, M. R. Callstrom. Doped glassy carbon: A new material for electrocatalysis. 1992, Journal of Materials Chemistry, 2, 771–784.

16. M. J. Madou, Fundamentals of microfabrication: The science of miniaturization. 1998, CRC-Press, ISBN: 0849394511.

17. G.E. Hak, The MEMS handbook. 2001, Boca Raton: CRC press, ISBN: 0849321069

18. R. P. Ribas, J. L. Leclercq, J. M. Karam, B. Courtois, P. Viktorovitch, Bulk micromachining characterization of 0.2 μm HEMT MMIC technology for GaAs MEMS design, 1998, Materials Science and Engineering, B: Solid-State Materials for Advanced Technology, 51, 267–273.

19. M. Datta, M. W. Pruessner, D. P. Kelly, R. Ghodssi, Design of MEMS-tunable novel monolithic optical filters in InP with horizontal bragg mirrors. 2004, SolidState Electronics, 48, 1959–1963.

20. M. Gromova, K. Baert, C.Van Hoof, A. Mehta, A. Witvrouw, The novel use of low temperature hydrogenated microcrystalline silicon germanium (SiGe:H) for MEMS applications. 2004, Microelectronic Engineering, 76, 266–271.

21. S. Guan, R. B. Nielsen, Rapid scan Fourier transform detection of a frequency encoded quartz crystal microbalance array. 2003, Review of Scientific Instruments, 74, 5241–5248.

22. M. Evans, C. Sewter, E. Hill, An encoded particle array tool for multiplex bioassays. 2003, Assay and Drug Development Technologies, 1, 199–207.

23. C. Wang, M. Madou, From MEMS to NEMS with carbon. 2005, Biosensors and Bioelectronics, 20, 2181–2187.

24. A. M. Lyons, Photodefinable carbon films: electrical properties. 1985, Journal of Non-Crystalline Solids, 70, 99–109.

25. S. Ranganathan, R. McCreery, S. Majji, M. Madou, Photoresist-Derived Carbon for Microelectromechanical Systems and Electrochemical Applications. 2000, J. Electrochem. Soc., 147, 277-282.

26. K. S. Ma, G. Jia, C. Wang, M. Madou, Fabrication of nanoscale carbon structures by C-NEMS technology. 2005, Proceedings of NSTI-Nanotech, 2, 151–154,

27. O. J. A. Schueller, S. T. Brittain, C. Marzolin, G. M. Whitesides, Fabrication and characterization of glassy carbon MEMS. 1997, Chemistry of Materials, 9, 1399– 1406

28. K. Malladi, C. Wang, M. Madou, Microfabrication of suspended C-MEMS structures by EB writer and pyrolysis method. 2006, Carbon, 44, 2602–2607

29. S. Konishi, M. Liger, T. A. Harder, Y. C. Tai, Parylene-Pyrolyzed carbon for MEMS application. 2004, Proceedings of IEEE MEMS, 161–164

30. C. Wang, R.Zaouk, M. Madou, Local CVD of carbon nanofibers from photoresist. 2006, Carbon, 44, 3073–3077.

31. O. J. A Schueller, S. T. Brittain, G. M. Whitesides, Fabrication of glassy carbon microstructures by soft lithography. 1999, Sensors and Actuators A, 72, 125–139

32. O. J. A. Schueller, S. T. Brittain, G. M. Whitesides. Fabrication of glassy carbon microstructures by pyrolysis of microfabricated polymeric precursors. 1997, Advanced Materials, 9, 477–480, 1997

33. X.-M. Zhao, Y. Xia, O. J. A. Schueller, D. Qin, G. M. Whitesides. Fabrication of microstructures using shrinkable polystyrene films..1998, Sensors and Actuators A: Physical, 65, 209–217.

34. J. Kim, X. Song, K. Kinoshita, M. Madou, R. White. Electrochemical studies of carbon films from pyrolyzed photoresist.1998, Journal of the Electrochemical Society, 45, 2314–2319.

35. R. Kostecki, X. Song, K. Kinoshita. Influence of geometry on the electrochemical response of carbon interdigitated microelectrodes.2000, Journal of the Electrochemical Society, 147,1878–1881.

36. S. Ranganathan, L. McCreery. Electroanalytical performance of carbon films with near-atomic flatness.2001, Analytical Chemistry, 73, 893–900.

37. A. Singh, J. Jayaram, M. Madou, S. Akbara. Pyrolysis of negative photoresists to fabricate carbon structures for microelectromechanical systems and electrochemical applications. 2002, Journal of the Electrochemical Society, 149, E78– E83.

38. C. Wang, G. Jia, L. H. Taherabadi, M. J. Madou. A novel method for the fabrication of high-aspect ratio C-MEMS structures.2005, Journal of Microelectromechanical Systems, 14,348–358.

39. B. Park, L. Taherabadi, Ch. Wang, J. Zoval, and M. Madou. Electrical properties and shrinkage of carbonized photoresist films and the implications for carbon microelectromechanical systems devices in conductive media. 2005, Journal of the Electrochemical Society, 152, J136–J143.

40. W. Chen, M. Beidaghi, V. Penmatsa, K. Bechtold, L. Kumari, W.Z. Li, C. Wang, Integration of Carbon Nanotubes to C-MEMS for On-chip Supercapacitors. 2010, Nanotechnology, IEEE Transactions on, 9, 734-739.

41. V. Penmatsa, T. Kim, M. Beidaghi, H. Kawarada, Z. Wang, L. Gu, C. Wang, Three-dimensional graphene nanosheets encrusted carbon micropillar arrays for electrochemical sensing. 2012, Nanoscale, DOI:10.1039/C2NR30161J.

42. W. Chen, M. Beidaghi, V. Penmatsa, K. Bechtold, L. Kumari, W.Z. Li, C. Wang, Integration of Carbon Nanotubes to C-MEMS for On-chip Supercapacitors. 2010, Nanotechnology, IEEE Transactions on, 9, 734-739.

43. M. Beidaghi, C. Wang, Micro-supercapacitors based on Three Dimensional Interdigital Polypyrolle/C-MEMS Electrodes.2011, Electrochimica Acta, 95089514.

44. M. Colburn, S. Johnson, M. Stewart, S. Damle, T. Bailey, B. Choi, M. Wedlake, T. Michaelson, S.V. Sreenivasan, J.G. Ekerdt, C.G. Willson. Step and flash Imprint lithography: A new approach to high resolution patterning. 1999, Proc. SPIE, 3676(I), 379-390

45. S. Sotiropoulou, V. Gavalas, V. Vamvakaki, N.A Chaniotakis, Novel carbon materials in biosensor systems. 2002, 18, 211-215.

46. J. A. Lee, S. Hwang, J. Kwak, S. I. Park, S. S. Lee, K-C Lee, An electrochemical impedance biosensor with aptamer-modified pyrolyzed carbon electrode for labelfree protein detection. 2008, Sensors and Actuators B, 129, 372-379.

47. J. A. Lee, K-C. Lee, S. I. Park, S. S. Lee, The fabrication of carbon nanostructures using electron beam resist pyrolysis and nanomachining processes for biosensing applications. 2008, 19, 215302 (pp7).

48. H. Xu, K. Malladi, C. Wang, L. Kulinsky, M. Song, M. Madou, Carbon postmicroarrays for glucose sensors. 2008, 23, 163-1644.

49. G. T. Teixidor, R. A. Gorkin, P. P. Tripathi, G. S. Bisht, M. Kulkarni, T. K. Maiti, T. K. Battacharyya, J. R. Subramaniam, A. Sharma, B. Y. Park, M. Madou, Carbon microelectromechanical systems as a substratum for cell growth. 2008, Biomed. Mater., 3, 034116 (8pp).

CHAPTER 3

METHODOLOGY

3.1. Comsol Multiphysics simulation

The simulation conducted in this thesis has been based on COMSOL Multiphysics. COMSOL Multiphysics is a powerful interactive environment for modeling and solving all kinds of scientific and engineering problems. The software provides a powerful integrated desktop environment with a model builder where the users get full overview of the model and access to all functionality. When solving the models, COMSOL Multiphysics uses the proven finite element analysis. The software runs the finite element analysis together with adaptive meshing and error control using a variety of numerical solvers. COMSOL Multiphysics creates sequences to record all steps that create the geometry, mesh, studies and solver settings, and visualization and results presentation. Partial differential equations (PDEs) form the basis for the laws of science and provide the foundation for modeling a wide range of scientific and engineering phenomena.

The main product is COMSOL desktop which is an integrated user interface environment designed for cross-disciplinary product development with a unified workflow for electrical, mechanical, fluid, and chemical applications. The optional modules are optimized for specific application areas and offer discipline-standard terminology and physics interfaces. In this thesis, several optional modules (AC/DC module, batteries & fuel cells module, chemical reaction engineering module) have been incorporated as well. The AC/DC module provides a unique environment for simulation of AC/DC electromagnetics in 2D and 3D modeling. The module is designed for detailed analysis of coils, capacitors, and electrical machinery. The batteries & fuel cells module provides customized physics interfaces for modeling of batteries and fuel cells. These

physics interfaces provide tools for building detailed models of the configuration of the electrodes and electrolyte in electrochemical cells. They include descriptions of the electrochemical reactions and the transport properties that influence the performance of batteries, fuel cells, and other electrochemical cells. The tailored physics interfaces mentioned above are also complemented with extended functionality in other physics interfaces for chemical species transport, heat transfer, and fluid flow. The heat transfer physics interfaces include heat sources that describe ohmic losses in the electrodes and electrolyte and heat sources due to electrochemical reactions in electrochemical cells. The fluid flow capabilities are extended for laminar flow, where the chemical species transport and the energy balances influence the properties of the flow. The chemical reaction engineering module uses reaction formulas to create models of reacting systems. It can solve the material and energy balances for both steady state models and transient models.

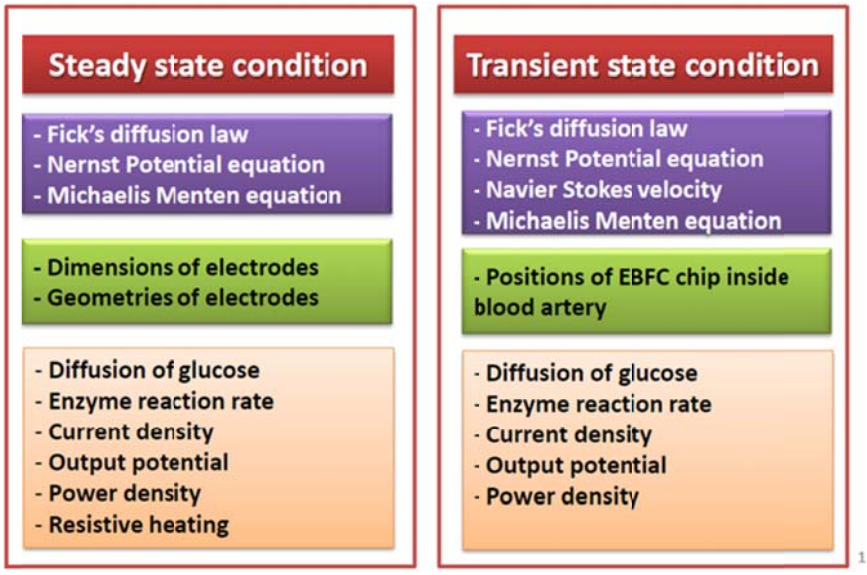

Figure 3.1 Simulation flow chart

In this work, a computational model of an enzymatic biofuel cell system to simulate mass transport, enzyme kinetics and electric current were evaluated by COMSOL multiphysics. Both steady state and transient state conditions have been considered shown in Figure 3.1.

The efficiency of utilization of the fuel is directly related to the enzyme kinetics. The Michaelis-Menten kinetics for a single-substrate reaction is considered for anode and cathode, respectively. The steady state kinetics of the enzyme reaction (v) is expressed by:

$$v=(k\_cat\ [E])/(1+K\_M/[S])$$

where kcat is catalytic rate constant, KM is the Michaelis Mention constant of the enzyme. [E] and [S] are the concentration of the enzyme and the substrate. . In the diffusion module, the diffusion of substrate with enzyme kinetics is solved based on reaction-diffusion equations:

$$(\partial c)/\partial t+\nabla(-D\cdot\nabla c) =v$$

where c is the concentration of substrate, D is the diffusion coefficient, v is the redox reaction rate. Conduction in this simulation occurs by a combination of electric field and diffusion, which is proportional to diffusion constant D and charge density. The current density is then described by generalized ohm's law:

$$J= \sigma\nabla ø+ zFD\nabla c$$

where σ is electric conductivity of the buffer and F is Faraday constant. In the above equation, electroneutrality condition is assumed.

The overall of redox reaction at the electrode surface is assumed to be reversible. The electrode potential-concentration relationship is defined by Nernst equation:

$$ø = ø\text{^}o+RT/zFln\ (([ø\_ox])/([ø\_red]))$$

where ø^o is the standard potential, [ø_ox] and [ø_red] represent the concentration of the oxidized and reduced enzyme. The mathematical considerations the incompressible Navier–Stokes equations for Newtonian fluids have been applied to represent the flow in the blood artery.

$$\partial_t \mathbf{v} + (\mathbf{v} \cdot \nabla)\,\mathbf{v} - \nabla \cdot (2\nu D\mathbf{v}) + \nabla p = \mathbf{f}$$

where v is flow velocity, v is kinematic viscosity, p represents the specific thermodynamic work and f is body acceleration.

In the steady state condition simulation, a model to mimic experiment in the lab condition has been developed. In the transient condition simulation, the blood artery environment has been simulated. The boundary condition for both simulations is shown in the Table 3.1, 3.2.

Boundary	**Diffusion**	**Potential**
Top boundary of bulk domain	Inward flux	Insulation
Bottom boundary of bulk domain	Convective flux	Insulation
Bulk-enzyme interface	Continuity	Potential expressions
Enzyme-electrode interface	Zero inward flux	Continuity
SiO_2 layer	Insulation	Insulation

Table 3.1. The boundary condition for steady state modeling

Boundary	Diffusion	Potential	Pressure
Top boundary of bulk domain	Inward flux	Insulation	Inlet pressure
Bottom boundary of bulk domain	Convective flux	Insulation	Outlet pressure
Bulk-mediator interface	Continuity	Potential expressions	Continuity
mediator-electrode interface	Zero inward flux	Continuity	Wall-no slip
SiO2 layer	Insulation	Insulation	Insulation

Table 3.2. The boundary condition for transient state modeling

3.2 C-MEMS

Carbon MEMS, or C-MEMS describes a manufacturing technique in which carbon devices are made by converting a pre-patterned organic structure to glassy carbon under the high temperatures in an inert environment. It has been shown recently that 3D high-aspect-ratio carbon structures can be made from patterned thick SU-8 negative photoresist layers. The experimental setup and details of the C-MEMS process used in this thesis has been reported previously [1-8]. Illustration of the typical C-MEMS fabrication procedure is shown in Figure 3.2. In brief, the C-MEMS based 3D micropillar arrays are prepared by a two-step photolithography process followed by a pyrolysis step. In the first photolithography step, a two-dimensional circle (diameter of 8 mm) pattern as current collector is firstly created using NANOTM SU-8 25. The photoresist film is spin-coated onto a silicon oxide wafer (4” in diameter, (1 0 0)-oriented, n-type) at 500 rpm for

12 sec and 3000 rpm for 30 sec by using a Headway research^{TM} photoresist spinner, followed by soft bake at 65 °C for 3 min and hard bake at 95 °C for 7 min on a hotplate. The baked photoresist is patterned with a UV exposure dose of 300 mJ cm^{-2}. Post-exposure bake is conducted at 65 °C for 1 min and 95 °C for 5 min on a hotplate. Next, second photolithography process is employed using NANO^{TM} SU-8 100 photoresist to build cylindrical micropillar arrays on patterned circle. SU-8 100 is spin-coated at 500 rpm for 12 sec and 1500 rpm for 30 sec by using a Headway researchTM photoresist spinner. The spincoated photoresist is then soft baked at 65 °C for 10 min and hard baked at 95 °C for 45 min in an oven. The exposure is done using a UV exposure dose of 700 mJ cm^{-2}. Post-exposure bake was performed at 65 °C for 3 min and 95 °C for 10 min in an oven. Then the sample is developed by NANOTM SU-8 developer (Microchem, USA) for 5-10 min to wash away the remaining unexposed photoresist followed by isopropanol rinsing and nitrogen drying. Finally, the resulting SU-8 structures are pyrolyzed at 1000 °C for 1 h in a Lindberg alumina-tube furnace with a continuous flow at 500 sccm forming gas (95% nitrogen, 5% hydrogen) then naturally cooled down to room temperature.

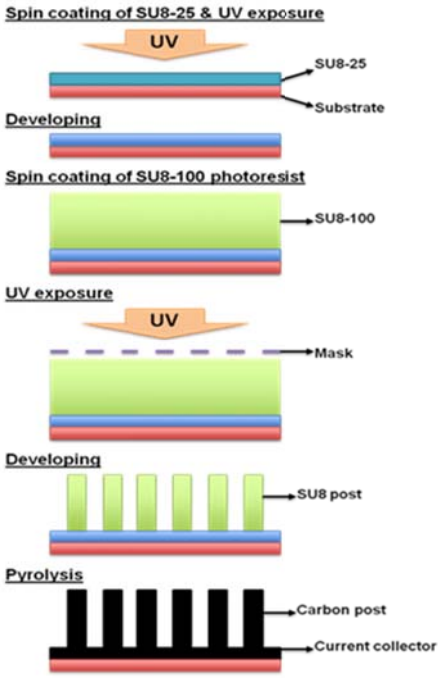

Figure 3.2 Schematic of C-MEMS

3.3 Diazonium surface functionalization

In order to immobilize enzyme covalently on the surface of electrode, the fabricated 3D carbon micropillar arrays are grafted with functional amino groups to form covalent binding with carboxyl groups in enzymes. The 4-(4'-nitrophenylazo) benzene diazonium tetrafluoroborate---a diazonium ion derivative is a highly reactive phenyl radical that can bind to glassy carbon surface irreversibly [9]. After placing the samples in diazonium salt aqueous solutions for 4 h, the 3D carbon micropillar arrays samples are conducted electrochemical reduction of nitro groups to amino group in an aqueous 0.1 M KCl solution with a scan rate of 50 mVs^{-1}. It is expected that all the electro-active nitro groups are electrochemically reduced to amino groups during the first negative sweep of the potential.

3.4 Electrophoretic deposition

EPD is a versatile method that has been successfully applied for the deposition of carbon nanotubes, graphite oxide, graphene as well as enzymes for electrochemical applications [10-11]. Particularly, the EPD method has a number of advantages such as high deposition rate, good thickness controllability, good uniformity and simple operation [12]. In this study, EPD method has been applied to fabricate composite bioanodes and biocathodes. Carbon based nanomaterials such as graphene, reduced graphene oxide, CNTs and enzyme are first dispersed in water and then the resultant solution is sonicated. The nanomaterials/enzyme composite migrated toward the positive electrode when a voltage of 10 V was applied for 3 min. During the EPD process, evolution of gas bubbles at the cathode is observed because of the water electrolysis, and the deposition occurred at the anode. The microstructures of EPD co-deposited nanomaterials/enzyme based 3D carbon micropillar arrays have been investigated by SEM.

3.5 Reference

1. C. Wang, L. Taherabadi, G. Jia, M. Madou, *Electrochem. Solid State Lett.,* 2004, 7, A435
2. C. Wang, G. Jia, L. Taherabadi, M. Madou, *Microelectromechanical Syst.,* 2005, 14, 348
3. C. Wang, M. Madou, *Biosens. Bioelectron.,* 2005, 20, 2181
4. B.Y. Park, L. Taherabadi, C. Wang, J. Zoval, M. Madou, *J. Electrochem. Soc.* 2005, 152, J136
5. K. Malladi, C. Wang, M. Madou, *Carbon,* 2006, 44, 2602
6. B. Park, Y.R. Zaouk, C. Wang, M. Madou, *ECS Trans.,* 2006, 1, 1
7. B.Y. Park, R. Zaouk, C. Wang, J. Zoval, M. Madou, *ECS Trans.* 2007, 4, 83
8. C. Wang, R.B. Zaouk, Y. Park, M. Madou, *Int. J. Manuf. Tech. Manag.* 2008, 13, 360

9. S. Pei, J. Du, Y. Zeng, C. Liu, H, Cheng, *Nanotechnol.,* 2009, 20, 235

10. S. Hong, S. Jung, S. Kang, Y. Kim, X. Chen, S. Stankovich, S. R. Ruoff, S. Baik, *J. Nanosci. Nanotechnol.,* 2008, 8, 424

11. M. Ammam, J. Fransaer, *Biosens. Bioelectron.*, 2009, 25, 191

12. S. J. An, Y. Zhu, S. H. Lee, M. D. Stoller, T. Emilson, S. Park, A. Velamakanni, J. An, R.S. Ruoff, *J. Phys. Chem. Lett.*, 2010, 1, 1259

CHAPTER 4

MODELING AND SIMULATION OF ENZYMATIC BIOFUEL CELLS WITH THREE-DIMENSIONAL MICROELECTRODES

4.1. Introduction

The last decade has seen an upsurge in the development of enzymatic biofuel cells (EBFCs) for their potential use as sustainable micropower sources in the implantable medical devices. In principle, EBFCs convert the biochemical energy in living organisms into electrical energy via various enzyme catalyzed redox reactions [1-6]. The EBFCs, in addition to powering the future generation of implanted medical devices, could also power biosensors for continuously monitoring chemical and physical conditions in environmental and military applications [7]. Recently, model biofuel cells were tested in vitro towards their ultimate goal as implanted micropower source in human bodies extracting power from glucose in blood [8-9]. However for an EBFC to successfully power an implantable medical device or autonomous sensor, significant reduction in size must be achieved while at the same time maintaining relatively high current and power. Normally, reducing size of EBFCs directly results in smaller amount of active electrode materials, which may significantly diminish the total energy and power output [10]. In this regard, in order to improve the power density of miniaturized EBFCs, researchers have proposed and investigated the novel micro/nano-electrode architectures, which offer increased surface area, superior physiochemical properties and enhanced electrode reactions. In particular, three-dimensional (3-D) microelectrode architectures have been considered as an attractive alternative solution due to the enhanced mass transport and higher electrode surface area compared to thin film two-dimensional (2-D) design in the same footprint area. Previous studies have shown that batteries with three dimensional

architectures have reached 350% larger energy capacity compared to traditional two-dimensional designs [11]. Moreover, the ion transport distance for the 3-D microelectrode based batteries during discharge is 3.5 times shorter than that in the thin film batteries [12]. Therefore, it could be predicted that 3-D microelectrode architectures might offer great opportunities to maximize output power density and reducing the mass transport distances between electrodes in the EBFCs.

Although the 3-D microelectrode architectures have significant advantages over the thin film electrodes, requisite multifunction-mass transport, conductivity and reaction kinetics must be considered for 3-D microelectrode designs for the EBFCs. Modeling can be highly useful to obtain optimized design rule when coupling with geometrical arrangement and reaction mechanisms. Anandan et al. [13] and Godino et al. [14] investigated the mass transport phenomenon in micro and nano-electrodes by using finite element analysis approach. Their study showed that the increased active surface area leads to enhanced electrochemical performance when the reaction rate constant of the target species is low. However, at higher reaction rate constants, only the top part of electrodes could transfer electrons. In addition, the principle that an array of microelectrodes could behave as a single electrode makes it necessary to investigate the design of the 3-D microelectrode array. Therefore, it is critical to optimize the microelectrode geometry and configuration for the 3-D array to obtain uniform current density distribution, enhanced mass transport and improved reaction kinetics, which could be translated to optimized EBFC performance.

Recently, a more economical alternative, carbon microelectromechanical systems (C-MEMS) technique involving the pyrolysis of patterned photoresist has developed a promising platform for a wide variety of potential applications such as lithium-ion

batteries, fuel cells, supercapacitors, electrochemical sensors and biosensors shown in Figure 1(a). Our group has been focusing on developing C-MEMS based micro/nanostructures [15-23], and building C-MEMS based electrodes for EBFCs [24-29]. One of the most important concerns is to achieve direct electron transfer (DET) between the enzyme reaction site and the electrode. In order to realize DET after enzyme immobilization, nano- or micro-structure of the electrode are widely used as a conductive agent, which would allow increasing the developed surface area of the electrode without modifying its geometric dimensions, where by developing a volumic network where enzyme can be entrapped or by creating pores enabling the adsorption of enzymes. In such an environment the number of orientations where each point of the enzyme surface is close enough to the electroactive surface to allow DET process. Carbon-based materials are the most widely used due to invaluable properties of carbon. Among the most cited are single-wall and multi-wall carbon nanotubes, carbon black, carbon nanoparticles, hollow carbon spheres, graphene, mesoporous carbon [30-38].

In this study, in order to obtain the optimum design of the 3-D microelectrode arrays for practical C-MEMS based EBFCs application, numerical simulations have been conducted by utilizing batteries & fuel cell module from COMSOL Multiphysics 4.3b commercial software (license No. 1023246), which solves partial different equations by finite element technique. In order to simplify the simulation, the 2-D modeling has been applied in this research.a C-MEMS based 3-D microelectrode array will be simulated as electrode for EBFC. A 10 μm conductive layer composed of mesoporous carbon and enzyme is proposed. We assumed that this mesoporous carbon structure has well-ordered porosity allowing enzyme entrapment and substrate diffusion. One of our recent efforts on simulation was targeted towards orientation of a C-MEMS based EBFC chip with 3-D

microelectrode arrays inside a blood artery. However, we only investigated the stability of an EBFC chip placing in different orientations in the blood flow and novel design to minimize the convective flux and optimize the mass transport around microelectrode arrays [39]. More detailed work regarding cell performance of microelectrode arrays based on both mass transport and enzyme kinetics have not been considered. In this work, we have conducted a detailed simulation study on the effect of dimensions and spatial arrangement of 3-D microelectrode arrays on the EBFC performance by incorporating the mass transport and enzymatic kinetics. In addition, four different electrode geometries were simulated to evaluate the distribution of current density on the electrodes.

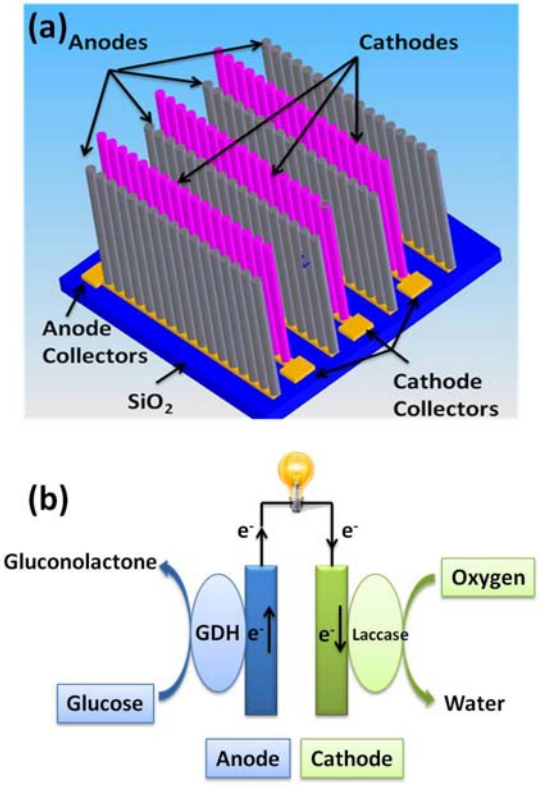

Figure 4.1 (a) A miniaturized EBFC with 3D interdigitated microelectrode arrays. (b) Schematic depiction of EBFC reaction mechanism.

4.2. Mechanism of EBFCs

Among today's glucose-oxidizing enzymes, glucose oxidase (GOx) has been the most widely used redox enzyme due to its thermostability and high selectivity for glucose. However, glucose oxidase is defined as oxidoreductases that can utilize oxygen as the external electron acceptor, which will cause the oxygen competetion between GOx and laccase catalysis. Therefore, glucose dehydrogenase (GDH), which is insensitive to oxygen has been considered in this study for simplicity. Figure 1(b) shows the schematic of 3-D microelectrodes immobilized with (GDH) and laccase on anode and cathode, respectively. The overall redox reaction of this EBFC is given by:

Anode: $\text{Glucose} \xrightarrow{\text{GDH}} \text{Gluconolactone} + 2H^+ + 2e^-$ (1)

Cathode: $O_2 + 4H^+ + 4e^- \xrightarrow{\text{laccase}} 2H_2O$ (2)

In principle, glucose is catalyzed by GDH and produces gluconolactone and hydrogen ions and generates electrons on the anode. On the cathode, laccase catalyst reduces oxygen and water is generated by combining with electrons and hydrogen ions. Laccase is multi-copper protein that can catalyze the four electron reduction of oxygen to water. It is believed that laccase catalysis involves reduction of the copper by reducing substrate. The FAD-GDH comprises oxidoreductases that catalyze the first hydroxyl group of glucose and other sugar molecules, utilizing FAD as the primary electron acceptor. When GDH catalyzes glucose oxidation, the GDH-FAD is reduced to GOx-$FADH_2$, which can be oxidized by the electrode back to GDH-FAD shown in the following reaction.

$$\text{GDH-FAD} + \text{Glucose} \longrightarrow \text{GDH-FADH}_2 + \text{Gluconolactone} \quad (3)$$

$$\text{GDH-FADH}_2 \longleftrightarrow \text{GDH-FAD} + 2H^+ + 2e^- \quad (4)$$

For this modeling, we will consider that enzyme (GDH-FAD/laccase) and electrode reactions are coupled by DET in this simulation. In such a system, the coupled overall

process is the redox transformation of the substrates, which can be considered as an enzyme-catalyzed electrode process.

The efficiency of utilization of the fuel is directly related to the enzyme kinetics. The Michaelis-Menten kinetics for a single-substrate reaction is considered for anode and cathode, respectively.

$$S + E \underset{k_{-1}}{\overset{k_1}{\rightleftarrows}} ES \xrightarrow{k_2} P + E \tag{5}$$

where S and P are the substrate and product, E is the enzyme; ES is enzyme and substrate complex by initial bimolecular reaction, k_1, k_{-1} are the rate constants for the association and breakdown, respectively of the complex and k_2 denote the rate constants for the breakdown of the complex. The steady state kinetics of the enzyme reaction (v) is expressed by:

$$v = \frac{k_{cat}[E]}{1+K_M/[S]} \tag{6}$$

where k_{cat} (= k_2) is catalytic rate constant, K_M (= (k_2 + k_{-1})/k_1) is the Michaelis Mention constant of the enzyme. [E] and [S] are the concentration of the enzyme and the substrate.

4.3 Simulation

A computational model of an EBFC system to simulate mass transport, enzyme kinetics and electric current were developed by COMSOL multiphysics, which solves partial differential equations (PDEs) by finite element techniques. The schematic of a prototype design of an EBFC chip, having 3-D microelectrode arrays was proposed as shown in Fig 1(a). The foot print was chosen as 15 by 15 mm in square. The diameter for each microelectrode is 30 μm and enzyme layer thickness is 10 μm. The height of the microelectrode has been chosen from 100 μm to 200 μm based on current C-MEMS

technology. In order to simplify the simulation, the 2-D modeling has been applied in this study. With the microelectrode dimension and foot print area, the change of distance between two electrodes (well width) is from 10-200 μm, which will affect the number of microelectrodes within the same foot print in one row on the chip. In our previous paper, the pressure variation in each cardiac cycle is considered with a simple trigonometry function to maintain normal systolic/diastolic pressure variation of 120/80 mmHg in the artery [39]. The glucose amount flowing in the artery will also change at the inlet according to contraction and extraction of blood artery which is considered as a transient model. In this study, in order to obtain the optimized design for 3-D microelectrode arrays, we simulate the model considering the 3-D microelectrode arrays is in the experimental beaker with glucose concentration at 5 $mol \cdot m^{-3}$. In the diffusion module, the diffusion of substrate with enzyme kinetics is solved based on reaction-diffusion equations:

$$\frac{\partial c}{\partial t} + \nabla(-D \cdot \nabla c) = v \tag{7}$$

where c is the concentration of substrate, D is the diffusion coefficient, v is the redox reaction rate.

To compute the electric field $\nabla ø$, we need to solve the continuity equation for current $\nabla J = 0$. Current density is proportional to the conductivity and electric field $J = \sigma \nabla ø$. Conduction in this simulation occurs by a combination of electric field and diffusion, which is proportional to diffusion constant D and charge density. The current density is then described by generalized ohm's law:

$$J = \sigma \nabla \phi + zFD\nabla c \quad (8)$$

where σ is electric conductivity of the buffer and F is Faraday constant. In the above equation, electroneutrality condition is assumed.

The overall of redox reaction at the electrode surface is assumed to be reversible. The electrode potential-concentration relationship is defined by Nernst equation:

$$\phi = \phi^o + \frac{RT}{zF} \ln\left(\frac{[\phi_{ox}]}{[\phi_{red}]}\right) \quad (9)$$

where ϕ^o is the standard potential, $[\phi_{ox}]$ and $[\phi_{red}]$ represent the concentration of the oxidized and reduced enzyme. In this simulation, we consider the concentration of the oxidized and reduced forms are from the active redox center of FAD/$FADH_2$ for GDH and type 1 copper for laccase.

The boundary conditions and the relevant constants are shown in Table 4.1 and Table 4.2, respectively.

Boundary	**Diffusion**	**Potential**
Top boundary of bulk domain	$c = c_0$	$n \cdot J = 0$
Bulk-enzyme interface	$-n(N_1 - N_2) = 0$	$V = V_0$
Enzyme-electrode interface	$-n(N_1 - N_2) = 0$	$n(J_1 - J_2) = 0$
Side and bottom boundaries of bulk domain	$-n(-D\nabla c) = 0$	$n \cdot J = 0$

Table 4.1. Boundary conditions for simulation models

Constant	**Ref. Value**	**Reference**
R	8.314 J·mol·K^{-1}	
T	300 K	
F	96485 C·mol^{-1}	
$D_{glucose}$	$7 \cdot 10^{-10}$ $m^2 \cdot s^{-1}$	[40-42]
D_{oxygen}	$1.74 \cdot 10^{-9}$ $m^2 \cdot s^{-1}$	[43, 44]

$K_{M\ GDH}$	17.4 mM	[45]
$K_{M\ laccase}$	133.4 mM	[46]
k_{cat_GDH}	360 s^{-1}	[45]
$k_{cat\_laccase}$	117 s^{-1}	[46]
$ø^{o}_{A}$	-0.32 V	[47]
$ø^{o}_{C}$	0.585 V	[47]
σ_{carbon}	8000 $S \cdot m^{-1}$	[48]
$\sigma_{substrate}$	4 $S \cdot m^{-1}$	

Table 4.2. Simulation parameters

In addition, several assumptions have been made in this simulation.

1) 2-D simulation is used to simplify the 3-D microelectrode design.

2) The DET between enzyme and electrode is aussumed.

3) The enzyme kinetics constant is obtained from the literatures based on immobilized enzymes.

4) The enzyme is uniformly distributed in the enzyme layer.

5) Negligible change in heat transfer is assumed between enzyme layer and electrode interface.

6) Temperature distribution around the EBFCs is assumed to be uniform.

4.4 Results and discussions

4. 4.1 Steady state response

Initially at time t=0, the concentration of the glucose is constant along the electrode. From t>0, the glucose starts to react with enzyme. The glucose depletion from the reaction from the bottom of the electrode causes the glucose diffusion from the bulk domain to the well between electrodes. We theninvestigated the response time for glucose

to diffuse within one pair of microelectrode before reaching a steady stateFigure 2 illustrates the steady state response time for electrode with height of 200 μm and well width of 40 μm. The glucose concentration is from the top point of the electrode. Based on the glucose concentration evolution over operation time, the steady state response time for microelectrode arrays at this dimension is around 700s. In the following study, we investigate the EBFC performance after the steady state condition has been met for each configuration of microelectrode array.

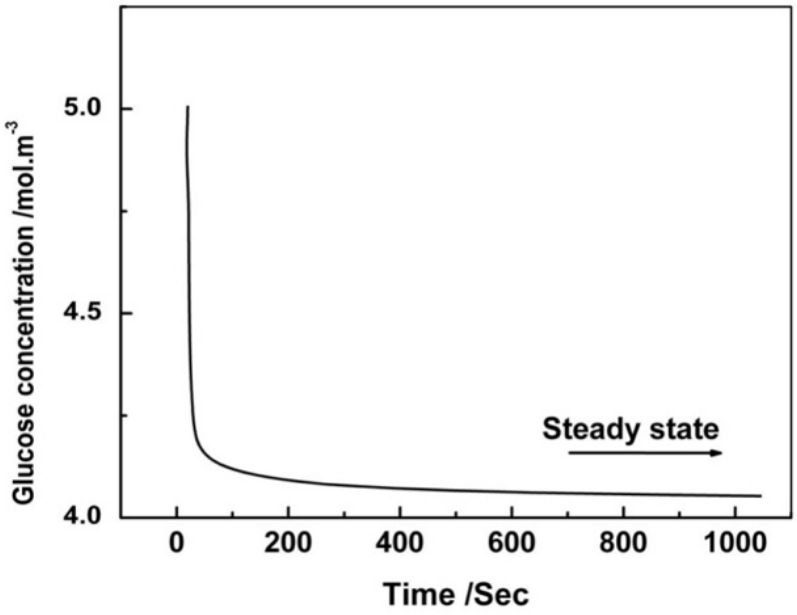

Figure 4.2. Response time to reach steady state for electrode at height of 200 μm with well width of 100 μm.

4.4.2 Impact of mass transport and reaction rate

Mass transport is investigated based on glucose and oxygen diffusion around electrodes in different configurations of microelectrode arrays. The glucose concentrations along the electrode surface inside the well at different electrode dimensions after reaching steady state are shown in Figure 3(a-b). The starting point is

0.05 μm from the bottom to the top of the electrode. Ideally, glucose should interact with the total surface area of electrodes from top to bottom to fully utilize the enzymes immobilized onto them. However, the glucose reacts immediately with the top portion of the electrode where it diffuses first and the rest of glucose reacts gradually down to the bottom of the electrode. From the results, we observed the non-uniformity of the concentration of glucose along the surface of electrode at all dimensions. There is a decrease in the glucose concentration along the vertical direction inside the well from the top to bottom of the electrode. We have simulated a microelectrode array with height of 200 μm with two well widths of 40 and 100 μm. The smaller glucose depletion occurs for the larger well width between two electrodes because there is more space for glucose. In order to investigate the effect of height on diffusion change, different height of microelectrode arrays at a fixed well width of 50 μm have been simulated and results were shown in Figure 3c. The glucose concentration is decreased from the top to the bottom of the electrode for all different height of microelectrode arrays. The concentration of the bottom of the electrode decreases as the height of the electrode increase. The competition between higher enzyme reaction rate and lower diffusion rate causes glucose depletion throughout the electrode surface and consequently generates non-uniform glucose concentration. Since the concentration gradient on the electrode surface is influenced by the enzyme kinetics defined by the Michaelis-Menten reaction rate equation (6), the concentration gradient of the glucose and oxygen along the vertical direction from top to bottom of electrode surface leads to the relevant enzyme reaction variation in the enzyme layer shown in Figure 4. From the simulation results, the enzyme reaction rate decreases from the top to bottom along the surface of microelectrodes, which is consistent with the result of concentration gradient. It is also observed that the

outer surfaces of the microelectrodes experience larger enzyme reaction rate in the enzyme layer due to the diffusion. In addition, the noticeable maximum enzyme reaction rate at the top edges of the microelectrodes results from the edge effect of the electrode design.

Even though by increasing the well width, the glucose concentration gradient has less difference along the microelectrode surface from the bottom to the top thus the glucose depletion is getting smaller, the number of microelectrodes within the same foot print area decreases. Because the current and power density is based on the total number of microeletrodes, it is necessary to find the optimum configuration of microelectrode arrays based on the simulation results from current density.

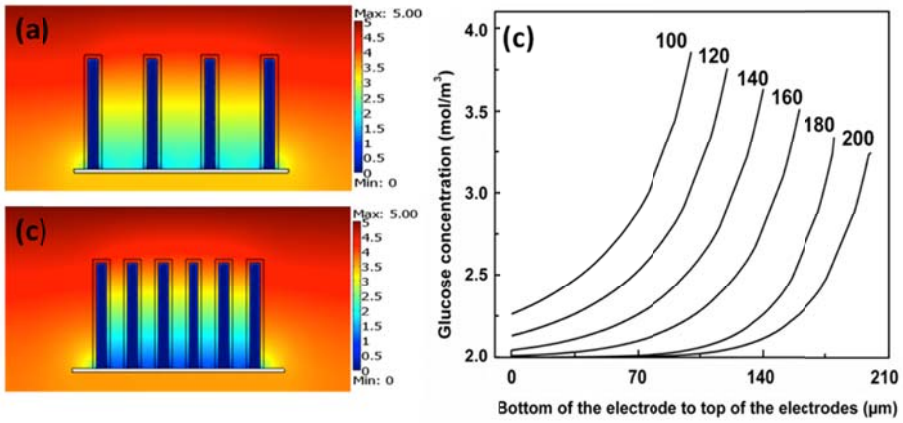

Figure 4.3. Glucose concentration from the bottom to the top of electrode at electrode height of 200 μm with different well width (ww) (a) 40 μm; (b) 100 μmrespectively. (c) Gluocse concentration from the bottom to the top of electrode at different height from 100 μm to 200 μm.

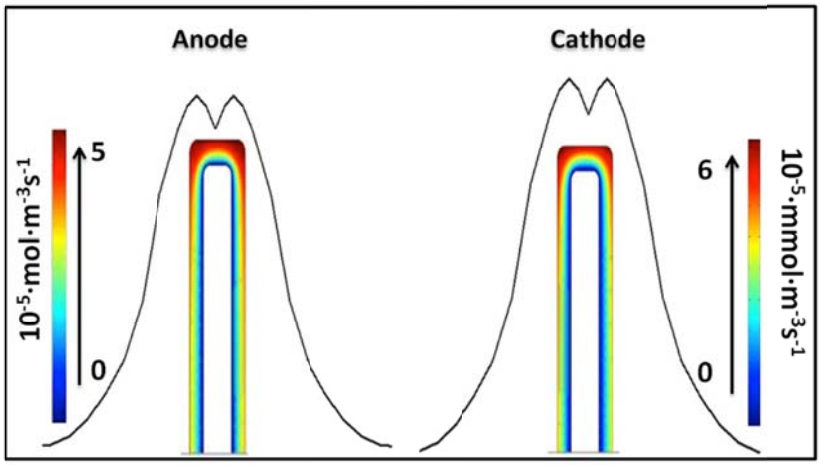

Figure 4.4. Change in reaction rate along the surface of anode and cathode at electrode height of 200 μm.

4.4.3 Cell performance of EBFCs

The current density of whole microelectrode arrays were simulated as shown in Figure 5(a-c). The Figure 5(a) and 5(b) are the current density profile for microelectrode arrays at the same height with different well width within the same foot print. From the previous diffusion result, the larger well width has better glucose diffusion along the electrode vertical surface. The substrate will react with the enzymes immobilized on the top of the electrodes first and at the meantime diffuse and react along the electrode surface from top to bottom. The competition between higher enzyme reaction rate and lower diffusion rate causes non-uniform electron transfer throughout the electrode surface and consequently generates non-uniform current density. The current density is relatively low from the bottom of the electrode and increase in the higher portion of the electrode. It is observed that the current density maximum occurs on the top corner of each electrode. Figure 5(c) is the corresponding current density plot for these two configurations of microelectrode arrays. The current density for larger well width (solid line) is higher than that of smaller

well width (dash line). As we discussed before, even though current density for larger well width is higher, increase in well width causes decrease in number of microelectrodes in the same foot print. Therefore, integration of the current density along the electrode surface in one row on the chip has been evaluated at different well width for each constant height of microelectrode arrays, which qualitatively represents the total current collected on each post-electrode in one row within the same foot print area. The change of the line current density with respect to the well width and height is obtained by simulation and shown in Fig 5(d). For each height, with the increase of well width the line current density reaches a peak and then decreases. This is because even though glucose depletion is less in the larger well width, the less micoelectrodes in one row could result in the decrease in total line current density. A conclusion can be drawn from the simulation results that the maximum line current density is obtained when the height is roughly equal to two times the well width. It could be noticed that among the three cases, microelectrode array with 200 μm exhibited the highest current density of 0.52 mA/cm^2. Ease of fabrication is an important consideration and since it is difficult to manufacture carbon microelectrodes higher than 200 μm by C-MEMS. Therefore, based on the results and practical application, to design the microelectrode arrays within 15mm x15mm foot print, the optimum configuration is height and well width keeping as 200 μm and 100 μm.

One of the most important characteristics to examine in an EBFC is power density. In this work, simulation was conducted by incorporating the Nernst equation. To compare the performance among different electrode configurations, we simulated EBFCs with threeheights: 100 μm, 150 μmand 200 μm, all at 2:1 fixed ratio of height to well width based on the previous results, which the optimized configuration of microelectrodes is

that the height is twice of the well width. Various external loads at the range of 5-500 kΩ are considered in the simulation in order to understand the power density-voltage relationship. As shown in Figure 5(e), the power density for all four configurations of microelectrodes increases as the voltage gets higher and reaches a maximum. After reaching the maximum, increasing the voltage leads to a decrease in the power density. The electrode array with height of 200 μm is observed to have the highest power density at around 110 μW/cm^2 when the voltage is approximately 0.44 V. This performance of EBFC is adequate for operation of low-voltage CMOS integrated circuits.

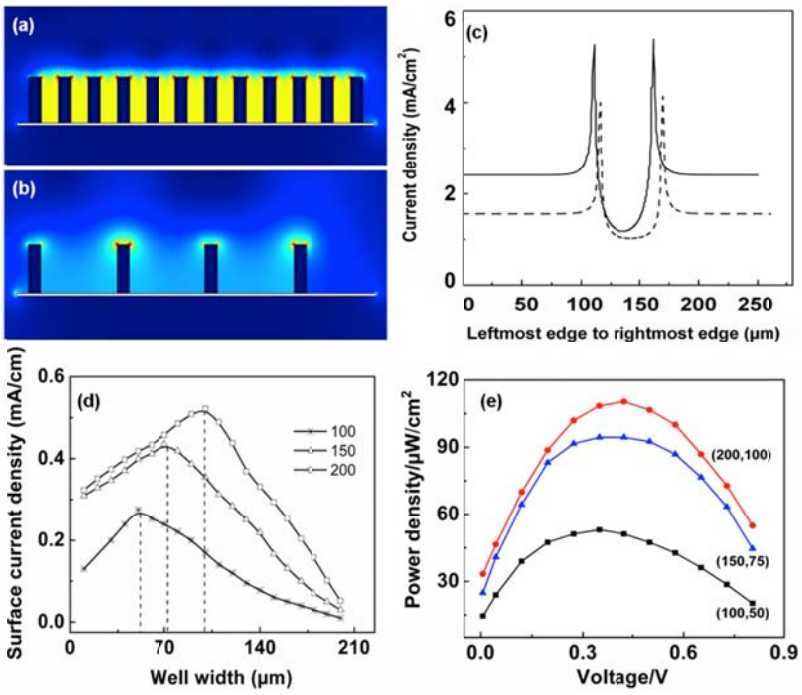

Figure 4.5. (a-b) Current density profile for one row of microelectrodes at 100 μm with different well width 50 μm and 100 μm. (c) Current density at the surface of electrode along the vertical direction inside the well: 50 μm (dash line); 100 μm (solid line). (d) Change of line current density with respect to electrode height and well width. (e) Power density vs. cell voltage at different electrode heights. The height to well width ratio of electrode is 2:1.

4.4.4 Geometry of the electrodes

The simulation profile of electric field is shown in Figure 6 for rectangular electrodes. The contour plot also shows the electric field; with more contours at higher value of electric field and less contours at lesser values of electric field. The arrow plot shows the direction of the charge transfer, with tails coming out of cathodes and heads going into anodes. The electric field is inversely proportional to the distance between electrodes and hence it is higher in between the post rather than in surrounding region. At the corners and sharp edges as area decreases the charge density increases and so does the electric field, because the electric field is perpendicular to the surface area and proportional to the charge density. According to Ohm's law, current density is directly proportional to electric field, and hence the current density is higher at sharp corners and edges. This may result in more heat dissipation/resistive heating and so electrodes can eventually degrade at those portions of electrodes. This higher heating can cause harm to enzymes immobilized onto posts. This may reduce the life span of enzymes, which can reduce the fuel cell longevity. In order for the electrodes and enzymes to last for long time, current density should be uniform around electrodes and edge effect should be minimized.

From above discussions, it is inferred that not only dimensions, but geometry of the electrodes also plays an important role in EBFC output performance. To find out more reliable and long lasting electrode configurations, four different geometries of one pair of electrodes with height of 100 μm, well width of 20 μm at bottom and diameter of 20 μm is implemented in order to obtain a more suitable configuration with uniform current density along the single electrode. In all these simulations, the open circuit potential for anodes is at -0.32 V (vs. SHE) and cathodes at 0.585 V (vs. SHE). For the anode, when the potential is in the interval from - 0.32 V to 0 V (vs. SHE), dissolved O_2 would get

reduced on the carbon and then decrease the current, voltage and faradic efficiency [49]. In order to simplify the simulation, we don't take into account any putative O_2 reduction on the anode. The current density and resistive heating profiles for a) rectangular, b) triangular, c) tapered, and d) semi-elliptical electrodes with height of 100 µm, well width of 20 µm at bottom and diameter of 20 µm are shown in Figure 7 (a-d), respectively. In the figures, the left Y-axis and the right Y-axis show the values for current density and resistive heating, respectively. The current density and resistive heating profiles follow almost the same trend for all the four geometries since heat dissipation is proportional to current density. The values for current density and resistive heating, for all the geometries, are summarized in

Geometry Property	Side Edges		Top Edge		Corners	
	CD ($\mu A \cdot cm^{-2}$)	RH ($\mu W \cdot cm^{-3}$)	CD ($\mu A \cdot cm^{-2}$)	RH ($\mu W \cdot cm^{-3}$)	CD ($\mu A \cdot cm^{-2}$)	RH ($\mu W \cdot cm^{-3}$)
Rectangular	170	4	100	1.5	410	23
Triangular	90–225	1–8	-	-	270(top) 230(bottom)	12(top) 7(bottom)
Tapered	130–210	2.5–5	125–135	1–3	250	8.5
Semi-elliptical	45–90	0.05–0.17	-	-	105(top) 47(bottom)	0.27(top) 0.05(bottom)

Table 3.3.

Geometry Property	Side Edges		Top Edge		Corners	
	CD ($\mu A \cdot cm^{-2}$)	RH ($\mu W \cdot cm^{-3}$)	CD ($\mu A \cdot cm^{-2}$)	RH ($\mu W \cdot cm^{-3}$)	CD ($\mu A \cdot cm^{-2}$)	RH ($\mu W \cdot cm^{-3}$)
Rectangular	170	4	100	1.5	410	23
Triangular	90–225	1–8	-	-	270(top) 230(bottom)	12(top) 7(bottom)
Tapered	130–210	2.5–5	125–135	1–3	250	8.5
Semi-elliptical	45–90	0.05–0.17	-	-	105(top) 47(bottom)	0.27(top) 0.05(bottom)

Table 4.3 Statistical analysis of current density (CD) and resistive heating (RH) for rectangular, triangular, tapered and semi-elliptical geometry of electrodes

From the simulation results, it could be observed that the current density values are very high at the tip corners of the rectangular electrodes. The resistive heating is almost 5 times higher at tip corners compared to other locations due to the edge effect. In contrast, for the other majority locations of side and top of electrodes, the current density and resistive heating is uniformly distributed. In triangular electrodes, those localized high current density and resistive heating regions, are located at the tips of the electrodes, with values much more stronger than the values taken from the side walls. In the case of tapered electrodes, the non-uniformity of current density and resistive heating are much less compared to the rectangular and triangular electrode geometries. In semi-elliptical electrodes, the current density and resistive heating values are more uniformly distributed compared to all other geometries. The resistive heating values are very small at the top curvature as well as at edges. According to Ohm's law, current density is directly proportional to electric field, and hence the current density is higher at sharp corners and edges. From these simulation results, semi-elliptical shaped geometry is more favorable due to lack of sharp corners and edges. But it should be noted that although semi-elliptical electrodes provides the least resistive heating, it might not be easy to fabricate such microstructures using conventional C-MEMS technology.

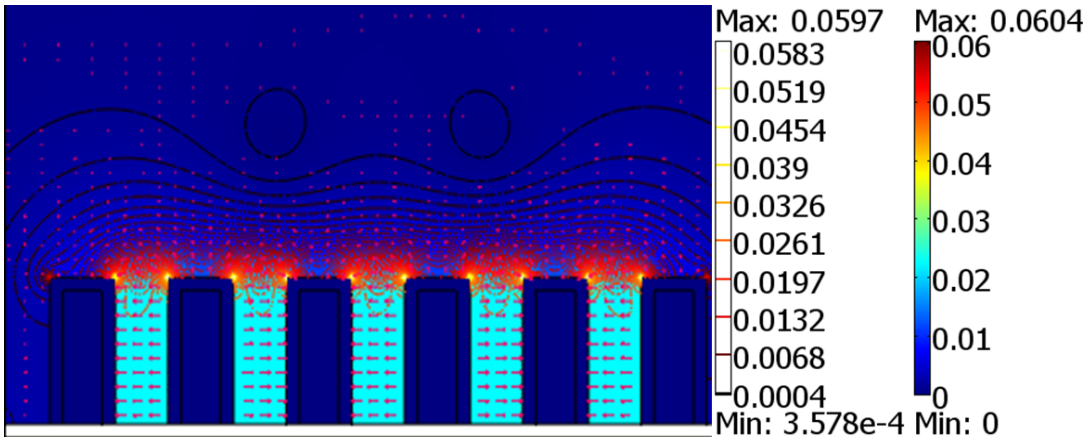

Figure 4.6. Electric field (surface, contour and arrow plot) profile surrounding the rectangle electrodes with constant potential of 0.585 V on cathode and -0.32 V on anode.

In order to truly check the plausibility of different computational models for EBFCs, effort is needed on experimental work, including fabrication techniques of different shapes of electrodes. At the same time, other essential EBFCs parameters such as overpotential, internal cell resistances as well as the cell performance in transient condition should be also investigated in the future work.

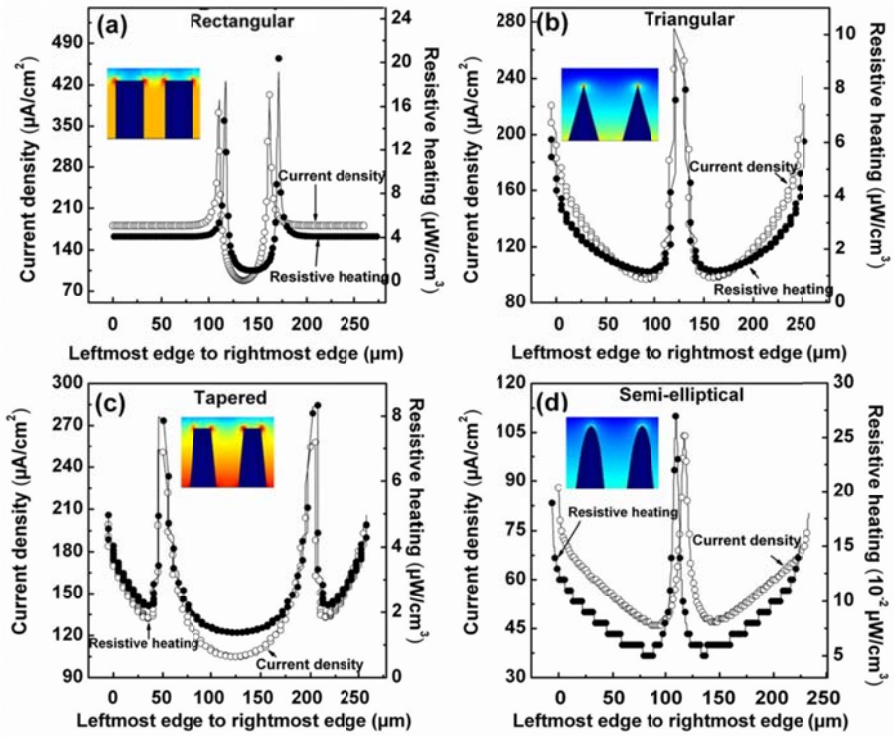

Figure 4.7. Current density and resistive heating distribution plots for four different geometries of electrodes: a) rectangular, b) triangular, c) tapered and d) semi-elliptical.

4.5 Conclusions

In this paper, a detailed simulation on 3-D microelectrode EBFC arrays is investigated. The novelty of this report is the incorporation of enzyme kinetics in the EBFC modeling. Optimization of the EBFC configuration suggests that in order to maximize the cell

performance within the fixed print area, the ratio of the height and the well width of the electrode should be kept as 2:1 in general. From the modeling, the maximum power density for 3-D microelectrode EBFC reaches 110 $\mu W/cm^2$ at 0.44 V in voltage when the dimension of electrodes is keeping height as 200 μm and well width as 100 μm. From current density and resistive heating distribution analysis for different geometries of electrodes, we highly recommend that semi-elliptical shaped electrode is more favorable to deliver uniform current density along the electrode.

4.6 References

1. Mano, N.; Heller, A. Biofuel cells and their development. *J. Electrochem. Soc.* 2013, 150, A1136-A1138.

2. Palmore, G.; Whitesides, G.M. Microbial and enzymatic biofuel cells. In: Enzymatic conversion of biomass for fuels production, E. Himmel, Editor, vol. 566, American Chemical Society, 1994, 271-290.

3. Ivnitski, D.; Branch, B.; Atanassov, P.; Apblett, C. Glucose oxidase anode for biofuel cell based on direct electron transfer. *Electrochem. Commun.* 2006, 8, 1204-1210.

4. Katz, E.; Shipway, A.N.; Willner, I. *Handbook of Fuel Cells—Fundamentals, Technology and Applications*, 2003, John Wiley & Sons, Ltd., Hoboken, NJ, 355-381.

5. Heller, A. Miniature biofuel cells. *Chem. Chem. Phys.* 2004, 6, 209-216.

6. Ramanavicius, A.; Kausaite, A.; Ramanaviciene, A. Biofuel cell based on direct bioelectrocatalysis. *Biosens. Bioelectron.* 2005, 20, 1962-1967.

7. Halamkova, L.; Halamek, J.; Bocharova, V.; Szczupak, A.; Alfonta, L.; Katz, E. Implantable biofuel cell operating in a living snail. *J. Am. Chem. Soc.* 2012, 134, 5040-5043.

8. Coman, V.; Ludwig, R.; Harreither, W.; Haltrich, D.; Gorton, L.; Ruzgas, T.; Shleev, S. A Direct Electron Transfer-Based Glucose/Oxygen Biofuel Cell Operating in Human Serum. *Fuel Cells* 2010, 10, 9-16.

9. Southcott, M.; MacVittie, K.; Halámek, J.; Halámková, L.; Jemison, WD.; Lobel, R.; Katz, E. Pacemaker Powered by Implantable Biofuel Cell Operating Under Conditions Mimicking Human Blood Circulatory System–Battery Not Included, Phys. Chem. Chem. Phys., 2013,15, 6278-6283

10. Ringeisen, B. R.; Henderson, E.; Wu, P.; Pietron, J.; Ray, R.; Little, B.; Biffinger, J.; Jones-meehan, J. High power density from a miniature microbial fuel cell using shewanella oneidensis DSP10. *Environ. Sci. Technol.* 2006, 40, 2629-2634.

11. Long, J.W.; Dunn, B.; Rolison, D.; White, H.S. Three-Dimensional battery architectures. *Chemical Reviews*, 2004, 104, 4463-4492.

12. Dunn, B.; Long, J.W.; Rolison, D. Rethinking multifunction in three dimensions for miniaturizing electrical energy storage. *Interface* 2008, 17, 49-53.

13. Anandan, V.; Yang, X.; Kim, E.; Rao, Y.; Zhang, G. Role of reaction kinetics and mass transport in glucose sensing with nanopillar array electrodes. *J. Biol. Eng.* 2007, 1, 1-10.

14. Godino, N.; Borrise, X.; Munoz, F. X.; Campo, F. J.; Compton, R. Mass transport to nanoelectrode arrays and limitations of diffusion domain approach: Theory and experiment. *J. Phys. Chem.* 2009, 113, 11119-11125.

15. Wang, C.; Taherabadi, L.; Jia, G.; Madou, M. C-MEMS for the manufacture of 3D microbatteries. *Electrochem. Solid State Lett.* 2004, 7, A435-438.

16. Wang, C.; Jia, G.; Taherabadi, L.; Madou, M. *J.* A novel method for the fabrication of high aspect ratio C-MEMS structures. *Microelectromechanical Systems* 2005, 14, 348-358.

17. Wang, C.; Madou, M. From MEMS to NEMS with carbon. *Biosens. Bioelectron.* 2005, 20, 2181-2187.

18. Park, B. Y.; Taherabadi, L.; Wang, C.; Zoval, J.; Madou, M. Morphological and electrical properties of carbon films of various thinknesses carbonized from photoresist and the implications for C-MEMS devices in conductive media. *J. Electrochem. Soc.* 2005, 152, J136-J143.

19. Malladi, K.; Wang, C.; Madou, M. Microfabrication of suspended C-MEMS structures by EB writer and pyrolysis. *Carbon* 2006, 44, 2602-2607.

20. Park, B. Zaouk, Y. R.; Wang, C.; Madou, M. Fractal C-MEMS architectures for 3D miniature power and sensor applications. *ECS Trans.* 2006, 1, 1-11.

21. Park, B. Y.; Zaouk, R.; Wang, C.; Zoval, J.; Madou, M. Fractal C-MEMS electrodes: theory and preliminary fabrication. *ECS Trans.* 2007, 4, 83-92.

22. Wang, C.; Zaouk, R. B.; Park, Y.; Madou, M. Carbon as a MEMS material: Micro and nano fabrication of pyrolyzed photoresist carbon. *Int. J. Manuf. Tech. Manag.* 2008, 13, 360-375.

23. Min, H.; Park, B. Y.; Taherabadi, L.; Wang, C.; Yeh, Y.; Zaouk, R.; Madou. M.; Dunn, B. Fabrication and properties of a carbon/polypyrrole three-dimensional microbattery. *J. Power Sources*, 2008, 178(2), 795-800.

24. Yang, J. H.; Penmatsa, V.; Tajima, S.; Kawarada, H.; Wang, C. Direct amination on 3D pyrolyzed carbon micropattern surface for DNA detection. *Material Lett.* 2009, 63, 2680-2683.

25. Chen, W.; Beidaghi, M.; Penmatsa, V.; Li, W.; Wang, C. Integration of carbon nanotubes to C-MEMS for on-chip supercapacitors. *IEEE nanotech* 2010, 9, 1222-1225.

26. Penmatsa, V.; Yang, J. H.; Yu, Y.; Wang, C. Porous 3D carbon electrodes using F127 as porogen preparation. *Carbon* 2010, 48, 4109-4115.

27. Penmatsa, V.; Kawarada, H.; Wang, C. Fabrication of carbon nanostructures using photo nanoimprint lithography and pyrolysis. *J. Micromech. Microeng.* 2012, 22, 045024.

28. Penmatsa, V.; Kim, T.; Beidaghi, M.; Kawarada, H.; Wang, Z.; Gu, L.; Wang, C. Three-Dimensional grapheme nanosheets encrusted carbon micropillar arrays for electrochemical sensing. *Nanoscale* 2012, 4, 3673-3678.

29. Penmatsa, V.; Ruslinda, R.; Beidaghi, M.; Kawarada, H.; Wang, C. Platelet-derived growth factor oncoprotein detection using three-dimensional carbon microarrays. Biosens. Bioelectron. 2013, 39, 118-123.

30. Miyake, T.; Yoshino, S.; Yamada, T.; Hata, K.; Nishizawa M. Self-regulating enzyme-nanotube ensemble films and their application as flexible electrodes for biofuel cells. J. Am. Chem. Soc. 2011, 133, 5129-5134.

31. Filip, J.; Sefcovicova, J.; Gemeiner, P., Tkac, J. Electrochemistry of bilirubin oxidase and its use in preparation of a low cost enzymatic biofuel cell based on a renewable composite binder chitosan Electrochim. Acta 2013, 87, 366-37.

32. Krishnan, S.; Armstrong, F.A. Order-of-magnitude enhancement of an enzymatic hydrogen-air fuel cell based on pyrenyl carbon nanostructures. Chem. Sci. 2012, 3, 1015-1023.

33. Miyake, T.; Haneda, K., Yoshino, S.; Nishizawa, M. Flexible, layered biofuel cell. Biosens. Bioelectron. 2013, 40, 45-49.

34. Tasca, F.; Harreither, W.; Ludwig, R.; Gooding, J.J.; Gorton, L. Cellobiose dehydrogenase aryl diazoniunn modified single walled carbon nanotubes: enhanced direct electron transfer through a positively charged surface. Anal. Chem. 2011, 83, 3042-3049.

35. Yan, Y.M.; Su, L.; Mao, L.Q. Multi-walled carbon nanotube-based glucose/O_2 biofuel cell with glucose oxidase and laccase as biocatalysts. J. Nanosci. Nanotechnol. 2007, 7, 1625-1630.

36. Lesniewski, A.; Paszewski, M.; Opallo, M. Gold-carbon three dimensional film electrode prepared from oppositely charged conductive nanoparticles by layer-by-layer approach. Electrochem. Commun. 2010, 12, 435-437.

37. Liang, B.; Fang, L.; Yang, G; Hu, Y.C.; Guo, X.S.; Y, X.S. Direct electron transfer glucose biosensor based on glucose oxidase self-assembled on electrochemically reduced carboxyl graphene. Biosens. Bioelectron. 2013, 43, 131-136.

38. Guo, C.X.; Hu, F.P.; Lou, X.W.; Li, C.M. High-performance biofuel cell made with hydrophilic ordered mesoporous carbon as electrode material. J. Power Sources 2010, 195, 4090-4097.

39. Parikh, Y.; Yang, J. H.; Wang, C. Optimizing the mass transport phenomenon around micro-electrodes of an enzymatic biofuel cell inside a blood artery via finite element analysis method. J. Power Sources 2009, 195, 4685-4694.

40. Picioreanu, C.; Head, I. M.; Katuri, K. P.; Loosdrecht, M. C. M. V. Scott, K. A computational model for biofilm-based microbial fuel cells. Water Research 2007, 41, 2921-2940.

41. P. V. Bernhardt, Enzyme Electrochemistry-Biocatalysis on an electrode. Aust. J. Chem. 2006, 59, 233-256.

42. Hamann, C. H.; Hamnett A.; Vielstich, W. Electrochemistry, second ed., Wiley-VCH, New York 1998.

43. Li, H.; Luo, R.; Birgersson E.; Lam K. Y. A chemo-electro-mechanical model for simulation of responsive deformation of glucose-sensitive hydrogels with the effect of enzyme catalysis. J. Mech. Phys. Solids 2009, 57, 369-382.

44. Kouassi, G.; Irudayaraj, J.; McCarty, G. Activity of glucose oxidase functionalized onto magnetic nanoparticles. Biomagn. Res. Technol., 2005, 3, 1-10.

45. Zafar, M., Beden, N.; Leech, D.; Sygmund, C.; Ludwig, R.; Gorton, Lo. Characterization of different FAD-dependent glucosedehydrogenases for possible use in glucose-based biosensors and biofuel cells. Anal Bioanal Chem 2012, 402,2069-2077.

46. Rekuća, A.; Bryjaka, J.; Szymańskab, K.; Jarzębski, A. Laccase immobilization on mesostructured cellular foams affords preparations with ultra high activity. Proc. Biochem. 2009, 44, 191-198.

47. Ahn, M. Y., Zimmerman, A. R.; Martínez, C. E.; Archibald, D. D.; Bollag, J. M.; Dec, J. Characteristics of Trametes villosa laccase adsorbed on aluminum hydroxide. Enzyme Microb. Technol. 2007, 41, 141-148.

48. Spaeth, E. E.; Friedlander, S. K. The Diffusion of Oxygen, Carbon dioxide and inert gas in flowing blood. Biophys. J. 1967, 7, 827-851.

CHAPTER 5

MODELING AND SIMULATION OF ENZYMATIC BIOFUEL CELLS WITH THREE-DIMENSIONAL MICROELECTRODES II: IN BLOOD ARTERY

5.1 Introduction

Since numerous active implantable medical devices (IMDs) such as pacemakers, defibrillators, cochlear implants, neuro-stimulators, artificial hearts, and drug delivery systems have been developed from 1950s [1-6], one of the major challenges in the development of these devices for clinical use is to find a suitable continuous power supply to substitute conventional power sources such as lithium primary or lithium ion secondary batteries which could not last much beyond 2 years at physiological environment in the human body [9-12]. The ideal power source should be capable of generating electricity for prolonged period of time utilizing natural biological fuel abundantly available inside a human body. Therefore, enzymatic biofuel cells (EBFCs) have attracted considerable attention as a promising alternative of the power source for IMDs. EBFCs can take advantage of glucose and oxygen naturally present in the human beings and operate at physiological condition of pH 7, body temperature 37 °C and body pressure 80-120 mmHg [13-14]. More importantly, the enzymes involved in the system such as glucose oxidase and laccase assure biocompatibility of this power source [15].

Until now, EFBCs performance has been significantly improved to reach the operational power requirement range for various types of IMDs such as Pacemaker (30-100 μW), cardiac defibrillator (30-100 μW), neurological stimulator (30 μW-3 mW), drug delivery (100 μW to 2 mV), cochlear implants (5-10 mW), etc [16-17]. However, the results from majority researches are based on *in-vitro* experiments by imitating physiological conditions of human body. Even though it is necessary to conduct the *in-*

vivo experiments to evaluate EBFC performance more accurately, several issues could be obstacles. In fact, as soon as an EBFC chip is placed inside a blood artery, the additional complex problems may arise. The first is within the process of implantation itself which requires a surgery to insert an EBFC chip, electrical wires and other IMD components. The next issue is how to place the chip to avoid the substantial pressure drop which can be dangerous to a human health. The last problem results from the blood flow velocity which is changed from the pressure variation in each cardiac cycle. It is important to study how blood flow affects the stability and cell performance of an EBFC chip inside the artery. Therefore, in order to investigate the EBFCs performance in the human body before *in-vivo* experiments, simulation with finite element analysis approach could be highly useful.

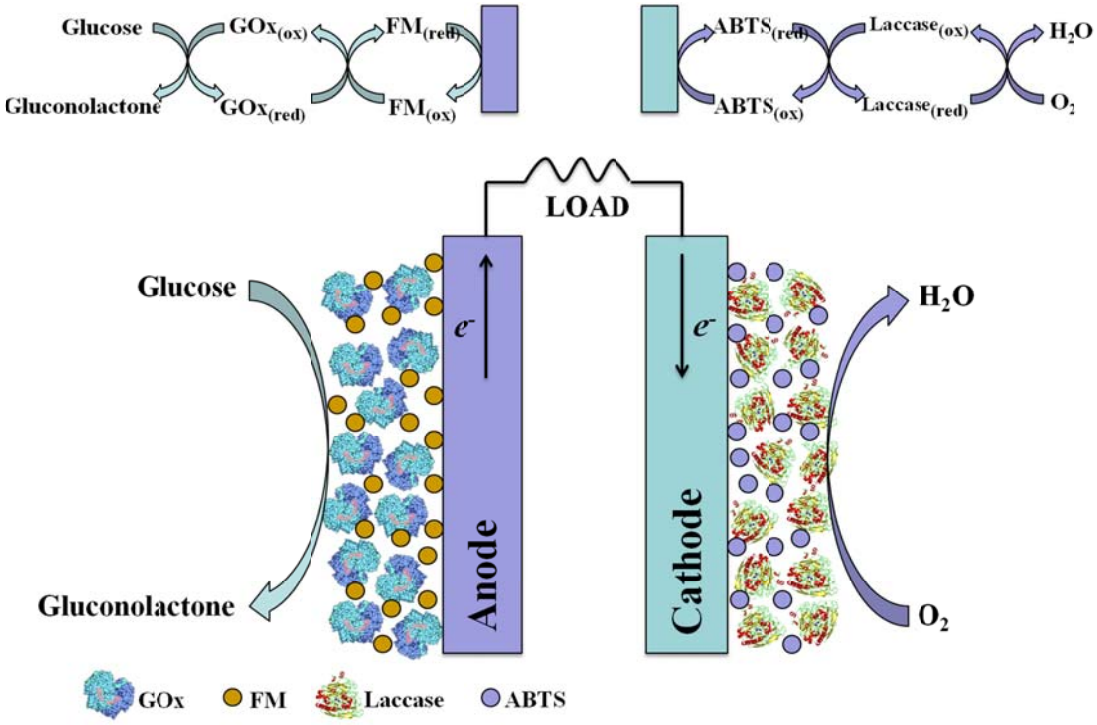

Figure 5.1. Schematic of an EBFC reaction mechanism. Eox and Ered are the oxidized and reduced form of enzymes. Mox and Mred are the oxidized and reduced form of

mediators. E1 and M1 are the enzyme and mediator for anode and E2 and M2 are enzyme and mediator for cathode. Kinetic scheme of mediated bioelectrocatalysis. S and P and substrate and product. ES is enzyme-substrate complex.

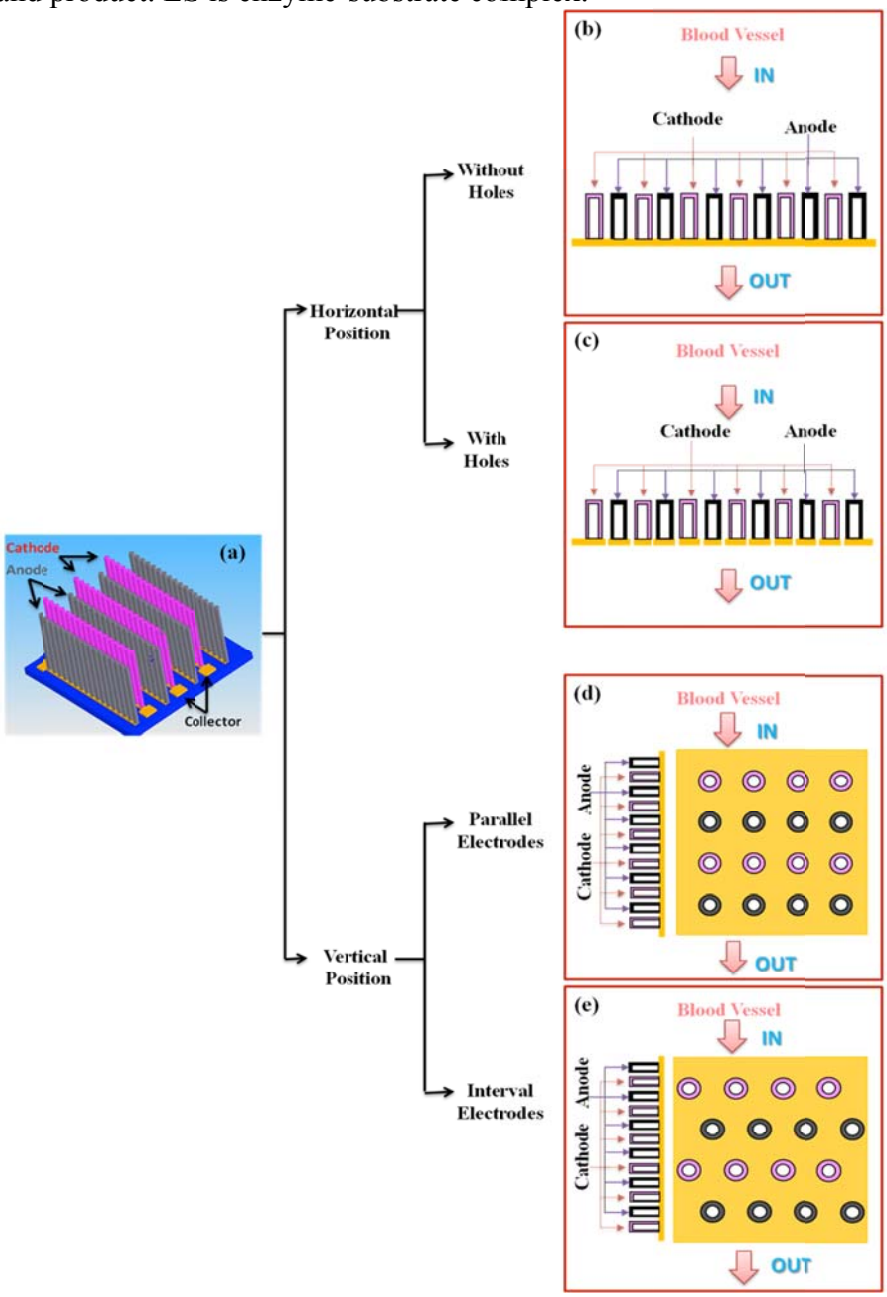

Figure 5.2. Schematic of a proposed design of a chip (a) with holes; (c) without holes in the substrate in horizontal position (HP); (b) Schematic of a prototype EBFC chip; (e) Schematic of a proposed design of a chip in vertical position (VP) including two designs (d) parallel electrodes; (f) interval electrodes.

Our past research has been focus on orientation of a carbon-microelectromechanical systems (C-MEMS) based EBFC chip with 3-D microelectrode arrays inside a blood

artery [18]. The stability of an EBFC chip placing in different orientations in the blood flow has been studied and novel design to minimize the convective flux and optimize the mass transport around microelectrode arrays has been achieved. Based on the previous results, our current research will head towards to EBFCs performance in the blood artery. We apply COMSOL 4.3a Multiphysics software to analyze mass transport, current density and power density for various designs at different orientations in the blood artery of the human body.

5.2 Mechanism of EBFCs

Fig. 4.1 depicts a typical redox reaction kinetic in mediated bioelectrocatalysis of a glucose-oxygen biofuel cell system. The main reason of redox mediation is to increase the rate of electron transfer between the active site of enzyme biocatalysts and an electrode. Depending on the enzyme and reaction conditions, electron transfer rate can be increased by orders of magnitude that of the direct mechanism [19]. The overall reaction occurring within each electrode is shown in Fig. 4.2 [20]. First, the substrate forms an ES complex then maintains at the equilibrium between the enzyme, substrate and ES complex. Next, E_{red} from step one can be reactivated by oxidation with co-substrate M_{ox} to form the M_{red} which subsequently is re-oxidized at the electrode surface in the last step. By introducing an additional redox step, enzyme-mediator electron transfer is isolated from direct electrode potential control. When the substrate concentration is sufficiently larger than the Michaelis constant for the substrate, the kinetics of the redox enzyme reaction, v_E, is given by the modified Michaelis-Menten equation [21]:

$$v_E = \frac{k_{cat}[E]}{1 + K_M/[M_{ox}]} \quad (1)$$

where k_{cat} is the catalytic constant, [E] is the total concentration of the enzyme, K_M is the Michaelis constant of M_{ox} and $[M_{ox}]$ is the concentration of M_{ox}. The complete substrate-enzyme-meditor bioelectrocatalysis system can be simplified by removing substrate where only the oxidized and reduced forms of the mediator determine the total current and potential generated in the system. The electrode potential and concentration relationship can be given by Nernst equation [22]:

$$\mathcal{O} = \mathcal{O}_0 + \frac{RT}{nF} \ln \frac{[M_{ox}]}{[M_{red}]} \quad (2)$$

where $\varnothing_0$ is the standard potential, $[M_{ox}]$ and $[M_{red}]$ represent the concentration of the oxidized and reduced species, R is the universal gas constant, T is the temperature, F is the Faraday's constant and z is the number of electrons transferred in the cell reaction. As for EBFCs, power density (P_{cell}) must be obtained and is defined by:

$$P_{cell} = E_{cell} \times I \quad (3)$$

where E_{cell} is overall cell voltage, I is current density. The overall cell voltage that can be derived from any electrochemical system is given by:

$$E_{cell} = Ec - E_A \quad (4)$$

Ec and E_A are actual potential of cathode and anode, respectively.

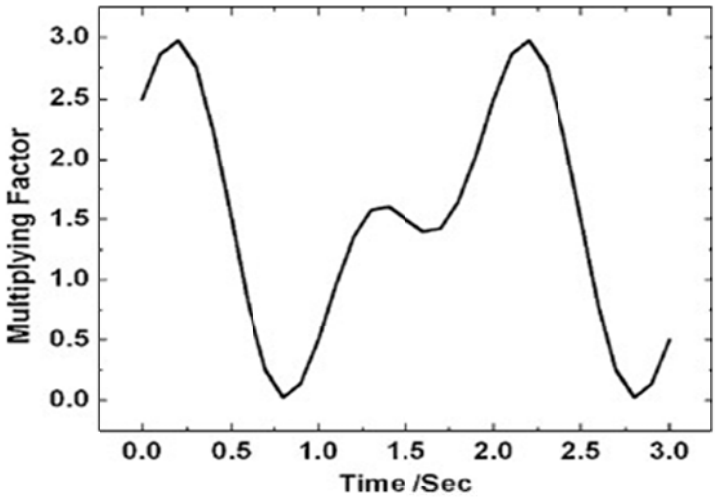

$$f(t) = \begin{cases} \sin \pi t & 0 \le t \le 0.5s \\ 1.5\text{-}0.5\cos[2\ \pi(t\text{-}0.5)] & 0.5s \le t \le 1.5s \end{cases}$$

Figure 5.3. Trigonometry function for pressure variation.

5.3 Simulation modeling

5.3.1 Computational cases

The schematic of a prototype model of an EBFC chip, having highly dense three dimensional micro-electrodes array is shown in Fig 3b. Height of all electrodes is 60 µm, diameter is 10 µm, mediator layer is 5 µm and distance between two electrodes is 30 µm. In this paper, two cases have been considered. In the first case, the comparison has occurred between two designs of EBFC chip in horizontal position (HP): with holes (Fig 3a) and without holes (Fig 3c). In the second case, the comparison has been made between two designs of EBFC chip in vertical position (VP): parallel electrodes (Fig 3d) and interval electrodes (Fig 3f).

5.3.2 Governing equations and boundary conditions

In order to simulate the operational behavior of an EFBC system in the blood artery, three physics have been coupled.

(1) Diffusion and convection application module, which solves Fick's law:

$$\delta_{ts}\frac{\partial c}{\partial t} + \nabla \cdot (-D\nabla c) = R - u \cdot \nabla c \,(\text{non-conservative}) \tag{5}$$

where δts is the time scaling co-efficient; c is the concentration of species (mol m^{-3}); D is the diffusion co-efficient (m^{-2} s); and R is the reaction rate (mol m^{-2} s^{-1}); and u is the velocity field (m s^{-1}).

(2) Incompressible Navier–Stokes application module, which solves Navier–Stokes pressure/velocity and continuity equations:

$$\rho\frac{\partial u}{\partial t} - \nabla \cdot [\eta(\nabla u + (\nabla u)^T)] + \rho(u.\nabla)u + \nabla p = F \tag{6}$$

where η is the dynamic viscosity (Pa s); ρ is the density of a fluid (kg m^{-3}); u is the velocity field (m s^{-1}); p is the pressure (Pa); and F is a volume force field such as gravity.

(3) Conductive DC module, the governing PDE to calculate the potential is given by

$$J = \sigma\phi + J^e \tag{7}$$

where J is the current density, σ is the conductivity of the material, ϕ is the electrode potential solved by equation (2) and J^e is external current density.

The boundary conditions and the relevant constants are shown in Table 4.1 and Table 4.2, respectively.

Boundary	Diffusion	Potential	Pressure
Top boundary of bulk domain	Inward flux	Insulation	Inlet pressure
Bottom boundary of bulk domain	Convective flux	Insulation	Outlet pressure
Bulk-mediator interface	Continuity	Potential expressions	Continuity

mediator-electrode interface	Zero inward flux	Continuity	Wall-no slip
SiO2 layer	Insulation	Insulation	Insulation

Table 5.1. Boundary conditions for simulation models

	Constant	**Value**	**Reference**
R	Universal gas constant	8.314 $J \cdot mol \cdot K^{-1}$	
T	Body Temperature	300 K	
F	Faraday's constant	96485 $C \cdot mol^{-1}$	
D_{gluc}	Diffusion coefficient of glucose	7^{-10} $m^2 \cdot s^{-1}$	[23-25]
D_{oxyg}	Diffusion coefficient of oxygen	2.13-(0.0092Ht)$\cdot 10^{-9}$ $m^2 \cdot s^{-1}$	[26-27]
	Michaelis Menten constant for GOx	1.82 mM	[28]
$K_{M\_}$	Michaelis Menten constant for laccase	3.28 mM	[29]
k_{cat}	Catalytic rate constant of GOx	6.5 S^{-1}	[30]
k_{cat_l}	Catalytic rate constant of laccase	2.69 S^{-1}	[31]
	Concentration of M_{ox}	5 mM	Initial value
E^o_A	Reference potential for anode	-0.32 V	[31]
E^o_C	Reference potential for cathode	0.585 V	[31]
σ_{carb}	Conductivity of glassy carbon	8000 $S \cdot m^{-1}$	[32, 33]
σ_{gluco}	Conductivity of glucose	10000 $S \cdot m^{-1}$	[34, 35]
	Density of blood	1060 kg m^{-3}	[36]

Viscosity of blood	0.005 Pa s	[37]

Table 5.2. Constants and parameters for simulation modeling

The pressure variation in each cardiac cycle is considered with a simple trigonometry function (fluid structure interaction in a network of blood vessels model, COMSOL Multiphysics), plotted in Fig. 4, to maintain normal systolic/diastolic pressure variation of 120/80 mmHg in the artery [38-39].

5.4 Results and discussions

5.4.1 Glucose concentration profile for HP orientation

Mass transport between microelectrodes has been investigated based on glucose concentration variation around electrodes in HP orientation. The glucose amount flowing in the artery changes at the inlet according to contraction and extraction of blood artery. To show the effect of varying amount of glucose, the EBFC is multiplied with glucose concentration at the artery inlet to consider continuously varying glucose flux in time shown in Fig 5(a) and 5(b) which are the point glucose concentration from the bottom of well between microelectrodes. The glucose concentration from the EBFC chip experiences a cyclic variation based on a trigonometry function. Ideally, glucose should interact with the total surface area of electrodes from top to bottom to fully utilize the biocatalysts immobilized onto them. However, the glucose reacts immediately with the top portion of the electrode where it diffuses first and the rest of glucose reacts gradually down to the bottom of the electrode. In comparison between an EBFC chip with holes and without holes, the lowest and highest concentration for chip with holes are 65 mmol/L and 238 mmol/L while for without holes are 22 mmol/L and 162 mmol/L. It is inferred that glucose diffusion has been significantly improved in the chip with holes

because the inward flux can diffuse through the chip. In order to investigate the glucose concentration variation over time on total electrode surface, the integration of the concentration along the electrode surface at different time point, which quantitively represents the total surface glucose concentration on the electrode surface, has been calculated. The total surface concentration results prove that the mass transport around microelectrode is enhanced with holes on the EBFC chip which is significantly important for an EBFC performance. This preferred design can also effectively prevent blood clotting. Human blood is mainly consisted of red blood cells and white blood cells with the size range from 6-15 μm which are mostly smaller than the size of the holes in the chip [40]. Therefore, these cells can pass through the holes in between micro-electrodes without blocking the way in between micro-electrodes.

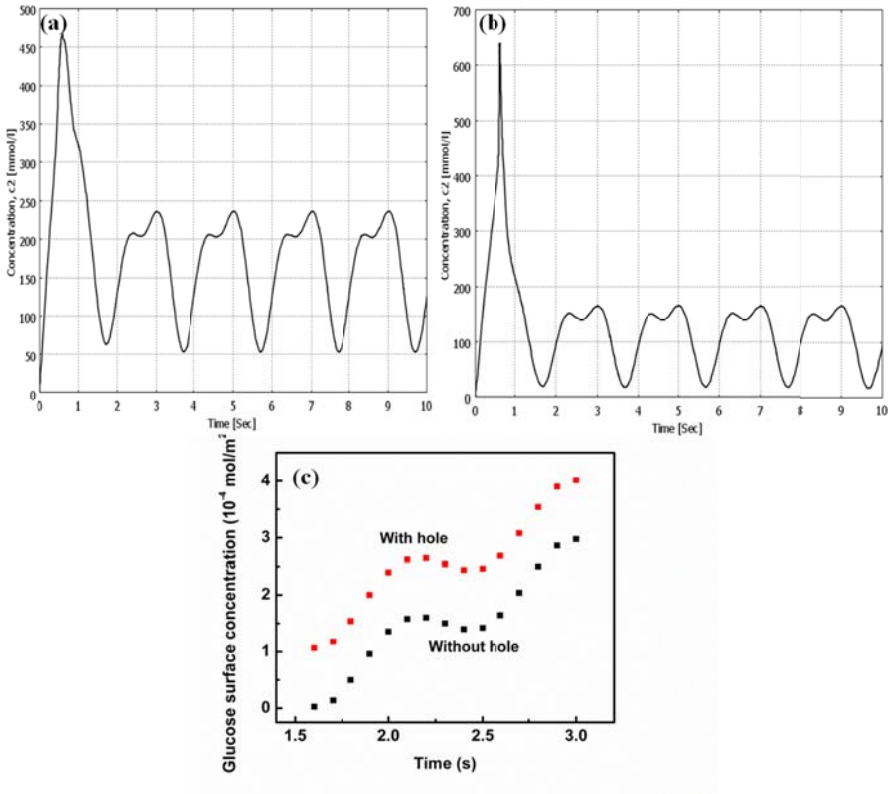

Figure 4.4. Glucose concentration profile over time for (a) EBFC chip with hole and (b) without hole. (c) Comparison of total glucose surface concentration in one cyclic pressure change between two designs.

5.4.2 Current density profile for HP orientation

In contrast to a 2-D battery, in which a uniform current density is naturally obtained over the surfaces of the cathode and anode, the current density in a 3-D EBFC is inherently non-uniform. The substrate will react with the biocatalysts immobilized on the top of the electrodes first and at the meantime diffuse and react along the electrode surface from top to bottom. The competition between higher redox reaction rate and lower diffusion rate causes non-uniform electron transfer throughout the electrode surface and consequently generates non-uniform current density from top to bottom of the electrode. Fig. 6 represent the current distribution along the surface from leftmost to rightmost electrode for EBFC chip without holes (Fig. 6a) and with holes (Fig. 6b). Because of cyclic pressure variation, the current density distribution varies over time as well. At time of 2s, 4s, 6s, 8s, 10s, etc., the current density is at the lowest while it reaches highest at time of 3s, 5s, 7s, 9s, etc. The current density is not uniform from the central to outer electrodes. The electrodes located at the circumference of a chip are having higher current density compared to those located in the center of the chip. The variation of the current density distribution around the single electrode is much higher in the chip without holes than that of chip with holes. In order to quantitively compare the uniformity of current density of two designs over the time, the integration of the total surface current density along the electrode surface at different time point has been studied in Table 5.3.

Time (s)	**Total surface current density (10^{-2}**	**Total surface current density (10^{-2}**

	A/m) without holes	A/m) with holes
1	2.31	2.54
2,4,6,8,10	2.26	2.64
3,5,7,9	2.53	2.69

Table 5.3 current density comparison between EBFC chip without and with holes.

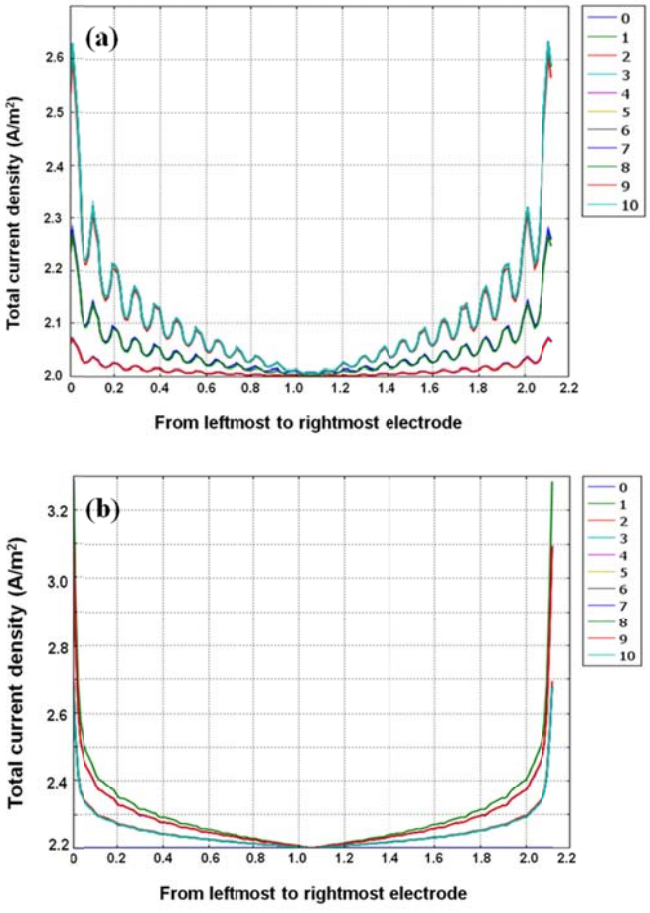

Figure 5.5. Total current density profile for (a) EBFC chip without hole; (b) EBFC chip with hole.

In the case of the chip without holes, the total surface current density changes 12% in one cyclic pressure variation while it only changes 2% in the case of the chip with holes. In

general, non-uniform currents result in poor utilization of the electrode materials, and are thus associated with lower cell efficiencies, reduced electrode stability due to non-uniform stresses, and non-uniform heat dissipation. Therefore, the EBFC chip with holes is highly preferred in practical applications.

5.4.3 Power density profile for HP orientation

One of the most important characteristics to examine in an EBFC is power density. In this work, simulation was conducted by incorporating the Nernst equation. Various external loads at the range of 5-500 kΩ are considered in the simulation in order to understand the power density-voltage relationship. As shown in Fig. 7, the power density for both designs of EBFC chip increases as the voltage gets higher and reaches a maximum. After reaching the maximum, increasing the voltage leads to a decrease in the power density. The EBFC chip with holes is observed to have the higher power density at around 160 μW/cm^2 when the voltage is approximately 0.55 V than that of chip without holes. This performance of EBFC is adequate for operation of low-voltage CMOS integrated circuits.

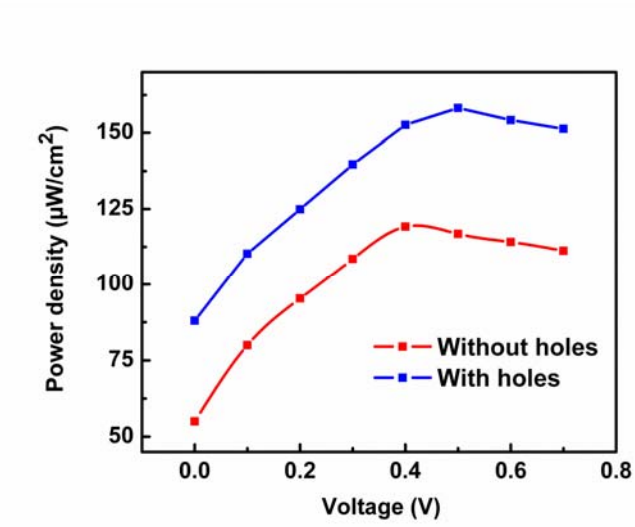

Figure 5.6. Power density vs. cell voltage for two designs in HP orientation.

5.4.4 Current density profile for VP orientation

In similar to HP orientation, the interdigitated microelectrode arrays suffer from a non-uniform current density distribution. Fig. 8(a) and 8(b) are two designs in VP orientation and Fig 8(c) and 8(d) illustrate the sensitivity of the current density distribution to electrode placement for different interdigitated microelectrode arrays. To allow comparison of the current densities between cathode and anode, current density is plotted in the same arbitrary units in each case. In the parallel low design, cathode and anode are in the alternating rows which results in high current density between each adjacent cathode and anode pair at angle 0°. As angle increases to 90°, almost 70% decrease in current density is observed. In order to minimize the current density decrease between each neighboring cathode and anode pair, an interdigitated microelectrode arrays in which each anode is surrounded by four cathodes. In this geometry, the higher number of nearest neighbor electrodes of opposite polarity allows a significantly better uniformity in current density distribution at each electrode. The current density only varies by 10% along the electrode circumference.

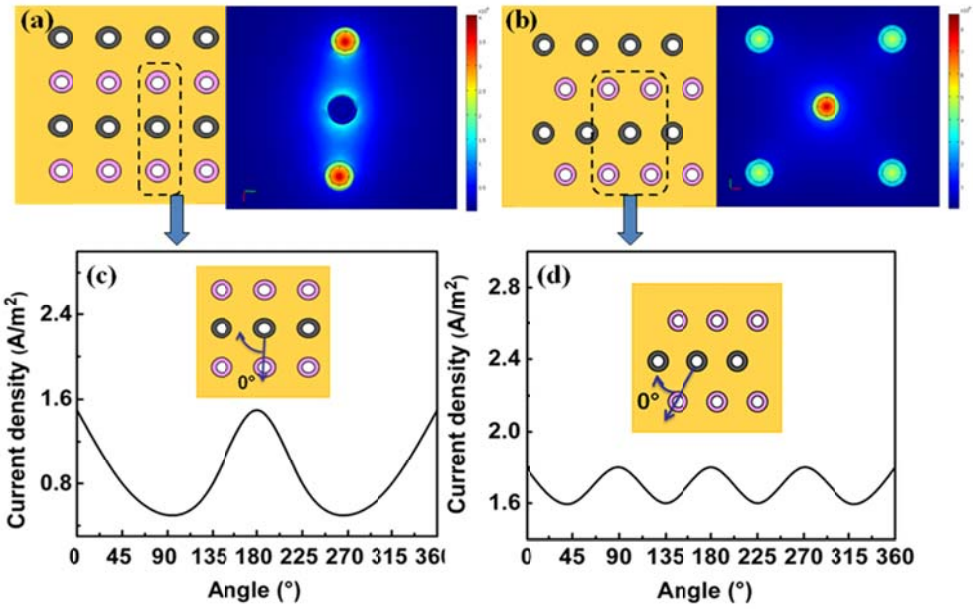

Figure 5.7. Current density subdomain profile for (a) parallel electrodes; (b) interval electrodes; Current density distribution profile in the same arbitrary units for (c) parallel electrodes; (d) interval electrodes.

5.4.5 Power density profile for VP orientation

Similarly, power density has been evaluated between two interdigitated microelectrode arrays in Fig. 9. In consistence with results from current density, the interval electrode design has better power density of 155 $\mu W/cm^2$ at 0.58V in potential. Therefore, the interval electrode design in VP orientation is recommended.

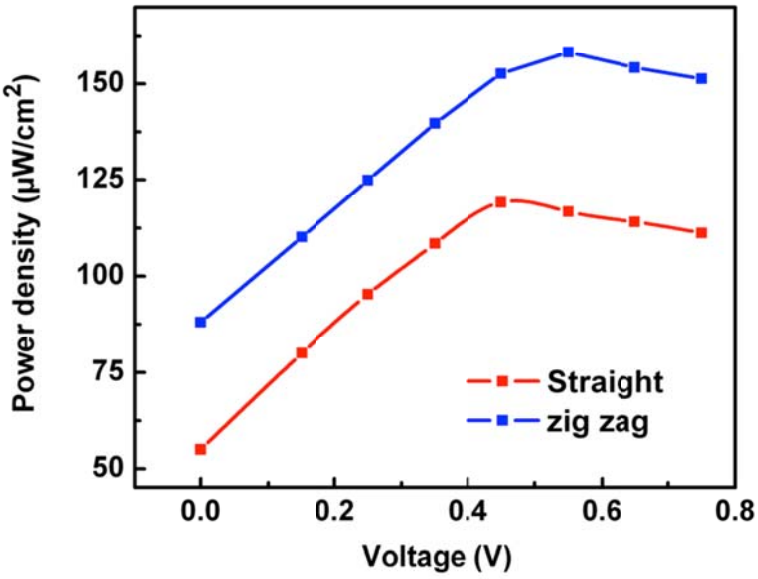

Figure 5.8. Power density vs. cell voltage for two designs in VP orientation.

5.2 Conclusion

While significant increases in both current and power density are obtainable from 3-D EBFC system, the inherent difficulty in achieving a uniform current distribution may limit the practical applications. In this paper, a detailed simulation to investigate the performance of 3-D microelectrode EBFC arrays in blood artery is studied. The several examples presented above demonstrate that there are tremendous opportunities to

improve 3-D microelectrode EBFC arrays design. From the simulation, more favorable design is obtained for HP and VP orientation, respectively. The power density for 3-D microelectrode EBFC arrays in blood artery reaches 160 $\mu W/cm^2$ at 0.55 V in voltage in HP while 155 $\mu W/cm^2$ at 0.58 V in voltage in VP. However, the biomechanical process and hemodynamic process are more complex when it comes to practical application, especially on the micro-scale level. More detailed research needs to be studied with biologists in order to reach the applicable level of the EBFCs as the functional power source for IMDs.

5.5 Reference

1. D. Ivnitski, B. Branch, P. Atanassov and C. Apblett, Glucose oxidase anode for biofuel cell based on direct electron transfer, Electrochem. Commun., 2006, 8, 1204-1210.

2. E. Katz, A.N. Shipway and I. Willner, Biochemical fuel cells. In: Handbook of Fuel Cells—Fundamentals, Technology and Applications, W. Vielstich, H.A. Gasteiger and A. Lamm, Fundamentals and Survey of Systems vol. 1, John Wiley & Sons, Ltd., Hoboken, NJ, 2003, 355–381.

3. A. Heller, Miniature biofuel cells. Phys. Chem. Chem. Phys., 2004, 6, 209–216.

4. A. Ramanavicius, A. Kausaite and A. Ramanaviciene, Biofuel cell based on direct bioelectrocatalysis, Biosens. Bioelectron., 2005, 20, 1962-1967.

5. L. Halamkova, J. Halamek, V. Bocharova, A. Szczupak, L. Alfonta and E. Katz, Implantable biofuel cell operating in a living snail. J. Am. Chem. Soc., 2012, 134, 5040-5043.

6. V. Coman, R. Ludwig, W. Harreither, D. Haltrich, L. Gorton, T. Ruzgas and S. Shleev, A Direct Electron Transfer-Based Glucose/Oxygen Biofuel Cell Operating in Human Serum, Fuel Cells, 2010, 10, 9−16.

7. C. Pan, Y. Fang, H. Wu, M. Ahmad, Z. Luo, Q. Li, J. Xie, X. Yan, L. Wu, Z. L. Wang and J. Zhu, Generating electricity from biofluid with a nanowire-based biofuel cell for self-powered nanodevices, Adv. Mater., 2010, 22, 5388− 5392.

8. B. R. Ringeisen, E. Henderson, P. Wu, J. Pietron, R, Ray, B. Little, J. Biffinger and J. Jones-meehan, High power density from a miniature microbial fuel cell using shewanella oneidensis DSP10, Environ. Sci. Technol., 2006, 40 (8), 2629–2634.

9. B. Dunn, J.W. Long and D. Rolison, Rethinking multifunction in three dimensions for miniaturizing electrical energy storage, Interface, 2008, 17, 49-53.

10. V. Anandan, X. Yang, E. Kim, Y. Rao and G. Zhang, Role of reaction kinetics and mass transport in glucose sensing with nanopillar array electrodes, J. Biol. Eng., 2007, 1, 1-10

11. N. Godino, X. Borrise, F. X. Munoz, F. J. Campo and R. Compton, Mass transport to nanoelectrode arrays and limitations of diffusion domain approach: Theory and experiment, J. Phys. Chem., 2009, 113, 11119-11125.

12. B. Y. Park, L. Taherabadi, C. Wang, J. Zoval and M. Madou, Morphological and electrical properties of carbon films of various thinknesses carbonized from photoresist and the implications for C-MEMS devices in conductive media, Journal of the electrochemical society, 2005, 152(12), J136-J143.

13. K. Malladi, C. Wang and M. Madou, Microfabrication of suspended C-MEMS structures by EB writer and pyrolysis, Carbon, 2006, 44(13), 2602-2607.

14. B. Y. Park, R. Zaouk, C. Wang and M. Madou, Fractal C-MEMS architectures for 3D miniature power and sensor applications, ECS Trans, 2006, 1(20), 1-11.

15. B. Y. Park, R. Zaouk, C. Wang, J. Zoval and M. Madou, Fractal C-MEMS electrodes: theory and preliminary fabrication, ECS Trans, 2007, 4(1), 83-92.

16. C. Wang, R. Zaouk, B. Y. Park and M. Madou, Carbon as a MEMS material: Micro and nano fabrication of pyrolyzed photoresist carbon, International journal of manufacturing technology and management, 2008, 13, 360-375.

17. H. Min, B. Y. Park, L. Taherabadi, C. Wang, Y. Yeh, R. Zaouk, M. Madou and B. Dunn, Fabrication and properties of a carbon/polypyrrole three-dimensional microbattery, Journal of power sources, 2008, 178(2), 795-800.

18. Y. Parikh, J. H. Yang and C. Wang, Optimizing the mass transport phenomenon around micro-electrodes of an enzymatic biofuel cell inside a blood artery via finite element analysis method, J. Power Sources, 2009, 195, 4685-4694.

19. A. L. Ghindilis, P. Atanasov and E. Wilkins, Enzyme-catalyzed direct electron transfer: Fundamentals and analytical applications, Electroanalysis, 1997, 9, 661-674.

20. F. A. Armstrong, H. A. O. Hill and N. Walton, Direct electrochemistry of redox proteins, J. Acc. Chem. Res. 1988, 21, 407-413.

21. P. De Taxis Du Poet, S. Miyamoto, T. Murakami, J. Kimura, I. Karube, Direct electron transfer with glucose oxidase immobilized in an electropolymerized poly(N-methylpyrrole) film on a gold microelectrode, Anal. Chim. Acta, 1990, 235, 255-263.

22. C. G. J. Koopal, B. de Ruiter and R. J. M. J. Nolte, Amperometric biosensor based on direct communication between glucose oxidase and a conducting polymer inside the pores of a filtration membrane, Chem. Soc., Chem. Commun, 1991, 1691-1962.

23. Q. Chi, J. Zhang, S. Dong and E. Wang, Direct electrochemistry and surface characterization of glucose oxidase adsorbed on anodized carbon electrodes, Electrochim. Acta, 1994, 39, 2431-2438.

24. L. Jiang, C. J. Mcneil and J. M. Cooper, Direct electron transfer reactions of glucose oxidase immobilised at a self-assembled monolayer, J. Chem. Soc., Chem. Commun, 1995, 1293-1295.

25. A. Lei and R. H. Baughman, Direct electron transfer of glucose oxidase on carbon nanotubes, Nanotechnology, 2002, 13, 559-562.

26. C. Cai, Direct electron transfer of glucose oxidase promoted by carbon nanotubes, J. Anal. Biochem, 2004, 332, 75-83.

27. J. Liu, A. Chou, W. Rahmat, M. N. Paddon-Row and J. Gooding, Achieving Direct Electrical Connection to Glucose Oxidase Using Aligned Single Walled Carbon Nanotube Arrays, J. Electroanalysis, 2005, 17, 38-46.

28. Y. Liu, M. Wang, F. Zhao, Z. Xu and S. Dong, The direct electron transfer of glucose oxidase and glucose biosensor based on carbon nanotubes/chitosan matrix, Biosens. Bioelectron, 2005, 21, 984-988.

29. D. Ivnitski, B. Branch, P. Atanassov and C. Apblett, Glucose oxidase anode for biofuel cell based on direct electron transfer, Electrochem. Commun, 2006, 8, 1204-1210.

30. C. Picioreanu, I. M. Head, K. P. Katuri, M. C. M. V. Loosdrecht and K. Scott, A computational model for biofilm-based microbial fuel cells, Water Research, 2007, 41, 2921-2940.

31. P. V. Bernhardt, Enzyme Electrochemistry-Biocatalysis on an electrode, Aust. J. Chem. 2006, 59, 233-256

32. C. H. Hamann, A. Hamnett, W. Vielstich, Electrochemistry, second ed., Wiley-VCH, New York, 1998.

33. H. Li, R. Luo, E. Birgersson and K. Y. Lam , A chemo-electro-mechanical model for simulation of responsive deformation of glucose-sensitive hydrogels with the effect of enzyme catalysis , J. Mech. Phys. Solids 2009, 57, 369–382.

34. G. Kouassi, J. Irudayaraj and G. McCarty, Activity of glucose oxidase functionalized onto magnetic nanoparticles, BioMagnetic Research and Technology, 2005, 3, 1-10.

35. F. Wang, C, Guo, L, Yang and C, Liu, Magnetic mesoporous silica nanoparticles: Fabrication and their laccase immobilization performance, Bioresource Tech, 2010, 101, 8931-8935.

36. M. Y. Ahn, A. R. Zimmerman, C. E. Martínez, D. D. Archibald, J. M. Bollag and J. Dec, Enzyme and Microbial Technology, 2007, 41, 141-148.

37. E. E. Spaeth and S. K. Friedlander, The Diffusion of Oxygen, Carbon dioxide and inert gas in flowing blood, Biophysical Journal, 1967, 7, 827-851.

38. N. Matsuda and K. Sakai, Blood flow and oxygen transfer rate of an outside blood flow membrane oxygenator, Journal of membrane Science, 2000, 170, 153-158.

39. F. Barriere, Y. Ferry, D. Rochefort and D. Leech, Targetting redox polymer as mediators for laccase oxygen reduction in a membrane-less biofuel cell, Electrochemistry Communications, 2004, 6, 237-241.

40. F. Hirsch, E. Texter, L. Wood, W. Ballard, F. Horan, I. Wright, C. Frey and D. Starr, The Electrical Conductivity of Blood, J. American Society of Hematology, 1950, 5, 1017-1035.

CHAPTER 6

GRAPHENE/ENZYME ENCRUSTED THREE-DIMENSIONAL CARBON MICROPILLAR ARRAYS FOR MEDIATORLESS MICRO-BIOFUEL CELLS

6.1 Introduction

Nowadays the undergoing miniaturization of implantable medical devices (IMDs), such as pacemaker, drug delivering pumps, neuro-stimulators, cochlear implants etc., requires the development of unconventional power source systems [1]. These devices should be capable of continuously operation for prolonged periods of time without external refueling or recharging while generating sufficient power output in a miniaturized size [2, 3]. Among all the prospective alternatives as the future power source systems for IMDs, glucose based enzymatic biofuel cell (EBFC), where the electric power is converted from the redox reactions, show significant promise as theoretically they are able to operate indefinitely, given the abundance of glucose and oxygen in human body [4]. The EBFC consists of two bioelectrodes immobilized with two types of enzymes, respectively, which catalyze the oxidation of glucose at the anode and reduction of oxygen at the cathode [5]. Ever since the invention of the first biofuel cell by Yahiro et al [6], advancements have been achieved by using high surface area materials to increase the enzyme loading, chemical covalent immobilization to stabilize the enzyme and redox mediators to facilitate the electron transfer since the active site of enzyme is buried deep under the protein shell [7]. However, the immobilization of mediators usually involves complex procedures and leads to a drop in the theoretical open-circuit potential [7]. Besides, the leakage of mediators from the electrodes may result in toxicity considering that the EBFC is implantable in the human body [7]. To date, the main challenges in developing EBFCs are how to increase the power output and cell lifetime [8]. The search

for proficient immobilization techniques and novel electrode architectures to enable direct electron transfer (DET) has been targeted [7, 8].

The recent developments in nanotechnology have opened up new opportunities in enzyme immobilization at nanostructured interfaces for efficient electrocatalysis to diminish the usage of mediators in EBFC and still realize DET [9]. Nanomaterials such as carbon nanotubes, carbon nanoparticles, hollow carbon spheres, graphene, and mesoporous carbons have been used as conductive agents, which allow further increasing the surface area of the electrode without changing the geometric dimensions [10-16]. Graphene, a two-dimensional sheet of carbon atoms, with its excellent conductivity, high surface area and good mechanical stability, has attracted an enormous amount of attention [17]. On one hand, in the application of conventional fuel cells, graphene that acted as good anchoring sites for deposition of catalyst has led to the improvement of Pt catalyst performance and stability [18-20]. On the other hand, graphene has also shown to be particularly appropriate to establish electronic communication with biocatalyst such as redox enzyme in the bio-electrochemical application, since it can reach close proximity to the redox active sites to promote DET [21]. It can be integrated quite effectively with biocatalysts to fabricate networked electrode interfaces, where high loading of biocatalysts can lead to improved power output for EBFC [22]. Since 2010, several works on graphene based EBFC have been published [23-28]. Most of them used planer glassy carbon or metal thin film electrodes as current collectors, some of which can support certain low energy-consumable IMDs [25-28]. Previous studies on batteries with 3D microelectrodes have shown a 350% larger energy capacity as compared to traditional two-dimensional designs in the same areal footprint [29]. The ion transport distance for the 3D microelectrode based batteries during discharge is 3.5 times shorter than that in

the thin film batteries [30]. Our group has focussed on developing various 3D micro/nanostructures using carbon microelectromechanical systems (C-MEMS) technique [31-40]. C-MEMS involves the pyrolysis of patterned photoresist to build a carbon platform; The high aspect ratio and short transport length of the 3D micro/nanostructures exhibited excellent performance for a wide variety of electrochemical applications such as lithium-ion batteries, biosensors, supercapacitors [41-49]. To the best of our knowledge, there are no publications on graphene based 3D C-MEMS microstructures as electrode materials for EFBC. It will be interesting to further improve the performance of EBFC with the integration of graphene onto the 3D microstructures to take advantage of potential merits including increased surface areas and enhanced chemical functionality. Therefore, developing such an enzyme/graphene 3D network for EBFC where the enzyme can be trapped to reach close enough to the electroactive surface while allowing DET process is highly crucial.

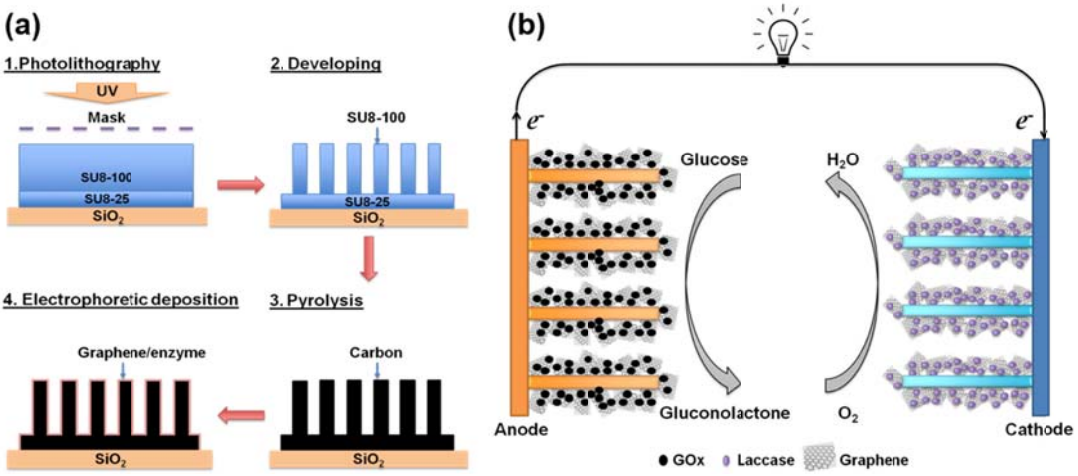

Figure 5.1. (a) Schematic showing the fabrication of EBFC based on C-MEMS micropillar arrays. (b) Illustration of the EBFC with graphene/enzyme encrusted 3D carbon micropillar arrays (not to scale).

In this paper, a mediatorless enzymatic micro-biofuel cell based on graphene/enzyme encrusted 3D micropillar arrays is developed and presented. The fabrication process of

this system combines top-down C-MEMS technology to fabricate the 3D micropillar arrays platform and bottom-up electrophoretic deposition (EPD) to deposit graphene/glucose oxidase (GOx) and graphene/laccase composites onto the 3D micropillar arrays based anode and cathode, respectively. EPD is a versatile method that has been successfully applied for the deposition of carbon nanotubes, graphite oxide, graphene as well as enzymes for electrochemical applications [50-52]. Particularly, the EPD method has a number of advantages such as high deposition rate, good thickness controllability, good uniformity and simple operation [53]. In this study, the co-deposition of enzyme with graphene to form an enzyme/graphene network has been first investigated. For comparison, the bare C-MEMS based 3D micropillar arrays have been functionalized by Diazonium salt electrochemical reduction method [54-57], and then immobilized with glucose oxidase and laccase on anode and cathode, respectively. By comparing the EBFC performance of graphene/enzyme encrusted 3D micropillar arrays to bare 3D micropillar arrays, the graphene based EBFC generated a maximum power density of 136.3 μWcm^{-2} at 0.59 V, which is almost 7 times that of the maximum power density from bare carbon based EBFC.

6.2 Experimental section

6.2.1 Fabrication of 3D C-MEMS micropillar arrays

The experimental setup and details of the C-MEMS process used in this work has been reported previously [31-38]. Illustration of the typical C-MEMS fabrication procedure is shown in Fig. 1. In brief, the C-MEMS based 3D micropillar arrays were prepared by a two-step photolithography process followed by a pyrolysis step. In the first photolithography step, a two-dimensional circle (diameter of 8 mm) pattern as current

collector was firstly created using NANO^{TM} SU-8 25. The photoresist film was spin-coated onto a silicon oxide wafer (4" in diameter, (1 0 0)-oriented, n-type) at 500 rpm for 12 sec and 3000 rpm for 30 sec by using a Headway research^{TM} photoresist spinner, followed by soft bake at 65 °C for 3 min and hard bake at 95 °C for 7 min on a hotplate. The baked photoresist was patterned with a UV exposure dose of 300 mJ cm^{-2}. Post-exposure bake was conducted at 65 °C for 1 min and 95 °C for 5 min on a hotplate. Next, second photolithography process was employed using NANO^{TM} SU-8 100 photoresist to build cylindrical micropillar arrays on patterned circle. SU-8 100 was spin-coated at 500 rpm for 12 sec and 1500 rpm for 30 sec by using a Headway research^{TM} photoresist spinner. The spincoated photoresist was then soft baked at 65 °C for 10 min and hard baked at 95 °C for 45 min in an oven. The exposure was done using a UV exposure dose of 700 mJ cm^{-2}. Post-exposure bake was performed at 65 °C for 3 min and 95 °C for 10 min in an oven. Then the sample was developed by NANO^{TM} SU-8 developer (Microchem, USA) for 5-10 min to wash away the remaining unexposed photoresist followed by isopropanol rinsing and nitrogen drying. Finally, the resulting SU-8 structures were pyrolyzed at 1000 °C for 1 h in a Lindberg alumina-tube furnace with a continuous flow at 500 sccm forming gas (95% nitrogen, 5% hydrogen) then naturally cooled down to room temperature.

6.2.2 Construction of bare 3D micropillar arrays based EBFC

Step 1-functionalization: The modification of glassy carbon was conducted by the reduction of the diazonium salt. The 40 mM 4-(4'-nitrophenylazo) benzene diazonium tetrafluoroborate (Aldrich) dissolved in 1% sodium dodecyl sulfate (Aldrich) aqueous solution was prepared according to previously established procedures [55]. The

developed C-MEMS samples were placed in the newly prepared aqueous solutions for 4 h under shaking. Electrochemical reductions were performed in a 0.1 M KCl (Aldrich) solution by cycling scan five times between 0 to -1.5 V versus Ag/AgCl at 50 mV/s using a multichannel potentiostat/galvanostat (VMP3, Princeton Applied Research). Step 2-immoblization: the GOx (Aldrich) and laccase (Aldrich) (1.5mg/mL) were prepared in 0.1 M N-hydroxysuccinimide (NHS, Aldrich) and 0.4 M 1-ethyl-3-(3-dimethylaminopropyl) carbodiimide (EDC, Aldrich) to activate the carboxyl group. The immobilizations were conducted by placing the samples in the prepared enzyme solutions for 2 h at 37 °C in a humidified chamber. Cyclic voltammograms were measured by VMP3 to confirm the functionalization and immobilization. FTIR (JASCO FT/IR 4100 spectrometer) was also used to analyse the functionalization of glassy carbon surface. The resulting bioanodes and biocathodes were connected with an external circuit for EBFC performance testing using a CHI 660C workstation. EBFC performance was tested in 100 mM air saturated glucose in PBS (pH=7.4)

6.2.3 Construction of graphene integrated 3D micropillar arrays based EBFC

EPD has been performed to integrate graphene and enzyme composite onto the 3D micropillar arrays surface. Graphene (1.5 mg/mL) and GOx (1.5 mg/mL) were first dispersed in water and then the resultant solution was sonicated for 1 h in order to fabricate the bioanode. Similar preparation was used for graphene and laccase dispersion for fabrication of the biocathode. Graphene/enzyme composites were then deposited by EPD with an applied DC voltage 10 V at a distance of 2 cm for 3 min. After the deposition, samples were dried at room temperature then kept at 4 °C to protect the enzyme from denaturisation before using. The morphology of the graphene/cabon

microstructures was investigated using JOEL 6335 FE-scanning electon microscopy (SEM). FTIR (JASCO FT/IR 4100 spectrometer) testing was conducted to confirm the enzymes existence. The electrochemical performance of the bioelectrodes was tested by cyclic voltammograms using VMP3. To evaluate the performance of the EBFC, the bioanodes and biocathodes were externally connected through a variable resistor (100 Ω - 100 kΩ), and the voltage and current between the bioelectrodes for each load were measured by CHI 660C workstation. EBFC performance was tested in 100 mM air saturated glucose in PBS (pH=7.4).

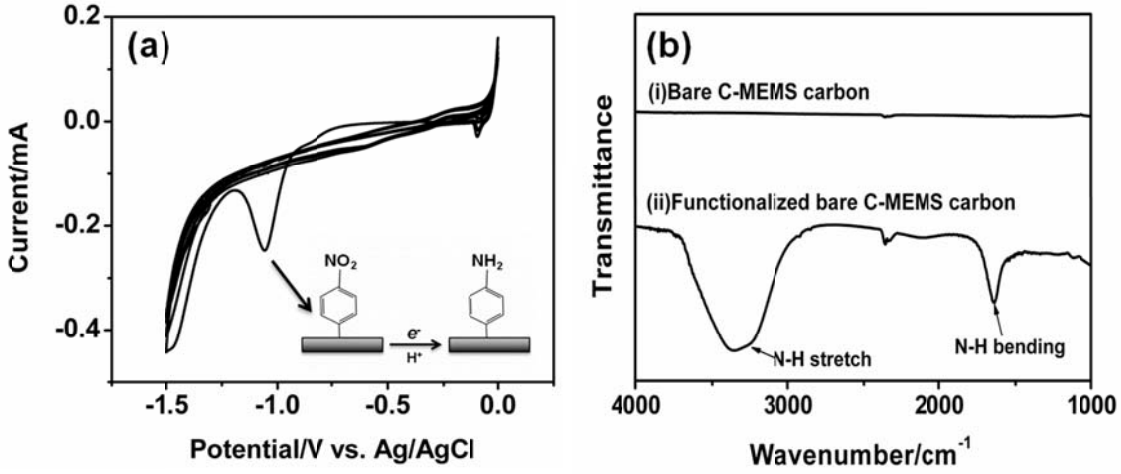

Figure 6.2. (a) Cyclic voltammograms of electrochemical reduction of bare 3D C-MEMS electrode, (b) FTIR spectra of bare 3D C-MEMS electrode (i) before and (ii) after functionalization.

6.3 Results and discussion

6.3.1 Characterization of bare 3D carbon micropillar arrays

In order to immobilize GOx and laccase covalently on the surface of anode and cathode, respectively, the fabricated 3D carbon micropillar arrays were grafted with functional amino groups (-NH_2) to form covalent binding with carboxyl groups (-COOH) in GOx

and laccase. The 4-(4'-nitrophenylazo) benzene diazonium tetrafluoroborate-a diazonium ion derivative is a highly reactive phenyl radical that can bind to glassy carbon surface irreversibly. After placing in diazonium salt aqueous solutions for 4 h, the 3D carbon micropillar arrays samples were conducted electrochemical reduction of nitro groups ($-NO_2$) to amino group ($-NH_2$). Fig. 2(a) shows five repeated cyclic voltammograms of the nitro groups terminated glassy carbon surface in an aqueous 0.1 M KCl solution with a scan rate of 50 mVs^{-1}. As the potential was brought negative, the nitro groups were reduced to amino groups at a potential of ~1.0 to -1.1 V, resulting in the first reduction peak in first reduction sweep of the cyclic voltammogram. As the potential went more negative, the reduction peak at -1.5 V was attributed to the hydrogen evolution peak of water. This is consistent with the results of previous research conducted on glassy carbon [55]. As the potential was brought positive, there was no corresponding oxidation peak to be observed, which indicated that the electrochemical reduction was irreversible and the amino groups cannot be easily re-oxidized. The consecutive four cyclic voltammograms were featureless with no characteristic reduction or oxidation peaks. It was demonstrated that the all the electro-active nitro groups were electrochemically reduced to amino groups during the first negative sweep of the potential. Fig. 2(b) presents the FTIR spectra of 3D carbon micropillar arrays (i) before the functionalization and (ii) after the functionalization. From (ii), the broad transmission peak centering at around 3300 cm^{-1} in the spectrum is assigned as amine N-H stretching vibration [58]. The presence of amine N-H bending vibration was signalled by the peak at around 1600 cm^{-1} and C-N stretching vibration was also observed by the peak at around 2340 cm^{-1} [59]. None of those characteristic peaks were observed in 3D carbon micropillar arrays before the functionalization. From both cyclic voltammogram and FTIR results, it can be concluded

that the C-MEMS fabricated 3D micropillar arrays were successfully functionalized with amino groups. The electrochemical reduction of nitro groups to amino groups is the key process for successful covalent binding of GOx and laccase. Successful immobilization was confirmed by the electrochemical test in following section.

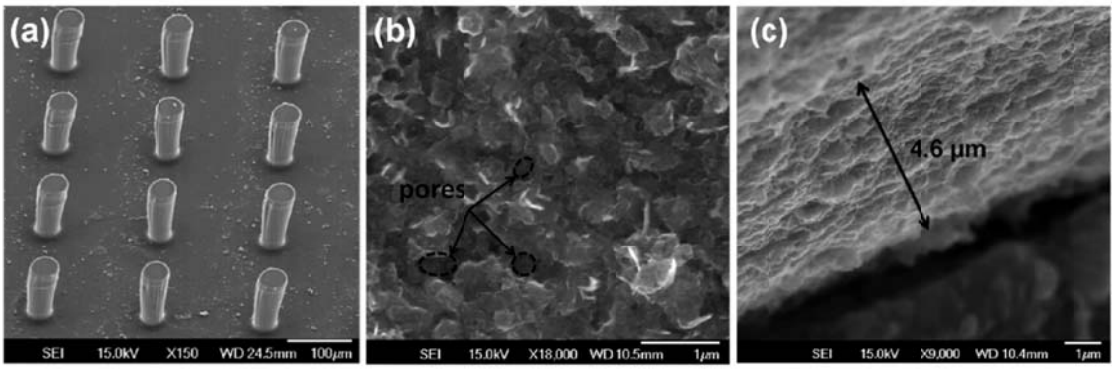

Figure 6.3. SEM images showing the morphology of (a) graphene/GOx encrusted 3D carbon micropillar arrays, (b) top view of deposited graphene/GOx on the top of one micropillar, (c) Tilted 60° deposited graphene/GOx film.

6.3.2 Characterization of graphene/enzyme encrusted 3D carbon micropillar arrays

EPD method has been applied to fabricate composite bioanodes and biocathodes in this study. Graphene and enzyme were first dispersed in water and then the resultant solution was sonicated. The graphene/enzyme composite migrated toward the positive electrode when a voltage of 10 V was applied for 3 min. During the EPD process, evolution of gas bubbles at the cathode was observed because of the water electrolysis, and the deposition occurred at the anode. The microstructures of EPD co-deposited graphene/GOx onto 3D carbon micropillar arrays were investigated by SEM. From Fig. 3(a), the height of each micropillar was around 200 µm and diameter was about 50 µm. The distance between adjacent micropillar was around 150 µm. One of the main advantages of using the EPD technique is the ability for seamless integration of graphene/enzyme composite film with

high homogeneity and proper surface roughness onto both conductive 2D current collector and high respect ratio 3D micropillar. Fig. 3(b) presents the morphology of deposited graphene/GOx film on the top of the micropillar. The image suggests that small stacks of graphene layers with size around 0.5-1 μm were formed. As expected, the graphene maintained its fidelity even after EPD process and shape of stack indicated its ordered and soft texture. Furthermore, pores with dimension around several hundred nm between the stacks of graphehe layers were observed. It is indicated that the 3D graphene/enzyme network has been achieved by EPD process. These pores within the grapehene layers can improve the mass transport and the direct electron transfer from enzyme. Fig. 3(c) shows titled 60° view of the deposited graphene/GOx film. The thickness of the film was found to be around 4.6 μm. Uniformly stacked graphene sheets can be observed locally with porous structures, which can act as diffusion channels and facilitate easy penetration of mass transport species. From the SEM images, uniform stacks of graphene layers with porous multi-channel features have been formed by EPD process. Throughout the thickness of deposited film, there was almost no sign of heavily stacked graphene sheets. This developed 3D graphene/enzyme network is expected to exhibit excellent electrochemical performance for EBFC application.

The constructed 3D graphene based EBFC is shown in Fig. 1(b). Bioanodes and biocathodes were fabricated based on top-down C-MEMS and bottom-up EPD as described. GOx entrapped on graphene based anodes oxidizes the glucose to gluconolactone and generates electrons, which are transferred from anode to cathode. Then the laccase entrapped on graphene based cathode accepts the transferred electrons and reacts with oxygen to form water. In order to investigate the entrapment of GOx and laccase on anode and cathode the FTIR spectra have been studied in Fig. 4. Fig. 4 curve

(a) presents the pristine graphene on the substrate, in which there was no characteristic peak. After EPD deposition of graphene/laccase on cathode, numerous adsorption perks were observed as shown in Fig. 4 curve (b). The adsorption peak centering at 3310 cm^{-1} is assigned as N-H stretching vibration, which is the characteristic peak for amino group from enzymes [58]. The peak at 2340 cm^{-1} is consistent with C-N stretching vibration [59]. The presence of N-H bending vibration was signalled by the peak at 1620 cm^{-1} [59]. The phenolic C-O peak at 1250 cm^{-1} was from carbonyl groups and peak at 1054 cm^{-1} is consistent with C-O stretching vibration [60]. The spectrum also shows the presence of epoxy C-O stretching at a peak of 970 cm^{-1} [61]. Similarly, the FTIR spectrum for EPD deposited graphene/GOx anode is also shown in Fig. 4 curve (c). The peaks indicated N-H stretching vibration (3310 cm^{-1}) and C-N stretching vibration (2340 cm^{-1}) as well as all the C-O stretching vibration peaks were also observed. Besides, the 1730 cm^{-1} which is assigned to C=O stretching vibrations was for carboxylic group and C=C stretching vibration (1404 cm^{-1}) was also observed [62]. As we know, the amino groups (-NH) and carboxylic groups (-COOH) are abundantly available in enzymes. Although the FTIR results cannot quantify the amount of enzyme, they clearly indicate the successful co-deposition of the GOx and laccase with graphene on the 3D carbon micropillar arrays.

6.3.3 Comparison of electrochemical performance and cell performance between bare and graphene based 3D carbon micropillar arrays

To compare the electron transfer properties of the bioanodes and to verify the successful immobilization, the cyclic voltammograms were performed. Fig. 5a (i) and (ii) show the cyclic voltammograms obtained from bare 3D carbon micropillar arrays covalently immobilized with GOx and graphene/enzyme encrusted 3D carbon micropillar arrays,

respectively. The bare bioanode exhibited a redox peak at maximum current of about 0.3 mA while graphene bioanode showed a redox peak at maximum current of around 1.0 mA. Upon comparison, the graphene bioanode presented a greater redox current which can be attributed to the massively increased surface area from graphene compared to bare carbon surface. Moreover, the multi-layer microstructure with channels of deposited graphene film can significantly increase the enzyme loading and facilitate the faster and more efficient electron transfer at the same time. From the above comparison, it is evident that graphene based 3D carbon micropillar arrays make a promising platform for the EBFC in this work.

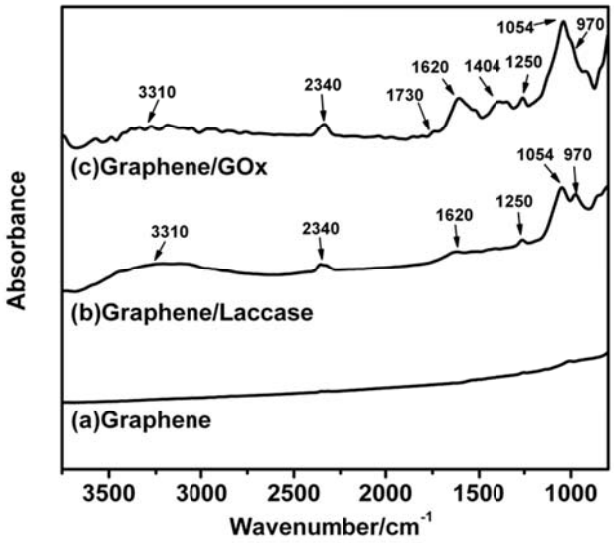

Figure 6.4. FTIR spectra of (a) graphene encrusted 3D micropillar arrays, (b) graphene/laccase encrusted 3D micropillar arrays, (c) graphene/GOx encrusted 3D micropillar arrays.

The EBFC devices were constructed using those two types of bioelectrodes. Evaluations were conducted by varying the external resistors between bioanode and biocathode. The current voltage behaviour at various external resistors of bare 3D carbon micropillar arrays for EBFC has been shown in Fig. 5(b). The open circuit voltage and

the maximum current density of were found to be 0.55 V and 164 μAcm^{-2}. Similarly, the graphene based 3D carbon micropillar arrays were assembled and tested under the same condition, resulting in an open circuit voltage of 0.91 V and a maximum current density of 653 μAcm^{-2}. In addition to the well-known excellent conductivity of graphene, the significant increase in open circuit potential and maximum current density can be attributed to the high enzyme loading on the same footprint of surface. The 3D graphene/enzyme network instead of 2D enzyme layer on the bare carbon surface exhibited much better performance.

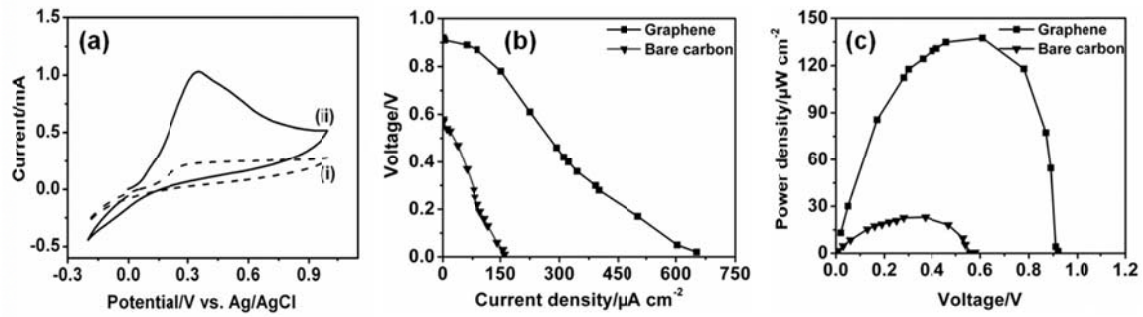

Figure 6.5. (a) Cyclic voltammogram of (i) bare carbon based (ii) graphene based bioanode in 100 mM glucose PBS solution, (b) current voltage behaviours of bare carbon based and graphene based EBFCs, (c) power density performance of bare carbon based and graphene based EBFCs.

Furthermore, the power densities of these two EBFC systems were calculated and shown in Fig. 5(c). The maximum power density of graphene based EBFC was calculated to be 136.3 μWcm^{-2} at 0.59 V, which is almost 7 times of maximum power density of bare carbon based EBFC (21.6 μAcm^{-2} at 0.38 V). In order to evaluate the stability of the two EBFC systems, the same measurements were conducted after 7 days. The power output of bared carbon based EBFC dropped 23% while graphene based EBFC decreased 49%. For the bare carbon based EBFC, the immobilization between enzyme and electrode is through chemical covalent binding which can better stabilize the enzyme on

the electrode surface than physical immobilization methods. In the case of graphene based EBFC, the enzyme and graphene were simple mixture deposited by EPD. Thus there are no stable chemical bonds between enzyme and graphene but only physical absorption immobilization. There are several reasons that could cause more decrease in power output for graphene based EBFC: 1) enzyme leaking into electrolyte; 2) enzyme denaturation in the graphene matrix; 3) enzyme agglomeration in the graphene matrix compared to uniform distribution of single layer of enzyme on bare carbon surface. Therefore, even though the performance of bare carbon based EBFC was much lower than graphene based EBFC, the chemical covalent immobilization of enzymes enabled EBFC to achieve better stability in cell performance over a period of time. Future work on developing and evaluating next generation EBFCs based on on-chip interdigital graphene encrusted C-MEMS arrays will be reported.

6.4 Conclusions

In this paper, fabrication of graphene-enzyme encrusted 3D carbon micropillar arrays for mediatorless micro-biofuel cells involving both top-down C-MEMS technology and bottom-up EPD has been demonstrated. The novelty of this design is to build graphene-enzyme matrix on the 3D microstructures. The deposited graphene exhibited uniform morphology and excellent electrochemical properties. Moreover, successful evaluation of the probability of employing the developed graphene based micropillar arrays as a potential candidate for developing EBFC has been conducted. The graphene based EBFC generated a maximum power density of 136.3 μWcm^{-2} at 0.59 V, which is almost 7 times of the maximum power density from bare carbon based EBFC.

6.5 References

13. A. Heller, *Chem. Chem. Phys.,* 2004, 6, 209

14. N. Mano, A. Heller, *J. Electrochem. Soc.,* 2013, 150, A1136

15. G. Palmore, G.M. Whitesides, G. Palmore, G.M. Whitesides, Microbial and enzymatic biofuel cells. In *Enzymatic Conversion of Biomass for Fuels Production*; Himmel, E., Ed.; American Chemical Society: Washington, DC, USA, 1994, 566, 271

16. M. Southcott, K. MacVittie, J. Halámek, L. Halámková, W.D. Jemison, R. Lobel, E. Katz, *Phys. Chem. Chem. Phys*. 2013, 15, 6278

17. E. Katz, A.N. Shipway, I. Willner, *Handbook of Fuel Cells—Fundamentals*, *Technology and Applications*; John Wiley & Sons, Ltd.: Hoboken, NJ, USA, 2003, 55

18. A.T. Yahiro, S.M. Lee, D.O. Kimble, *Biochimica. Biophysica. Acta.,* 1964, 88, 375

19. S.C. Barton, J. Gallaway, P. Atanassov, *Chem. Rev.,* 2004, 104, 4867

20. J. Kim, H. Jia, P. Wang, *Biotechnol. Adv.,* 2006, 24, 296

21. A. de Poulpiquet, A. Ciaccafava, E. Lojou, *Electrochim. Acta,* 2014, 126, 104

22. T. Miyake, S. Yoshino, T. Yamada, K. Hata, M. Nishizawa, *J. Am. Chem. Soc.,* 2011, 133, 5129

23. S. Krishnan, F.A. Armstrong, *Chem. Sci*. 2012, 3, 1015

24. F. Tasca, W. Harreither, R. Ludwig, J.J. Gooding, L. Gorton, *Anal. Chem.,* 2011, 83, 3042

25. Y.M. Yan, L. Su, L.Q. Mao, *J. Nanosci. Nanotechnol.,* 2007, 7, 1625

26. A. Lesniewski, M. Paszewski, M. Opallo, *Electrochem. Commun.,* 2010, 12, 435

27. B. Liang, L. Fang, G. Yang, Y.C. Hu, X. Guo, X. Ye, *Biosens. Bioelectron.,* 2013, 43, 131

28. C.X. Guo, F.P. Hu, X.W. Lou, C.M. Li, *J. Power Sour.,* 2010, 195, 4090

29. A.K. Geim, *Science,* 2009, 324, 1530

30. S. Sun, G. Zhang, N. Gauquelin, N. Chen, J. Zhou, S. Yang, W. Chen, X. Meng, D. Geng, M. Banis, R. Li, S. Ye, S. Knights, G. Botton, T. Sham, X. Sun, *Sci. Rep.*, 2013, 3, 1775

31. N. Cheng, J. Liu, M. Banis, D. Geng, R. Li, S. Ye, S. Knights, X. Sun, *Int. J Hydrogen Energy,* 2014, 39, 15967

32. D. Geng, Y. Chen, Y. Chen, Y. Li, R. Li, X. Sun, S. Ye, S. Knights, *Energy Environ. Sci.* 2011, 4, 760

33. B. Liang, X. Guo, L. Fang, Y. Hu, G. Yang, Q. Zhu, J. Wei, X. Ye, *Electrochem. Commun.,* 2015, 50, 1

34. J. Filip, J. Tkac, *Electrochim. Acta,* 2014, 136, 340

35. C. Liu, S. Alwarappan, Z. Chen, X. Kong, C.Z. Li, *Biosens. Bioelectron.,* 2010, 25, 1829

36. W. Zheng, H.Y. Zhao, J.X. Zhang, H.M. Zhou, X.X. Xu, Y.F. Zheng, Y.B. Wang, Y. Cheng, B.Z. Jang, *Electrochem. Commun.,* 2010, 12, 869

37. C. Liu, Z. Chen, C.Z. Li, *IEEE Trans. Nanotechnol.,* 2011, 10, 59

38. S. Palanisamy, S. Cheemalapati, S.M. Chen, *Int. J. Electrochem. Sci.,* 2012, 7, 11477

39. B. Devadas, V. Mani, S.M. Chen, Int. *J. Electrochem. Sci.,* 2012, 7, 8064

40. H.U. Lee, H.Y. Yoo, T. Lkhagvasuren, Y. Seok Song, C. Park, J. Kim, S. WookKim, *Biosens. Bioelectron.,* 2013, 42, 342

41. J.W. Long, B. Dunn, D. Rolison, H.S. White, *Chem. Rev.* 2004, 104, 4463

42. B. Dunn, J.W. Long, D. Rolison, *Interface,* 2008, 17, 49

43. C. Wang, L. Taherabadi, G. Jia, M. Madou, *Electrochem. Solid State Lett.,* 2004, 7, A435

44. C. Wang, G. Jia, L. Taherabadi, M. Madou, *Microelectromechanical Syst.,* 2005, 14, 348

45. C. Wang, M. Madou, *Biosens. Bioelectron.,* 2005, 20, 2181

46. B.Y. Park, L. Taherabadi, C. Wang, J. Zoval, M. Madou, *J. Electrochem. Soc.* 2005, 152, J136

47. K. Malladi, C. Wang, M. Madou, *Carbon,* 2006, 44, 2602

48. B. Park, Y.R. Zaouk, C. Wang, M. Madou, *ECS Trans.,* 2006, 1, 1

49. B.Y. Park, R. Zaouk, C. Wang, J. Zoval, M. Madou, *ECS Trans.* 2007, 4, 83

50. C. Wang, R.B. Zaouk, Y. Park, M. Madou, *Int. J. Manuf. Tech. Manag.* 2008, 13, 360

51. Y. Parikh, J. H. Yang, C. Wang, *J. Power Sour.,* 2009, 195, 4685

52. Y. Song, V. Penmatsa, C. Wang, *Energies,* 2014, 7, 4694

53. H. Min, B. Y. Park, L. Taherabadi, C. Wang, Y. Yeh, R. Zaouk, M. Madou, B. Dunn, *J. Power Sour.* 2008, 178, 795

54. J. H. Yang, V. Penmatsa, S. Tajima, H. Kawarada, C. Wang, *Mater. Lett.,* 2009, 63, 2680

55. W. Chen, M. Beidaghi, V. Penmatsa, W. Li, C. Wang, *IEEE Nanotech,* 2010, 9, 1222

56. V. Penmatsa, J. H. Yang, Y. Yu, C. Wang, *Carbon* 2010, 48, 4109

57. V. Penmatsa, H. Kawarada, C. Wang, *J. Micromech. Microeng.* 2012, 22, 045

58. V. Penmatsa, T. Kim, M. Beidaghi, H. Kawarada, Z. Wang, L. Gu, C. Wang, *Nanoscale* 2012, 4, 3673

59. V. Penmatsa, R. Ruslinda, M. Beidaghi, H. Kawarada, C. Wang, *Biosens. Bioelectron*. 2013, 39, 118

60. V. Penmatsa, R. Ruslinda, M. Beidaghi, H. Kawarada, C. Wang, *ECS Trans.* 2013, 45, 7

61. V. Penmatsa, H. Kawarada, Y. Song, C. Wang, *Material Science Research India,* 2014, 11, 01

62. S. Pei, J. Du, Y. Zeng, C. Liu, H, Cheng, *Nanotechnol.,* 2009, 20, 235

63. S. Hong, S. Jung, S. Kang, Y. Kim, X. Chen, S. Stankovich, S. R. Ruoff, S. Baik, *J. Nanosci. Nanotechnol.,* 2008, 8, 424

64. M. Ammam, J. Fransaer, *Biosens. Bioelectron.*, 2009, 25, 191

65. S. J. An, Y. Zhu, S. H. Lee, M. D. Stoller, T. Emilson, S. Park, A. Velamakanni, J. An, R.S. Ruoff, *J. Phys. Chem. Lett.*, 2010, 1, 1259

66. A.L. Gui, G. Liu, M. Chockalingam, G.L. Saux, E. Luais, J. B. Harper, J. J. Gooding, *Electroanal*, 2010, 22, 1824

67. C. Lee, S. E. Baker, M. S. Marcus, W. Yang, M. A. Eriksson, R. J. Hamers, *Nano lett.*, 2004, 4, 1713

68. K. H. Vase, A. H. Holm, K. Norrman, S. U. Pedersen, K. Daasbjerg, *Langmuir*, 2007, 23, 3786

69. P. Actis, G. Caulliez, G. Shul, M. Opallo, M. Mermoux, B. Marcus, R. Boukherroub, S. Szunerits, *Langmuir*, 2008, 24, 6327

70. C. Zangmeister, *Chem. Mater*., 2010, 22, 5625

71. H. Huang, C. Huang, C. Hsieh, P. Kuo, J. Ting, H. Teng, *J. Phys. Chem. C*, 2011, 115, 20689

72. W. Gao, L. Alemany, L. Ci, P. Ajayan, Nat. Chem. 2009, 1, 403.

73. A. Cass, G. Davis, G. Francis, H. Hill, W. Aston, J. Higgins, E. Plotkin, L. Scott, A. Turner, *Anal. Chem.,* 1984, 56, 671

74. Y. Okawa, M. Nagano, S. Hirota, H. Kobayashi, T. Ohno, M. Watanabe, *Biosens. Bioelectron.,* 1999, 14, 229

CHAPTER 7

HIGH-POWER MICRO BIOFUEL CELLS BASED ON THREE-DIMENSIONAL CARBON MICROPILLAR ARRAYS OF REDUCED GRAPHENE OXIDE/CARBON NANOTUBE COMPOSITE

7.1 Introduction

Since the first successful implantation of the cardiac pacemaker in 1960, the market for implantable medical devices (IMDs) has been continuously expanding for surgical treatments ranging from hearing loss to neurological disorders [1-3]. In US the demand for IMDs is expected to increase 7.7 percent annually to $52 billion in 2015 and reach $73.9 billion by 2018, which urges the development of advanced miniaturized IMDs with micropower source systems [4]. The rigorous search for alternative power sources, imposed by economic and ecological concerns, has motivated researchers in finding green and efficient energy conversion sources. Enzymatic biofuel cells (EBFCs), are a subclass of fuel cells that employ enzymes to convert chemical energy into electricity, and have been touted as a potentially promising strategy for continuous power supply of IMDs requiring power in range of micro to milli watts [5]. EBFCs offer several advantages over conventional power sources including the use of renewable and non-toxic biocomponents, high reaction selectivity, flexibility and availability of fuel, and the ability of operation under physiological conditions (human body temperature and near neutral pH) [6]. Over the last decade, the development of EBFCs has increased tremendously in the terms of enzyme immobilization and loading, power density and cell lifetime, etc [7-8]. However, despite all the strengths and possible applications of EBFCs, in order to achieve a qualified practical device, it is essential to consider some crucial factors when furthering the development of this power source system. One of the most fundamental concerns is that although enzymes are highly selective and efficient

catalysts, these biomolecules must be effectively immobilized onto an electrode surface to ensure retention of catalytic activity. Additionally, achieving high efficiency of electron transfer from the active site of the immobilized enzyme to the electrode surface is probably the most critical challenge when developing EBFCs.

Today, impressive achievements in nanoscience and nanotechnology have provided fascinating opportunities in biotechnology development. The new trends in EBFCs design include incorporating nanomaterials as the optimal environment to immobilize enzymes [9]. Graphene, the one-atom-thick planar sheet of sp2-bonded carbon atoms exhibits phenomenal mechanical, electrical and thermal properties, which have given it a stellar status in the scientific community. [10-11]. Of specific interest is oxygen-containing graphene, also referred to as graphene oxide (GO). In essence, GO is basically graphene decorated with oxygenated functional groups on both basal planes and edges. It is these functional groups that make GO such special since they can serve as sites for chemical modification or functionalization. This remarkable nanomaterial with great defects offers an ideal platform for the accommodation of various biomolecules through covalent bonds, which can solve the key issue in the fabrication of biofunctional electrodes for electrochemical applications. Recent studies have shown that GO can be used to covalently bind biomaterials such as bovine serum albumin, DNA and enzymes and it also exhibits excellent biocompatibility, enhanced electrochemical reactivity and electron transfer efficiency of biomolecules [12-15]. Meanwhile, the large effective surface area of GO can also provide a large number of active sites where high loading of biomolecules can lead to improved electron generation [16]. Owing to these specific advantages, GO-based bioelectrodes have great potential for the development of high performance EBFCs.

In order to further increase the surface area of electrode over the same footprint, previous studies have demonstrated the development of different three dimensional (3D) micro and nanostructures onto carbon microelectromechanical systems (C-MEMS) [16-25]. The high aspect ratio and short transport distance of this 3D carbon platform exhibited excellent performance for various electrochemical applications such as lithium-ion batteries, supercapacitors, biosensors and biofuel cells [26-36]. Recently, we have successfully developed an EBFC based on graphene/enzyme encrusted 3D micropillar arrays [36]. A maximum power density of 136.3 μWcm-2 was obtained at 0.59 V, which is the highest performance among the reported works on graphene based EBFC since 2010 [Table S1]. However, the physical absorption immobilization in the system led to the stability issue of the developed EBFC. Therefore, in order to increase the longevity of the cell system, substitution of graphene for GO in the fabrication of bioelectrodes to take the advantage of functionality of GO and covalent bonding with enzymes is highly necessary. Furthermore, the performance of GO-based EBFC may be hindered by the fact that these nanosheets tend to aggregate and restack and the actual accessible electrode surface area is much smaller than the theoretical value. From our previous study on GO-based ultra-high power micro-supercapacitors [30], the effective strategy to overcome the aggregation behavior is the addition of one-dimensional (1D) nanomaterials carbon nanotubes (CNTs) as spacers between nanosheets. CNTs not only prevent restacking of graphene sheets by acting as nanospacers but also add to conductivity of the GO.

Herein we present an enzymatic micro-biofuel cell based on CNT (1D)/GO (2D) hybrid nanomaterials in the form of 3D carbon micropillar arrays. The fabrication methods of this study associate top-down C-MEMS technology to build to 3D micropillar arrays platform with bottom-up electrophoretic deposition (EPD) to co-deposit

enzyme/nanomaterials composites onto the 3D micropillar arrays. EPD is a versatile method that has been successfully applied for the co-deposition of graphene with enzyme onto 3D micropillar arrays in our previous research [36]. In this study, GO and CNTs composite in the weight ratio of 9:1 has been firstly dispersed in deionized water with enzymes for covalent bonding, then followed by EPD. It was confirmed that EPD could be utilized for simultaneous deposition and reduction of GO to reduced graphene oxide (rGO). In order to demonstrate the effects of the addition of CNTs between GO nanosheets, we have fabricated sole GO-based 3D micropillar arrays for comparison. Upon comparison, the rGO/CNTs based EBFC generated almost twice the maximum power density as rGO based EBFCs. In addition, on the basis of our prototype design of an EBFC chip [37], the simulation modeling utilizing COMSOL Multiphysics based on this study has been proposed. Two modules have been applied to obtain the maximum theoretical cell performance: 1) diffusion module to incorporate the mass transport and enzymatic kinetics; 2) conductive module to integrate concentration and potential. The parameters and constants have been either extracted from the experiment data or considered under the same circumstances. By comparing both experimental and theoretical results, the efficiency of experimental rGO/CNTs based EBFC reached 71.1% for theoretical cell performance.

7.2 Methods

Chemicals. Two negative photoresists: NANOTM SU-8 25 and SU-8 100 and SU-8 developer were purchased from Microchem. GOx from Aspergillus niger (100 U mg-1 solid), laccase form Trametes versicolor (20 U mg-1 solid) and glucose were purchased from Sigma-Aldrich and used without further purification. Glucose was prepared in phosphate buffer solution (pH=7.4). Single layer GO (0.7-1.2 nm thickness and 300-800

nm dimension) and multi walled CNT (30-50nm) were purchased from CheapTubes, Inc. All aqueous solutions were prepared in deionized water.

Instrumentation. The C-MEMS fabrication was performed using a Headway researchTM photoresist spinner, OAI 800 mask aligner and Lindberg alumina-tube furnace. The morphology of the microstructures was investigated using JOEL 6335 FE-scanning electron microscopy (SEM). FTIR (JASCO FT/IR 4100 spectrometer) was used to analyze the functionalization of carbon surface.Cyclic voltammograms were measured by a multichannel potentiostat/galvanostat (VMP3, Princeton Applied Research). The resulting bioanodes and biocathodes were connected with an external circuit for EBFC performance testing using a CHI 660C workstation. The simulations have been conducted by utilizing COMSOL Multiphysics 4.3b commercial software (license No. 1023246). Briefly, the C-MEMS based 3D micropillar arrays were prepared by a two-step photolithography process followed by a pyrolysis step. In the first step, a 2D sphere (diameter of 8 mm) pattern as the current collector was formed. The NANO^{TM} SU-8 25 photoresist was spin-coated onto a silicon oxide wafer (4" in diameter, (1 0 0)-oriented, n-type) at 500 rpm for 12 sec and 3000 rpm for 30 sec, followed by soft bake at 65 °C for 3 min and hard bake at 95 °C for 7 min on a hotplate. The photoresist film was then patterned under a UV exposure dose of 300 mJ cm^{-2}, followed by post-exposure bake at 65 °C for 1 min and 95 °C for 5 min on a hotplate. Second photolithography step was conducted using NANOTM SU-8 100 photoresist to construct cylindrical micropillar arrays on patterned circle. The photoresist was spin-coated at 500 rpm for 12 sec and 1500 rpm for 30 sec followed by soft baked at 65 °C for 10 min and hard baked at 95 °C for 45 min. The exposure was conducted under a UV exposure dose of 700 mJ cm^{-2}. Post-exposure bake was done at 65 °C for 3 min and 95 °C for 10 min. The sample was

then developed using NANO^{TM} SU-8 developer for 5-10 min and followed by isopropanol rinsing and nitrogen drying. Finally, the microstructures were pyrolyzed at 1000 °C for 1 h in a Lindberg alumina-tube furnace under a constant flow of 500 sccm forming gas (95% nitrogen, 5% hydrogen). EPD has been performed to integrate rGO/CNTs and enzyme composite onto the 3D micropillar arrays surface (Fig 1). GO/CNTs at the weight ratio of 9:1 (1.5 mg/mL) and GOx (1.5 mg/mL) were dispersed in deionized water and then the dispersion was sonicated for 1 h to facilitate the covalent bonds formation. Similar preparation was used for GO/CNTs and laccase dispersion for fabrication of the biocathode. rGO/CNTs/enzyme composite was then deposited by EPD with an DC voltage of 10 V at a distance of 2 cm for 3 min. During the EPD process, evolution of gas bubbles at the cathode was observed because of the water electrolysis, and the deposition occurred at the anode. After the process, the bioelectrodes were dried and kept at 4 °C to prevent the enzyme from denaturisation. Sole GO/enzyme based bioelectrodes were prepared in the same manner for comparison.

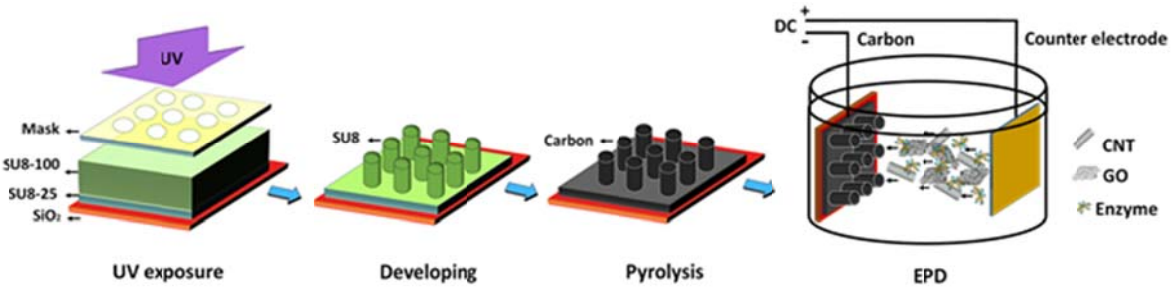

Figure 7.1. The fabrication process: top-down carbon microelectromechanical systems (C-MEMS) to fabricate the 3D micropillar arrays platform and bottom-up electrophoretic deposition (EPD) to deposit the graphene oxide (GO)/carbon nanotubes (CNTs)/enzyme onto the electrode surface (not to scale).

7.3 Results

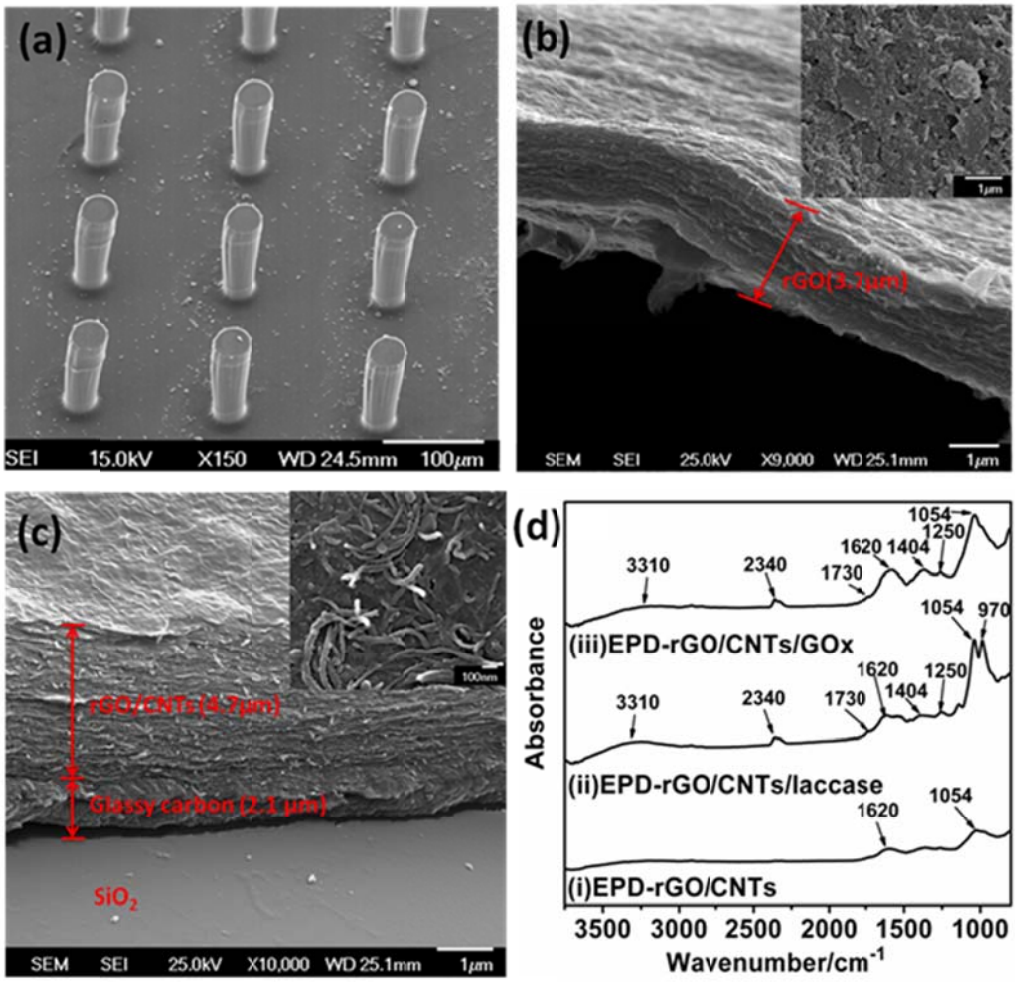

Figure 7.2. SEM images showing the morphology of (a) rGO/CNTs/GOx encrusted 3D carbon micropillar arrays; (b) Cross-sectional view and top view (inset) of deposited sole rGO/GOx on the top of one micropillar ; (c) Cross-sectional view and top view (inset) of deposited rGO/CNTs/GOx on the top of one micropillar; (d) FTIR spectra of (i) EPD-rGO/CNTs, (ii) EPD-rGO/CNTs/laccase, (iii) EPD-rGO/CNTs/GOx;

The microstructure of EPD co-deposited enzyme/nanomaterials composites onto C-MEMS based 3D micropillar arrays were investigated by scanning electron microscopy (SEM). Fig. 2(a) has shown the dimensions of the developed 3D micropillar arrays. The height of single cylindrical micropillar was about 200 μm and diameter was around 50 μm while the distance between nearby micropillar was approximately 150 μm. One of the

main reasons of using EPD process to is to seamlessly deposit nanomaterials/enzyme composite thin film simultaneously, as well as with proper surface roughness and good homogeneousness on both conductive 2D current collector and high respect ratio 3D micropillar arrays as shown from Fig 2(a). In order to obtain the thickness of nanomaterials/enzyme composite thin film, the cross-sectional views of rGO/GOx and rGO/CNTs/GOx have been investigated and shown in Fig 2(b) and Fig 2(c), respectively. Fig 2 (b), a 35° tilted view from the cross-section of rGO/GOx thin film peeled from C-MEMS 2D current collector layer, showed the local folding and non-uniform stacking of the rGO layers. The thickness of the film was found to be around 3.7 μm. Several to hundreds of stacked graphene nanosheets can be observed locally with extended irregular porous structures. In addition, in order the investigate the morphology of nanomaterials/enzyme composite thin film on the 3D microelectrode arrays, the top view of co-deposited rGO/GOx film on the top of one 3D micropillar is shown (inset in Fig. 2(b)). The small stacks of rGO nanosheets with micro-sized wrinkles that are possibly the result of GO bending during the EPD process have been observed. As expected, the rGO maintained its fidelity and the firm shape of stack indicated its soft texture. Furthermore, pores with dimension around several hundred nm between the stacks of graphehe layers were also observed. However, the heavily stacked rGO nanosheets would inhibit the diffusion of mass transport species into the rGO film and hinder the electron transfer efficiency from the enzyme to the electrode. In order to avoid the rGO restacking, the 10%wt of 1D CNTs was added to 90% wt 2D rGO and the mixture was deposited by EPD under the same condition. The 40° tilted view from the cross-section of rGO/CNTs/GOx thin film on C-MEMS 2D current collector layer is shown in Fig. 2(c). It clearly showed uniformly packed rGO nanosheets with the appearance of CNTs between

the nanosheets layers. The thickness of the think film was seen to be around 4.7 µm, which is greater than rGO/GOx thin film (3.7 µm) It is believed that the addition of CNTs, this 1D nanomaterial significantly reduced the rGO restacking and created a 3D network between 2D rGO nanosheets. This formed microstructure could act as diffusion channels, facilitate easy penetration of mass transport species and improve electron transfer efficiency between enzyme and electrodes. Therefore, the developed 3D rGO/CNTs/enzyme bioelectrodes are expected to display excellent electrochemical properties for high performance EBFCs.

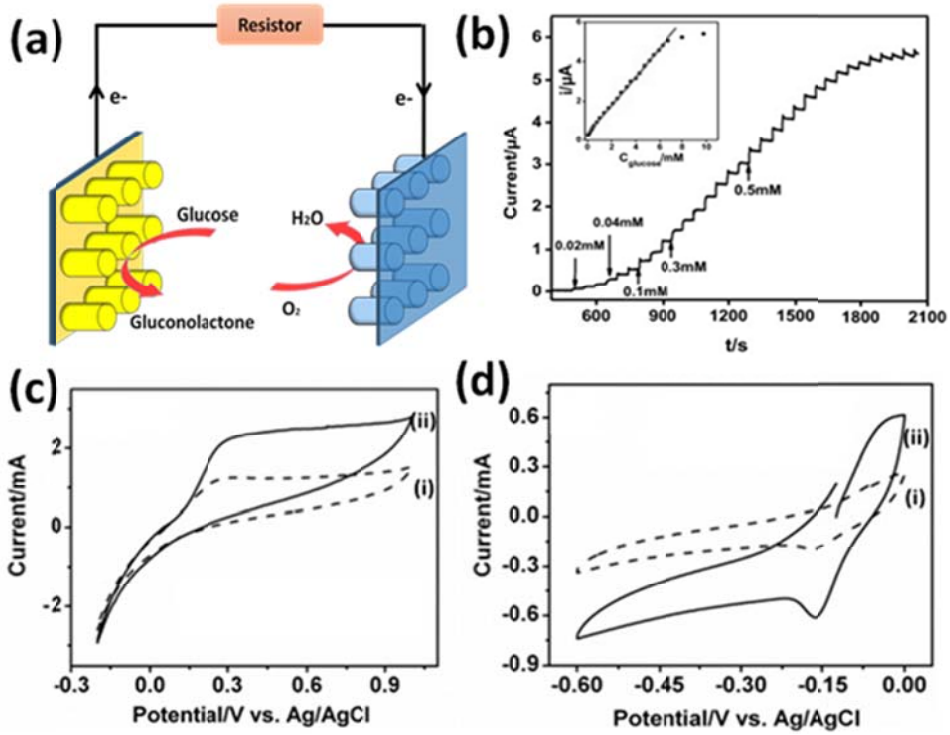

Figure 7.3. (a) Schematic of glucose EBFCs, (b) Amperometric response of rGO/CNTs/GOx bioanode at applied potential of 0.05 V to successive addition of glucose in PBS solution. (c) Cyclic voltammogram of (i) rGO based (ii) rGO/CNTs based bioanode in 100 mM glucose PBS solution, (d) Cyclic voltammogram of (i) rGO based (ii) rGO/CNTs based biocathode in oxygen saturated PBS solution.

Although the oxygenated functional groups in GO can indeed give rise to remarkable structure defects for functionalization, the loss in electrical conductivity could limit the

ability of GO as electrically active materials. Thus the reduction of GO to rGO is highly desired. The studies of the surface chemistry of deposited films with Fourier Transform Infrared Spectroscopy (FTIR) showed that the GO has been reduced to rGO during the EPD process. The FTIR spectra of GO before and after deposition are shown in Fig. S1. The broad adsorption peak centering at around 3310 cm-1 in the spectrum of GO was assigned to be isolated hydroxyl groups [38]. Water, which signals an H-O-H bending at 1635 cm^{-1}, was observed [38]. The existence of -CO_2 was confirmed by the peak at 2300 cm^{-1}. The peak at 1054 cm^{-1} was consistent with C-O stretching vibration. The presence of phenol and carboxylic acid groups were signaled by peak at 1222 cm^{-1} and 1726 cm^{-1}, respectively [38]. According to the structural model of GO, these functional groups are existed on the periphery of GO nanosheets. After the EPD process, the intensities of oxygen functionalities and water were significantly weakened. The spectrum of EPD-rGO exhibited mainly peaks originating from C-O and C=O stretching. The FTIR analysis demonstrated that the GO has been effectively reduced to rGO during the EPD process.

In order to investigate the immobilization of GOx and laccase on anode and cathode, respectively, the FTIR spectra have been studied in Fig. 2 (d). Fig. 2 (d)(i) presented rGO/CNTs on the micropillar, in which there was no obvious characteristic peak. After EPD deposition of rGO/CNTs/laccase on biocathode, various adsorption perks were observed as shown in Fig. 2 (d)(ii). The adsorption peak centering at 3310 cm^{-1} was assigned as N-H stretching vibration, which is the characteristic peak for amino group from enzymes [39]. The peak at 2340 cm^{-1} was consistent with C-N stretching vibration indicating covalent bonds between enzyme and rGO. The 1730 cm^{-1} assigned to C=O stretching vibrations was from carboxylic group and C=C stretching vibration (1404 cm-

1) was also seen [38]. The presence of N-H bending vibration has been signaled by the peak at 1620 cm^{-1}. The phenolic C-O peak at 1250 cm^{-1} was from carbonyl groups and peak at 1054 cm^{-1} was from C-O stretching vibration [38]. The spectrum also showed the presence of epoxy C-O stretching at a peak of 970 cm^{-1}. The FTIR spectrum for EPD deposited rGO/CNTs/GOx bioanode was also studied shown in Fig. 2 (d)(iii). The similar characteristic peaks were observed as well. As we know, the amino groups (-NH2) and carboxylic groups (-COOH) abundantly exist in GOx and laccase. Therefore, FTIR results clearly indicated that the successful immobilization of the enzymes with rGO/CNTs composite on the 3D carbon micropillar arrays.

In order to calculate the Michaelis-Menten constant (KM) of GOx on the developed rGO/CNTs/GOx bioanode, which is relative to enzymatic affinity and ratio of microscopic kinetic constant, the current–time relationship of the rGO/CNTs/GOx bioanode on additions of glucose at an applied potential of 0.05 V was investigated. The results showed that the bioanode could respond very rapidly to a change in the glucose concentration (Fig. 3b).The response displayed a linear glucose concentration range from 0.02 to 7.24 mM. Based on the slope, the K_M of GOx after fabrication was calculated to be 2.1 mM according to the Lineweaver-Burk equation [56]. The resulted K_M is larger than that of free enzyme (1.8 mM) which means GOx is less active after EPD on the microelectrodes. However, the result K_M is much smaller than the average published K_M of GOx after different immobilization methods [45-48]. It is suggested that enzyme after EPD based immobilization could remain comparatively active. To compare the electron transfer properties of the bioanodes and biocathodes and to verify the successful immobilization, the cyclic voltammograms were performed. Fig. 3a (i) and (ii) show the cyclic voltammograms obtained from rGO/GOx and rGO/CNTs/GOx based micropillar

arrays, respectively. The rGO/GOx bioanode exhibited a redox peak at maximum current of about 1.1 mA while rGO/CNTs/GOx bioanode showed a redox peak at maximum current of around 2.2 mA. Upon comparison, the rGO/CNTs/GOx bioanode presented a much better redox activity which can be attributed to more accessible surface area in the rGO/CNTs network compared to stacked rGO nanosheets. Moreover, the addition of CNTs can significantly increase the enzyme loading and facilitate the faster and more efficient electron transfer simultaneously. Similarly, the electrochemical performance of biocathodes has been also investigated shown in Figure 3b. Similarly, the rGO/CNTs/GOx biocathode exhibited much higher maximum redox current than rGO/GOx biocathode. From the above comparisons of both bioanodes and biocathodes, it is concluded that rGO/CNTs/GOx based 3D carbon micropillar arrays are preferred to in the construction of EBFCs to deliver high performance.

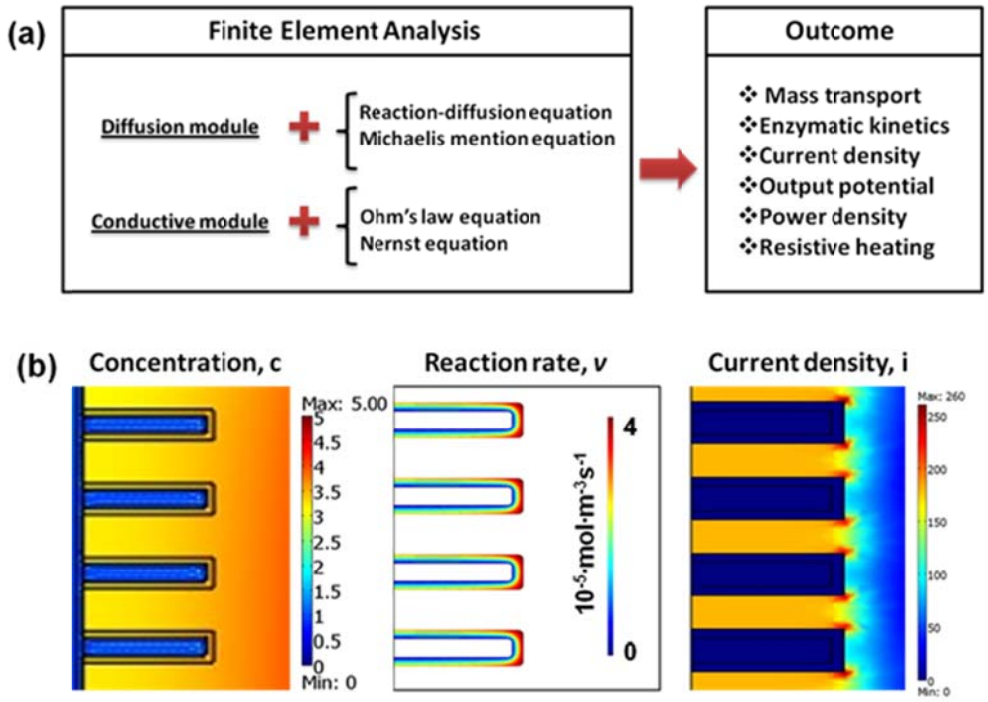

Figure 7.4. (a) Simulation flow chart; (b) Cross-sectional plot of EBFC in terms of concentration (mol/m^3), reaction rate (mol/m^{3}s), current density (mA/cm^2).

In order to predict the performance of the developed rGO/CNTs/enzyme based EBFCs, a detailed modeling of the EBFC system has been conducted by using COMSOL Multiphysics, which solves partial differential equations (PDEs) by finite element techniques (Fig 4a). Two modules have been applied: 1) diffusion module to incorporate the mass transport and enzymatic kinetics; 2) conductive module to integrate concentration and potential.

Mass transport is investigated based on glucose and oxygen diffusion around electrodes in microelectrode array. Ideally, glucose should interact with the total surface area of electrodes from top to bottom to fully utilize the enzymes immobilized onto them. However, the glucose reacts immediately with the top portion of the electrode where it diffuses first and the rest of glucose reacts gradually down to the bottom of the electrode. From the concentration profile in Fig 4b, non-uniformity of the concentration of glucose along the surface of electrode was observed. There was a decrease in the glucose concentration inside the well from the top to bottom of the electrode. The competition between higher enzyme reaction rate and lower diffusion rate causes glucose depletion throughout the electrode surface and consequently generates non-uniform glucose concentration. Since the concentration gradient on the electrode surface is influenced by the enzyme kinetics defined by the Michaelis-Menten reaction rate Equation [2], the concentration gradient from top to bottom of electrode surface leads to the relevant enzyme reaction variation in the enzyme layer shown in the reaction rate in Fig 4b. From the simulation results the enzyme reaction rate decreases from the top to bottom along the surface of microelectrodes, which is consistent with the concentration gradient results. It is also observed that the outer surfaces of the microelectrodes experience larger enzyme reaction rates in the enzyme layer due to the diffusion. In addition, the noticeable

maximum enzyme reaction rate at the top edges of the microelectrodes results from the edge effect of the electrode design. The cell performance of this EBFC was simulated and shown in Fig 4(b). The substrate will react with the enzymes immobilized on the top of the electrodes first and at the meantime diffuse and react along the electrode surface from top to bottom. The competition between higher enzyme reaction rate and lower diffusion rate causes non-uniform electron transfer throughout the electrode surface and consequently generates non-uniform current density. The current density is relatively low from the bottom of the electrode and increase in the higher portion of the electrode. It is observed that the current density maximum occurs on the top corner of each electrode. The integration of the current density along the electrode surface has been evaluated according to our previous work to calculate power density, one of the most important characteristics to examine EBFC performance. In this work, simulation was conducted by incorporating the Nernst equation as well. Various external loads at the range of 500Ω–500 kΩ are considered in the simulation in order to understand the power density-voltage relationship. As shown in Figure 5, the power density for this EBFC increases as the voltage gets higher and reaches a maximum. After reaching the maximum, increasing the voltage leads to a decrease in the power density. The maximum power density is around 272 $\mu W/cm^2$ when the voltage is approximately 0.58 V.

The EBFC devices were constructed using rGO/enzyme and rGO/CNTs/enzyme bioelectrodes, respectively as shown in Fig 5a. Evaluations were conducted by varying the external resistors between bioanode and biocathode. The current voltage behavior at various external resistors of rGO/enzyme based EBFC has been shown in Fig. 5(a). The open circuit voltage and the maximum current density of were found to be 0.81 V and 431.2 μAcm^{-2}. Similarly, the rGO/CNTs/enzyme based 3D carbon micropillar arrays

were constructed and evaluated under the same condition, resulting in an open circuit voltage of 0.88 V and a maximum current density of 844 μAcm^{-2}. The significant increase in open circuit potential and maximum current density can be attributed to the higher enzyme loading on the same footprint of surface and better conductivity of rGO/CNTs composite.

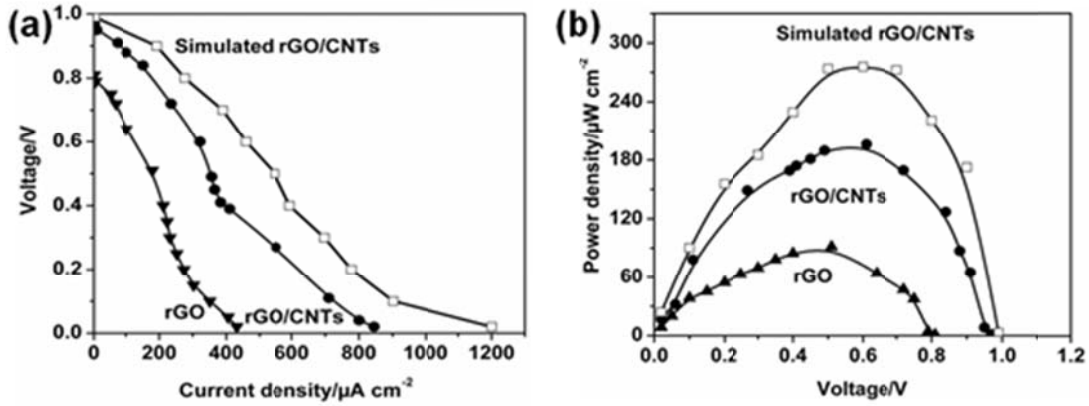

Figure 7.5. (a) Current voltage behaviors of rGO/CNTs, rGO based EBFCs and the simulated rGO/CNTs based EBFC (b) Power density performance of rGO/CNTs, rGO based EBFCs and the simulated rGO/CNTs based EBFC.

Furthermore, the power densities of these two EBFC systems were calculated and shown in Fig. 5(b). The maximum power density of rGO/CNTs/enzyme based EBFC was calculated to be 196.04 μWcm^{-2} at 0.61 V, which is about twice of maximum power density of rGO/enzyme based EBFC (91.34 μWcm^{-2} at 0.51 V). In order to evaluate the efficiency of rGO/CNTs/enzyme based EBFC, the theoretical modeling has been conducted based on the prototype of EBFCs simulations (see supplementary information). By comparing both experimental and theoretical maximum power densities, the efficiency of experimental rGO/CNTs/enzyme based EBFC reached 71.1%. The evaluation of the stability of the rGO/CNTs/enzyme based EBFC has also been considered. The same measurements were conducted after 7 days and the power output

dropped 35.5%. This performance of EBFC is adequate for operation of low-voltage CMOS integrated circuits.

7.4 Discussion

The novelty of this study is to combine the 1D and 2D carbon-based materials in the form of 3D microstructures to develop high performance micro EBFCs. In this paper, fabrication of rGO/CNTs encrusted 3D carbon micropillar arrays for micro-biofuel cells involving both top-down C-MEMS technology and bottom-up EPD has been demonstrated. The resulted new structure exhibited the following desirable characteristics: 1) conformal deposition with ordered 3D rGO/CNTs structures; 2) high surface area with active surfaces; 3) feasibility of embedding other catalysts for electrochemical reactions. The deposited rGO/CNTs thin film presented uniform morphology and the resulted bioelectrodes exhibited excellent electrochemical properties. One of the challenges in this research is to quantify the enzyme within rGO/CNTs layer because the amount of enzyme deposited by EPD is difficult to measure. Instead, the apparent Michaelis menten constant K_M was calculated as an inverse measure of the substrate's affinity for the enzyme. A smaller K_M indicates higher affinity, meaning that the enzyme reaction rate is greater. In this study, the apparent K_M of GOx after immobilization was 2.1 mM, which is not much lower than K_M of free GOx. Moreover, the evaluation of the developed rGO/CNTs based 3D micropillar arrays as a potential candidate for developing EBFC has been conducted. The rGO/CNTs based EBFC generated a maximum power density of 196.04 μWcm^{-2} at 0.61 V, which is about 2 times of the maximum power density from bare sole rGO based EBFC. Moreover, the rGO/CNTs based EBFC is believed to have highest performance among the graphene based EBFCs. In addition, the cell performance measurements were conducted within the

same rGO/CNTs based EBFC system after 7 days and the power output dropped 35.5%. Compared with our previous work on graphene based EBFC, the stability of rGO/CNTs based EBFC has been improved. The prolonged life might result from the covalent immobilization formed between the functional groups of GO and enzymes.

Furthermore, detailed and rigorously validated simulations have been used in conjunction with experimental studies in order to evaluate the efficiency of this practical EBFC system. Modeling has been incorporated to obtain the theoretical maximum performance from the same system by coupling with geometrical arrangement and reaction mechanisms. From the comparison, the rGO/CNTs based EBFC has reached 71.1% of the theoretical performance. The difference in performance between simulation and experiment has arisen several concerns. First, even though the EPD is known to form a uniform layer on different substrates, however, it was observed that some 3D microelectrodes were not fully covered. Thus, the uniform boundary condition in the nanomaterials layer could result higher cell performance in simulation results. Second, the distribution of enzyme in the rGO/CNTs layer is not predictable during EPD while the subdomain condition in simulation assumed evenly distributed. Third, the diffusion of fuel in the enzyme/rGO/CNTs layer is also not uniform in the experiment, but in the simulation, it has constant diffusion coefficient. Therefore, although the simulation is a useful tool in the pre-evaluation of actual systems, there remain different limitations in every case.

From the published performance for micro EBFCs, Mano et al. reported a high-performance EBFC generating 740 μWcm^{-2}. However, the single carbon nanofibre was used in this study and the total power could be a concern. Even though such EBFCs exhibit a high power density, they are not designed for the practical applications. The

novel microstructure in this study, instead, has integrated nano-enabled micro on-chip system, which can be suitable for powering IMDs.

7.5 Reference

1. D. L. Robertson, G.F. Joyce, Selection in vitro of an RNA enzyme that specifically cleaves single-stranded DNA. 1990, Nature, 344, 467–468.

2. C. Tuerk, L. Gold, Systematic evolution of ligands by exponential enrichment: RNA ligands to bacteriophage T4 DNA polymerase. 1990, Science, 249, 505–510.

3. S.D. Jayasena, Aptamers: An emerging class of molecules that rival antibodies in diagnostics. 1999, Clin Chem., 45,1628–1650.

4. D Shangguan, Y Li, Z Tang, Z. C. Cao, H.W. Chen, P. Mallikaratchy, K. Sefah, C. J. Yang, W.Tan, Aptamers evolved from live cells as effective molecular probes for cancer study. 2006, Proc. Natl. Acad. Sci. USA, 103, 11838–11843.

5. M. Lassila, T. J. Allen, Z. Cao, V. Thallas, K. A. Jandeleit-Dahm, R. Candido, M. E. Cooper, Imatinib Attenuates Diabetes-Associated Atherosclerosis. 2004, Arterioscler Thromb Vasc Biol, 24, 935-942.

6. A. Szabó, J. Laki, H. O. Madsen, E. Dósa, Z. Prohászka, S. Rugonfalvi-Kiss, M. Kókai, G. Acsádi, I. Karádi, L. Entz, L. Selmeci, L. Romics, G. Füst, P. Garred, Early rise in Serum VEGF and PDGF Levels Predisposes Patients With a normal MBL2 Genotype to restenosis after eversion endarterectomy. 2007, Stroke, 38, 2247-2253.

7. R. J. Barst, PDGF signaling in pulmonary arterial hypertension. 2005, J. Clin. Invest., 115, 2691–2694.

8. M. Trojanowska, Role of PDGF in fibrotic diseases and systemic sclerosis. 2008, Rheumatology, 47, v2-v4.

9. A.H. Shih, C. Dai, X. Hu, M. K. Rosenblum, J. A. Koutcher, E. C. Holland, Dosedependent effects of platelet-derived growth factor-B on glial tumorigenesis. 2004, Cancer Res., 64, 4783–4789.

10. L. Yang, C. W. Fung, E. J. Cho, A. D. Ellington, Real-time rolling circle amplification for protein detection. 2007, Anal. Chem., 79, 3320-3329.

11. A. R. Ruslinda, V. Penmatsa, Y. Ishii, S. Tajima, H. Kawarada, Highly sensitive detection of platelet-derived growth factor on a functionalized diamond surface using aptamer sandwich design. 2012, Analyst, 137,1692-1697.

12. X. Fang, Z. Cao, T. Beck, W. Tan, Molecular Aptamer for Real-Time Oncoprotein Platelet-Derived Growth Factor Monitoring by Fluorescence Anisotropy. 2001, Anal. Chem., 73, 5752-5757.

13. X. Fang, A. Sen, M. Vicens, W. Tan, Synthetic DNA Aptamers to detect protein molecular variants in a high throughput fluorescence quenching assay. 2003, ChemBioChem, 4, 829-834.

14. M. C. Vicens, A. Sen, A. Vanderlaan, T. J. Drake, W. Tan, Investigation of molecular beacon aptamer-based bioassay for platelet-derived growth factor detection. 2005, ChemBioChem, 6, 900 – 907.

15. C. J. Yang, S. Jockusch, M. Vicens, N. J. Turro, W. Tan, Light-switching excimer probes for rapid protein monitoring in complex biological fluids. 2005, Proc. Natl. Acad. Sci. USA, 102, 17278-17283.

16. Y. Jiang, X. Fang, C. Bai, Signaling aptamer/protein binding by a molecular light-switch complex. 2004, Anal. Chem., 76, 5230-5235.

17. C. Zhou, Y. Jiang, S. Hou, B. Ma, X. Fang, M. Li, Detection of oncoprotein platelet-derived growth factor using a fluorescent signaling complex of an aptamer and TOTO. 2006, Anal. Bioanal. Chem., 384, 1175–1180.

18. C. Huang, S. Chiu, Y. Huang, H. Chang, Aptamer-functionalized gold nanoparticles for turn-on light switch detection of platelet-derived growth factor. 2007, Anal. Chem., 79, 4798-4804.

19. C. Huang, C. Chiang, Z. Lin, K. Lee, H. Chang, Bioconjugated gold nanodots and nanoparticles for protein assays based on photoluminescence quenching. 2008, Anal. Chem., 80, 1497-1504.

20. C. Huang, Y. Huang, Z. Cao, W. Tan, H. Chang, Aptamer-modified gold nanoparticles for colormetric determination of platelet-derived growth factors and their receptors. 2005, Anal. Chem., 77, 5735-5741.

21. R. Y. Lai, K. W. Plaxco, A. J. Heeger, Aptamer-Based Electrochemical Detection of Picomolar Platelet-Derived Growth Factor Directly in Blood Serum. 2007, Anal. Chem., 79, 229-233.

22. T. H. Degefa, J. Kwak, Label-free aptasensor for platelet-derived growth factor (PDGF) protein. 2008, Anal. Chim. Acta, 613, 163–168.

23. A. R. Ruslinda, S. Tajima, Y. Ishii, Y. Ishiyama, R. Edgington, H. Kawarada, Aptamer-based biosensor for sensitive PDGF detection using diamond transistor.

2010, Biosens. and Bioelec., 26, 1599–1604.

24. M. F. Phillips, M. R. Lockett, M. J. Rodesch, M. R. Shortreed, F. Cerrina, L. M. Smith, In situ oligonucleotide synthesis on carbon materials: stable substrates for microarray fabrication. 2008, Nucleic Acids Res., 36, e7.

25. Y. Ishii, S. Tajima, H. Kawarada, Aptasensor for oncoprotein platelet-derived growth factor detection on functionalized diamond surface by signal-off optical method. 2011, Appl. Phys. Exp., 4, 027001-3.

26. C. Wang, L. Taherabadi, M.Madou, A novel method for the fabrication of highaspect ratio C-MEMS structures. 2005, IEEE J. Microelectromechanical Systems, 14, 348-358.

27. S. Ranganathan, R. McCreery, S.M. Majji, M. Madou, Photoresist-Derived Carbon for Microelectromechanical Systems and Electrochemical Applications. 2000, J. Electrochem. Soc, 147, 277-282.

28. A. Singh, J. Jayaram, M. Madou, S. Akbara. Pyrolysis of negative photoresists to fabricate carbon structures for microelectromechanical systems and electrochemical applications. 2002, Journal of the Electrochemical Society, 149, E78– E83.

29. J.H. Yang, V. Penmatsa, S. Tajima, H. Kawarada, C. Wang, Direct amination on 3-dimensional pyrolyzed carbon micropattern surface for DNA detection. 2009, Materials Letters, 63, 2680-2683.

30. H. Xu, K. Malladi, C. Wang, L. Kulinsky, M. Song, M. Madou, Carbon postmicroarrays for glucose sensors. 2008, 23, 163-1644.

31. J. A. Lee, S. Hwang, J. Kwak, S. I. Park, S. S. Lee, K-C Lee, An electrochemical impedance biosensor with aptamer-modified pyrolyzed carbon electrode for labelfree protein detection. 2008, Sensors and Actuators B, 129, 372-379.

32. C. Wang, L. Taherabadi, G. Jia, M. Madou, Y. Yeh, B. Dunn, C-MEMS for the manufacture of 3D microbatteries. 2004, Electrochemical and Solid-State Letters, 7, A435- A438.

33. W. Chen, M. Beidaghi, V. Penmatsa, K. Bechtold, L. Kumari, W.Z. Li, C. Wang, Integration of Carbon Nanotubes to C-MEMS for On-chip Supercapacitors. 2010, Nanotechnology, IEEE Transactions on, 9, 734-739.

34. V. Penmatsa, J. H. Yang, Y. Yu, C. Wang, Fabrication of porous carbon micropillars using a block copolymer as porogen. 2010, Carbon, 48, 4109-4115.

35. V. Penmatsa, T. Kim, M. Beidaghi, H. Kawarada, Z. Wang, L. Gu, C. Wang, Three-dimensional graphene nanosheet encrusted carbon micropillar arrays for electrochemical sensing. 2012, Nanoscale, DOI:10.1039/C2NR30161J.

36. V. Penmatsa, H. Kawarada, C. Wang, Fabrication of carbon nanostructures using photo-nanoimprint lithography and pyrolysis. 2012, J. Micromech. Microeng, 22, 045024-045032.

37. F. Tuinstra, J.L. Koenig, Raman Spectrum of Graphite. 1970, J. Chem. Phys., 53, 1126-1130.

38. H. Kawarada, A. R. Ruslinda, Diamond electrolyte solution gate FETs for DNA and protein sensors using DNA/RNA aptamers. 2011, Phys. Status Solidi A, 208, 2005-2016.

39. H. J. In, S. Kumar, Y. Shao-Horn, G. Barbastathis, Origami fabrication of nanostructured, three-dimensional devices: Electrochemical capacitors with carbon electrodes, 2006, Appl. Phys. Lett. 2006, 88, 083104 (pp.).

40. Z. Weng, Y. Su, F. Li, J. Du, Graphene–Cellulose Paper Flexible

Supercapacitors. 2011, Adv. Energy Mater. 2011, 1, 917-922.

41. G. Wang, L. Zhang, J. Zhang, A review of electrode materials for electrochemical supercapacitors. 2012, Chem. Soc. Rev., 41, 797-828.

42. P. L. Taberna, P. Simon, J. F. Fauvarque, Electrochemical Characteristics and

Impedance Spectroscopy Studies of Carbon-Carbon Supercapacitors, 2003, J. Electrochem. Soc., 150, A292-A300.

43. V. Presser, L. Zhang, J. J. Niu, J. McDonough, C. Perez, H. Fong, Y. Gogotsi, Flexible Nano-felts of Carbide-Derived Carbon with Ultra-high Power Handling Capability. 2011, Adv. Energy Mater., 1, 423-430.

44. J. A. Paradiso, T. Starner, Energy Scavenging for Mobile and Wireless Electronics. 2005, IEEE Pervasive Comput., 4, 18-27.

CHAPTER 8

SUMMARY AND FUTURE WORK

8.1 Summary

Modeling could play a vital role in optimizing the design of increasingly sophisticated devices, taking into account various factors regarding mass transport, electron transfer, and reaction kinetics. The prototype design of an EBFC chip, having 3D intedigitated microelectrode arrays was proposed to obtain an optimum design of 3D microelectrode arrays for C-MEMS based EBFCs. I have developed a detailed modeling on the effect of 1) dimensions of microelectrodes, 2) spatial arrangement of 3D microelectrode arrays, 3) geometry of microelectrode on the EBFC performance based on COMSOL Multiphysics, which solves partial differential equations (PDEs) by finite element techniques. Two modules have been applied: 1) diffusion module to incorporate the mass transport and enzymatic kinetics; 2) conductive module to integrate concentration and potential. To optimize the performance of the EBFCs, numerical simulations have been performed for cylindrical electrodes with various electrode heights and well widths in terms of mass transport of glucose, enzymatic reaction rate, current density and open circuit output potential. In addition, to find out potential long lasting electrode design, four different geometries (rectangular, triangular, tapered, semi-elliptical) were implemented in order to obtain a more uniform current density along the electrode.

Until now, majority of the EBFCs research have been focused on in vitro experiments by mimicking physiological conditions. However, additional complications may arise when an EBFC chip is placed inside a blood artery, such as implantation process, the stability of chip inside an artery and the clotting of the blood, etc. Ideally, the EBFC chip should be placed in a manner that it would not obstruct the blood flow and it should not

result in substantial pressure drop inside an artery. In order to investigate the performance of an EBFC, behavior of an EBFC chip performance inside an artery has been studied. I applied COMSOL Multiphysics software to analyze mass transport for different orientations of an EBFC chip inside a blood artery. Two orientations: horizontal position (HP) and vertical position (VP) have been analyzed. The objective of this research is to further investigate diffusion phenomenon of glucose, output potential, current density and power density of the EBFC chip in the blood artery. To improve the performance of the EBFCs in the horizontal position, the EBFC chip with holes is preferred. In the case of vertical position, optimized cell performance was obtained when four cathodes surround each anode.

Furthermore, two-dimensional graphene is a promising material candidate for high performance enzymatic biofuel cell (EBFC). The work has integrated graphene/enzyme onto three-dimensional (3D) micropillar arrays in order to obtain efficient enzyme immobilization, enhanced enzyme loading and facilitate direct electron transfer. The fabrication process of this system combines top-down carbon microelectromechanical systems (C-MEMS) technique to fabricate the 3D micropillar arrays platform and bottom-up electrophoretic deposition (EPD) to deposit the graphene/enzyme onto the electrode surface. The amperometric response of the graphene-based bioelectrode exhibited excellent electrochemical activity, which indicated the successful co-deposition of graphene with the enzymes. The developed 3D graphene/enzyme network based EBFC generated a maximum power density of 136.3 μWcm^{-2} at 0.59 V, which is almost 7 times of the maximum power density of the bare 3D carbon micropillar arrays based EBFC.

Finally, miniaturized self-contained enzymatic biofuel cells with high cell performance possess the ability to enable a new generation of minimally invasive implantable medical

devices in vivo studies. A novel method for fabricating micro-biofuel cells based on three-dimensional carbon micropillar arrays with reduced graphene oxide and carbon nanotube composite was proposed. The fabrication process of this system combines top-down carbon microelectromechanical systems (C-MEMS) technique to fabricate the 3D micropillar arrays platform and bottom-up electrophoretic deposition (EPD) to deposit the reduced graphene oxide (rGO)/carbon nanotubes (CNTs)/enzyme onto the electrode surface. Theoretical modeling of this EBFC system has also been conducted to obtain the cell performance efficiency of experimental work. Without the use of thermal or chemical based reduction methods, GO nanosheets have been readily reduced to rGO during the EPD process. The developed rGO/CNTs based EBFC generated twice the maximum power density of rGO based EBFC. Through a comparison of experimental and theoretical results, the cell performance efficiency is noted to be 67%.

8.2 Future Scope of the Research

A few years ago, one could say that the applicability of the enzymatic biofuel cell as an alternative energy source was questionable or a dream that would be difficult to come true. Rapid development on EBFCs has been achieved in the past decade with the arised demands for reliable power supplies for implantable medical device. It has shown particular advantages over conventional batteries because of the specific biocatalysts and the possibility of miniaturization. However, these systems still need to meet the requirements of practical commercial application. Significant improvements in terms of enzyme immobilization, power density, stability, cost of the employed materials, and issues related to the electron transfer between enzymes and electrode surfaces still need to be achieved. Over the last years, there have been many outcomes both in terms of mediated and direct electronic connection between enzymes and electrode surfaces. These efforts have increased the amount of research

describing enhanced electron shuttle through different electrode surfaces. Moreover, elegantly designed bioelectrodes have also been reported to enable direct electrical connection between several enzymes and solid supports.

To achieve higher power density output, the use of nanomaterials has emerged as an interesting strategy to obtain high power devices. Besides, in terms of protein engineering, despite the progress seen in the past years in enzymatic biofuel cells using mutant enzymes have been achieved, challenges still exist in this field. Fundamental studies on protein structure-function relationships are still necessary to achieve better electron transfer and substrate conversion at electrode surfaces. Moreover, standardizing stability and operation tests is crucial to obtaining consistent data on enzymatic activity retention over long periods. Therefore, in the future, besides investigating performance parameters researchers of enzymatic biofuel cells must also consider interface engineering; i.e., they must evaluate the prepared biomaterials in prototype devices, to better visualize them under operational conditions.

Finally, considering implantable technology, this area has witnessed many advances, including the promising results in terms of the generated current density. The in vivo use of enzymatic biofuel cells still requires further investigation, especially with regard to operational stability tests, to attend to the desirable durability.

VITA

YIN SONG

Born, Wuhan, China

2003-2007	B. S., Materials Science and Engineering Wuhan University of Technology Wuhan, China
2014	Dissertation Evidence Acquisition Fellowship
2015	Dissertation Year Fellowship
2008-2015	M. S., PH. D. Materials Science and Engineering Florida International University Miami, Florida

PUBLICATIONS AND PRESENTATIONS

R. Agrawal, C. Chen, Y. Hao, Y. Song and C. Wang, "Graphene for Supercapacitors" in the book “Graphene-Based Energy Devices”, John Wiley & Sons, Inc., 2015, ISBN 978-3-527-33806-1.

Y. Song, V. Penmatsa, C. Wang “Recent Development of Miniature Enzymatic Biofuel Cells” in the book “Biofuel's Engineering Process Technology”, InTech, 2011, ISBN 978-953-307-480-1.

Y. Song, R. Agrawal, C. Wang, “Micro enzymatic biofuel cells: from theoretical to experimental aspect”, Proceedings of SPIE, 2015.

Y. Song, R. Agrawal, C. Wang, “C-MEMS for bio-sensing applications”, Proceedings of SPIE, 2015.

R. Agrawal, Y. Hao, Y. Song, C. Chen, C. Wang, “Hybridization of lithium-ion batteries and electrochemical capacitors: fabrication and challenges”, Proceedings of SPIE, 2015.

Y. Song, C. Chen, C. Wang, "Graphene/enzyme-encrusted three-dimensional carbon micropillar arrays for mediatorless micro-biofuel cells", Nanoscale, 10.1039/C4NR06856D, 2015.

V. Penmatsa, H. Kawarada, Y. Song and C. Wang, "Comparison of Different Oxidation Techniques for Biofunctionalization of Pyrolyzed Carbon", Material Science Research India 2014, 11, 1-8.

Y. Song and C. Wang, "Surface Engineered Carbon Electrode Arrays for Bio-sensing", ECS transactions, 2014, 61, 49-54.

Y. Song, V. Penmatsa and C. Wang, "Modeling and Simulation of Enzymatic Biofuel Cells with Three-Dimensional Microelectrodes", Energies 2014, 7, 4694-4709.

Y. Song, R. Agrawal, Y. Hao, C. Chen and C. Wang, "Carbon Microelectromechanical Systems (C-MEMS) based Micro-supercapacitors", ECS transactions, 2014, 61, 55-64.

Y. Song, V. Penmatsa and C. Wang “Recent development of enzymatic biofuel cell”, Proceedings of SPIE 8035, 80350S (2011).

Y. Song, C. Wang, "Finite Element Analysis Approach for Optimization of Enzyme Activity for Enzymatic Biofuel Cell", Proceedings of the COMSOL Conference 2010 Boston.

Y. S. Parikh, Y. Song, and C. Wang, "Finite Element Analysis of an Enzymatic Biofuel Cell: The Orientations of a Chip inside a Blood Artery", Proceedings of the COMSOL Conference 2009 Boston.

Y. Song, R. Agrawal, C. Wang, “Micro enzymatic biofuel cells: from theoretical to experimental aspect”, SPIE, Apr 2015, Baltimore.

Y. Song, R. Agrawal, C. Wang, “C-MEMS for bio-sensing applications”, SPIE, Apr 2015, Baltimore.

R. Agrawal, Y. Hao, Y. Song, C. Chen, C. Wang, “Hybridization of lithium-ion batteries and electrochemical capacitors: fabrication and challenges”, SPIE, Apr 2015, Baltimore.

R. Agrawal, Y. Song, C. Wang, “Hybridization of lithium-ion batteries and electrochemical capacitors: fabrication and challenges”, SPIE, Apr 2015, Baltimore.

Y. Song, R. Agrawal, C. Wang, "Self-Charging Biocapacitor Hybrid System Based on Graphene/CNT Modified 3D C-MEMS Micropillar Arrays" MRS, Apr 2015, San Francisco.

C. Chen, Y. Hao, R. Agrawal, Y. Song, C. Wang, "A New Green Electrode Material based on Nature Clay for Li-ion Battery/Capacitor" MRS, Dec 2014, Boston.

Y. Hao, C. Chen, R. Agrawal, Y. Song, C. Wang, "Carbon Nanotubes and Conducting Polymer Dual Protection for Improving Sulfur Cathode Performance" MRS, Dec 2014, Boston.

Y. Song, C. Wang, "Surface Engineered Carbon Electrode Arrays for Bio-sensing" Nanoflorida, Sept 2014, Miami.

Y. Song, C. Wang, "Surface Engineered Carbon Electrode Arrays for Bio-sensing" ECS, May 2014, Orlando.

Y. Song, C. Wang, "An enzymatic biofuel cell based on graphene/CNT modified 3D C-MEMS micropillar arrays." MRS, April 2014, San Francisco.

Y. Hao, C. Chen, Y. Song, C. Wang, "Composite of Sulfer/nitrogen-doped Graphene Nanosheets as the Cathode of Lithium-Sulfur Batteries" MRS, April 2014, San Francisco.

Y. Song, C. Wang, "Evaluation of Performance of Enzymatic Biofuel Cells with Microelectrode Arrays inside a Blood Artery via Finite Element Approach" COMSOL Conference October 2013, Boston.

Y. Song, C. Wang, “A Microfluidic Enzymatic Biofuel Cell Based on Carbon Micropillar Electrode Arrays”, MRS 2012 April, San Francisco.

Y. Song, C. Wang, “A Miniature Glucose/Oxygen Biofuel Cell based on C-MEMS Interdigitated Electrode Arrays”, ECS 2011 Fall.